Universitat Politècnica de Catalunya
Escola Tècnica Superior d'Enginyers
de Camins, Canals i Ports

Departament de Resistència de Materials i Estructures a
l'Enginyeria

PhD Thesis

Stabilized Finite Element Approximation of the Incompressible MHD Equations

by

Noel Hernandez Silva

Advisor:
Ramon Codina Rovira

Barcelona, July 12, 2010

A mi pequeña gran familia.

Agradecimientos

Durante el esfuerzo que esta tesis representa, recibí la ayuda y el apoyo de muchas personas. En estas breves líneas quiero manifestarles mi gratitud.

En primer lugar deseo agradecer a mi tutor Ramon Codina. Prácticamente sin conocerme acepto guiarme en este camino y supo ser paciente con mis innumerables tropiezos. No solo es generoso al compartir sus conocimientos, sino que además siempre esta dispuesto a ayudar a sus estudiantes y también a quienes no lo son. En suma, Ramon es el ejemplo de lo que debe ser un Científico, Catedrático y Tutor.

También deseo agradecer a los compañeros de la universidad que a lo largo de los años compartieron las penas y las alegrías del doctorado. En primer lugar deseo mencionar al grupo de Mecánica de Fluidos de Ramon. Guillaume Houzeaux, Santiago Badia, Oriol Guasch, Matias Avila, Christian Muñoz, Javier Principe y Herbert Coppola. Gracias por acompañarme en esta parte del camino.

Ocupan un lugar importante los compañeros del despacho 105, con quienes compartí mucho más que una oficina. Maritzabel Molina, Pablo Vargas, Carlos Lara, Joaquín Hernández, Xavier Martínez, Fernando Rastellini, Roberto Serpieri, Flavia Bastos, Carlos Recarey, Joanna Irigoyen, Quino Valverde, Maria Laura De Bellis, Juan Carlos Vielma y Mailhyn Cafiero. A todos gracias por haber hecho mas interesante mi paso por el despacho 105 y sobre todo gracias por soportar mi manía de congelarlos con el aire acondicionado.

La comunidad mexicana en el departamento de Resistencia de Materiales y Estructuras en la Ingeniería fue siempre una compañía constante y un apoyo desinteresado. Gerardo Valdés, Fernando Guzmán, Guillermo Díaz, Gelacio Juárez y Humberto Esqueda. A todos gracias por su compañía y los buenos momentos que compartimos durante nuestras andanzas juntos.

El ambiente de discusión intelectual y camaradería que viví durante mi estancia en Barcelona no habría sido tan estimulante como lo fue sin varias personas a las cuales también quiero agradecer: Martha Liliana Carreño, Dorian Luis Linero, Sergio Blanco, Pablo Mata, William Taylor Matias Silva, Roberto Clemente, Carlos Ferrari, Eduardo Chaves y Esteban Samaniego. Gracias por las discusiones de café, las charlas de pasillo y los puntos de vista diferentes. La hospitalidad de Alejandra Arlettaz merece una mención especial. Le agradezco sus atenciones y el haberme soportado durante el tiempo que compartí departamento con ella y Fernando Rastellini.

Quiero también agradecer a Víctor Zurita y a Zeidy Sarabia, del equipo de liderazgo de la sección de Performance Engineering en General Electric, que amablemente me han brindado todas las facilidades para preparar la defensa y presentación final de esta tesis.

Los recursos financieros que hicieron posible mi estancia en Barcelona fueron provistos por el Consejo Nacional de Ciencia y Tecnología de México que tuvo a bien confiar en mí y otorgarme la beca que me permitió realizar mis estudios de doctorado. Agradezco a CONACYT el apoyo proporcionado.

No puedo dejar de mencionar a las personas que, desde México, nunca dejaron de apoyarme y alentarme, mi pequeña gran familia. En primer lugar mi madre Maria de la Luz que siempre me ha animado a perseguir mis sueños y confiar en mis capacidades. Todo lo que soy se lo debo a ella. Agradezco a mi hermano Oliver y su esposa Ana Lilia, quienes a pesar de estar sufriendo las mismas vicisitudes de un doctorado, siempre me apoyaron y al momento de escribir estas líneas esperan a su primer hijo.

Durante este andar, muchas personas han contribuido a enriquecerme con experiencias, enseñanzas y conocimientos. Cada persona debe buscar su camino en la vida y descubrir por si misma el fin último de la existencia humana y es por esta razón que algunas han tomado senderos que hacen difícil que nos volvamos a encontrar. Aun sin mencionar sus nombres quiero agradecerles por haberme acompañado por lo menos una parte de este camino. Lamento que no estén conmigo, pero al igual que todas las personas que he mencionado, forman parte indeleble de mi memoria.

A todos gracias.

Resumen

No es frecuente encontrar un campo donde dos ramas principales de la Física estén involucradas. La Magnetohidrodinámica es uno de tales campos debido a que involucra a la Mecánica de Fluidos y al Electromagnetismo. Aun cuando puede parecer que esas dos ramas de la Física tienen poco en común, comparten similitudes en las ecuaciones que gobiernan los fenómenos involucrados en ellas. Las ecuaciones de Navier–Stokes y las ecuaciones de Maxwell, ambas en la raíz de la Magnetohidrodinámica, tienen una condición de divergencia nula y es esta condición de divergencia nula sobre la velocidad del fluido y el campo magnético lo que origina algunos de los problemas numéricos que surgen en la modelación de los fenómenos donde el flujo de fluidos y los campos magnéticos están acoplados.

El principal objetivo de este trabajo es desarrollar un algoritmo eficiente para la resolución mediante elementos finitos de las ecuaciones de la Magnetohidrodinámica de fluidos incompresibles.

Para lograr esta meta, los conceptos básicos y las características de la Magnetohidrodinámica se presentan en una breve introducción informal.

A continuación, se da una revisión completa de las ecuaciones de gobierno de la Magnetohidrodinámica, comenzando con las ecuaciones de Navier–Stokes y las ecuaciones de Maxwell. Se discute la aproximación que da origen a las ecuaciones de la Magnetohidrodinámica y finalmente se presentan las ecuaciones de la Magnetohidrodinámica.

Una vez que las ecuaciones de gobierno de la Magnetohidrodinámica han sido definidas, se presentan los esquemas numéricos desarrollados, empezando con la linealización de las ecuaciones originales, la formulación estabilizada y finalmente el esquema numérico propuesto. En esta etapa se presenta una prueba de convergencia.

Finalmente, se presentan los ejemplos numéricos desarrollados durante este trabajo. Estos ejemplos pueden dividirse en dos grupos: ejemplos numéricos de comparación y ejemplos de interés tecnológico. Dentro del primer grupo están incluidas simulaciones del flujo de Hartmann y del flujo sobre un escalón. El segundo grupo incluye simulaciones del flujo en una tobera de inyección de colada continua y el proceso Czochralski de crecimiento de cristales.

Abstract

It is not frequent to find a field where two major branches of Physics are involved. Magnetohydrodynamics is one of such fields because it involves Fluid Mechanics and Electromagnetism. Although those two branches of Physics can seem to have little in common, they share similarities in the equations that govern the phenomena involved. The Navier–Stokes equations and the Maxwell equations, both at the root of Magnetohydrodynamics, have a divergence free condition and it is this divergence free condition over the velocity of the fluid and the magnetic field what gives origin to some of the numerical problems that appear when approximating the equations that model the phenomena where fluids flow and magnetic fields are coupled.

The main objective of this work is to develop an efficient finite element algorithm for the incompressible Magnetohydrodynamics equations.

In order to achieve this goal the basic concepts and characteristics of Magnetohydrodynamics are presented in a brief and informal introduction.

Next, a full review of the governing equations of Magnetohydrodynamics is given, staring from the Navier–Stokes equations and the Maxwell equations. The MHD approximation is discussed at this stage and the proper Magnetohydrodynamics equations for incompressible fluid are reviewed.

Once the governing equations have been defined, the numerical schemes developed are presented, starting with the linearization of the original equations, the stabilization formulations and finally the numerical scheme proposed. A convergence test is shown at this stage.

Finally, the numerical examples performed while this work was developed are presented. These examples can be divided in two groups: numerical benchmarks and numerical examples of technological interest. In the first group, the numerical simulations for the Hartmann flow and the flow over a step are included. The second group includes the simulation of the clogging in a continuous casting nozzle and Czochralski crystal growth process.

Table of Contents

List of Figures

Chapter 1

Preliminaries

1.1 Introduction

This thesis presents a stabilized finite element approximation for the incompressible Magnetohydrodynamics[1] equations. This stabilized finite element approximation is focused at incompressible fluids and the main technological applications in mind are those related with material processing techniques. The numerical simulation of MHD phenomena faces two problems: the stabilization of the numerical solution and the enforcement of the free divergence condition of the magnetic field.

Although MHD originates in the XIX^{th} century, its applications are more recent. It was not until early 1980's that the academic world realized the potential uses of MHD in the processing of liquid metals. The main advantage of MHD in the liquid metals processing is that it provides a mean of non intrusive manipulation. This non intrusive manipulation in liquid metals makes possible to stir, damp and levitate liquid metals avoiding any contamination.

With the advent of modern numerical methods the simulation of MHD phenomena started, but it faced important problems, mainly because of spurious solutions in the magnetic field. These spurious solutions made desirable the development of a completely stabilized finite element approximation of MHD equations. In this thesis the stabilization of MHD equations is performed using the algebraic version of the Variational Multiscale approach. Another problem faced in finite element approximations of MHD is the enforcement of the free divergence condition of the magnetic field. This last problem is addressed using a fictitious variable r which plays the role of a Lagrange multiplier.

The stabilized finite element approximation presented in this work makes possible to gain insight in very complex phenomena which take place in modern metallurgy when magnetic fields are used to process liquid metals. This insight will be useful to design and optimize operations where MHD phenomena takes place and therefore important industrial process can be improved.

[1] MHD will be used as abbreviation

1.2 Objectives

In a broad sense, the main goal of this work is to develop a numerical tool which makes possible to simulate the behavior of liquid metals in the presence of magnetic fields. To accomplish this goal several objectives must be formulated. These objectives are reviewed next.

1.2.1 General Objective

The objective of this thesis is the theoretical formulation, development, computational implementation and application of a numerical model for Magnetohydrodynamics equations for incompressible fluids. For the development of this numerical model the Variational Multiscale approach for stabilized finite elements will be used.

1.2.2 Specific Objectives

The specific objectives to achieve in order to succeed in the general objective are:

1. To study the state of the art of the following subjects:
   - Numerical simulation of fluid flow using stabilized finite elements.
   - Numerical simulation of MHD using finite elements.
   - Stabilization methods using Variation Multiscales.
   - Industrial applications of MHD.
2. To arrive to a theoretical formulation of a numerical model for MHD equations for incompressible fluids in the stationary case.
3. To build a computational formulation of the numerical model for MHD equations for incompressible fluids in the stationary case in *ZEPHYR*.[2]
4. To arrive to a theoretical formulation of a numerical model for MHD equations for incompressible fluids in the time–dependent case.
5. To build a computational formulation of the numerical model for MHD equations for incompressible fluids in the time–dependent case in *ZEPHYR*.
6. To develop a convergence study for stationary and time–dependent cases. To compare this study with results reported by others researchers.
7. To incorporate the thermal coupling in the numerical model.
8. To build numerical simulations of industrial cases where MHD is involved.

[2] *ZEPHYR* is a Stabilized Finite Element Method program developed by Prof. Codina´s research group at UPC

1.3 State of the Art

This section provides a review of the state of the art in four different fields related with this research. First, it is presented a brief review of the historical development of Magnetohydrodynamics because MHD is still an obscure and unknown topic not only for the layperson but also for the scientifically literate reader. It is also presented a review of the development experience by the applications of Magnetohydrodynamics. Some of the applications of Magnetohydrodynamics have been abandoned, others are well established and a third group is still under development. It is also highly convenient to know the previous attempts to apply the Finite Element Method to the simulation of phenomena related to Magnetohydrodynamics. This is the main reason why a review of Finite Element Method applied to Magnetohydrodynamics is documented. Finally, the last part of this section is devoted to review the stabilization techniques in the Finite Element Method.

1.3.1 Brief Historical Review of MHD

The Maxwell equations and the Navier–Stokes equations are scientific knowledge originated in the XIX^{th} century, nevertheless MHD did not fully develop until the XX^{th} century. The first MHD phenomena were reported by Ritchie [54]. At the same time Faraday [20] tried unsuccessfully to measure the electric potential induced between the opposite banks of the Thames river by the movement of the water in the Earth's magnetic field. Although conceptually the experiment was sound, he failed because the instruments available at that time did not have enough sensitivity. This can be seen as the first serious attempt to take into account MHD effects in real life situations.

The next important development of MHD took place when Larmor [41] proposed that the magnetic fields around the planets and stars were originated by the so called *Dynamo Effect*. This effect consists in the appearance of a magnetic field because the liquid metallic core of the planet acts like a self–induced dynamo. This theory was confirmed and developed further by Cowling [16]. Shortly after Cowling works, Hartmann [26, 27], published theoretical and experimental works on mercury flow under the influence of magnetic fields. Due to this work the flow of a liquid metal under the influence of a magnetic field was named *Hartman Flow*.

The last theoretical development in MHD was done when Alfvén [1] published the discovery of the waves that take place in plasma due to ions oscillations around their equilibrium positions. This discovery points the beginning of a new branch of Physics, fully developed, and called Magnetohydrodynamics, name that was coined and first used by the same Alfvén [2]. His work in MHD was awarded with the Nobel Prize for Physics in 1970.

1.3.2 Development of MHD Applications

As was explained in section 1.3.1, MHD has its origins in the XIX^{th} century but its applications began to appear some time after. In 1917 Kürth [38] suggested the idea of using a magnetic field to stir a liquid metal before its solidification. In 1933

Shtanko [59] made the first experiment to stir liquid metals using a stator from an electric motor where he put a small sample of liquid steel. An aspect less known about MHD applications is that Albert Einstein and Leonard Szilard [19] patented a pump for liquid metals, which employed MHD. This patent was the result of their efforts to design and build new refrigeration cycles. Those readers interested in this facet of Albert Einstein are referred to the article of Hughes [33]. In 1958, Mullin and Hulme [48] suggested by the first time the use of magnetic fields in the processing of semiconductors.

One of the most studied applications of MHD is its use in MHD generators. The objective is to build an electric generator which could transform thermal energy or kinetic energy directly into electricity, employing plasmas as work fluid. This idea is not new, the same Faraday proposed it in his Bakerian lecture to the Royal Society, [20]. The first research was done at Westinghouse Company in the late 1930´s and the first patent was issued to Karlovitz in 1940, [36]. Although the theory behind MHD generator is correct some problems have arisen. The main problems are the generation of toxic by–products, generator inefficiency[3] and economic limitations. These problems together with the increasing availability of nuclear energy made interest in MHD generators decline by the late 1960's.

In 1962 Phillips [52] proposed the use of MHD to build a magnetohydrodynamic propeller to drive ships and submarines. This idea was latter developed by the Mitsubishi company which built in 1992 a ship called Yamato I,[57]. This ship used a liquid helium-cooled superconductor to propel the water. Unfortunately the project was a complete failure because the speed achieved was only 15 Km/hr. The failure can be attributed to the fact that the magnetic field employed at Yamato I was only 4.0 Teslas.

Since the late seventies of the XX^{th} century the metallurgic industry started to use extensively magnetic fields to stir metallic alloys during their solidification. In the beginning of the eighties research related with metallurgical applications of MHD started. The term *Metallurgical Magnetohydrodynamics* was coined in the conference of the International Union of Theoretical and Applied Mechanics held in Cambridge (UK) in 1982 [47]. Since then, the research in MHD has focused on applications of MHD related with metallurgy because it is an area which has an important research potential. The reader interested in an exhaustive revision of MHD applied to metallurgy is referred to the papers written by Davidson [17] and Dold and Benz [18]. Recently MHD applications have been proposed in very unusual fields. For instance it is used in an artificial heart, [50], and it is used to detect the wakes of vessels, [63], this last application with obvious military uses.

1.3.3 Finite Element Applied to MHD

The first work were the finite element method is applied to the equations of MHD dates from the early seventies. Wu [62] applies the finite element method to MHD equations considering a completely developed,unsteady, laminar, incompressible

[3]Typical MHD generators have efficiencies around 17%, which compared to 40% in conventional Rankine cycle power plants made MHD generators unattractive.

Hartmann flow. In this work the author only treats low magnetic Reynolds numbers and therefore he considers that the applied magnetic field is not altered by the movement of the fluid. After this work Bani and Lal [60] made some research applying the finite element method to MHD equations at small Hartmann numbers, but opposed to Wu, calculating the induced magnetic field. Peterson [51] offers a theoretical study on the existence and uniqueness of the solution for a finite element scheme over the case of an unperturbed applied magnetic field. In 1989, Tezer–Sezgin and Köksal [61] applied the finite element method to MHD equations on problems with Hartmann numbers up to 100. In the theoretical analysis, Gunzburger, Meir and Peterson [24] performed a complete study of Galerkin approximation of stationary incompressible MHD equations and they offer proof of existence and uniqueness of the solution. All the previous works took the magnetic field and the velocity as unknowns. An alternative approach is tackled by Meir and Schmidt, [45, 46]. They take as unknowns the velocity and the electric current. Also Meir [44], introduces the study of thermally coupled MHD flows. Armero and Simo [3] presented numerical schemes that preserve the dissipative properties of the continuum transient system and applied these schemes to two-dimensional MHD problems.

One of the biggest concerns about the finite element method applied in situations where magnetic fields are involved is the onset of spurious solutions in the magnetic field. These spurious solutions are commonly associated to the numerical treatment of the Maxwell equations. Nonetheless, Jiang, Wu and Povinelli [34], showed that the origin of the spurious solutions is the inadequate handling of the magnetic field divergence equation (3.3.4). In the same article, the authors proposed to employ a fictitious variable r, which plays the same role than a Lagrange multiplier to enforce the equation (3.3.4). Based in this last article Ben Salah, at [56, 55], proposed a stabilized finite element scheme for the MHD equations using the fictitious variable r. Gerbeau [21] studied the convergence of a finite element scheme for the MHD equations although without including in the analysis the fictitious variable r. Guermond and Nimev, [22, 23], applied the finite element method to MHD equations in the low frequency limit in a domain composed of conducting and isolating regions. Finally Charina [10] developed a mixed variational formulation for velocity, stress, current and potential boundary conditions for stationary MHD. In this work, a finite element discretization is used. Existence and uniqueness, if solution is under the assumption of sufficient small data can be proved as in [24]. The interested reader can also consult Gunzburger classic book [25].

1.3.4 Stabilized Finite Element Method

Given the fact that a stabilized finite element scheme is the aim of this work, it is convenient to review briefly the history of the stabilization concept in the finite element method.

It is considered that Brooks and Hughes [8] presented the first stabilized finite element scheme. In this work they introduced diffusion in the streamlines to avoid numerical oscillations due to low diffusion in Convection-Diffusion problems and in the equations of Navier-Stokes. Shortly after this work, in 1984, Arnold, Brezzi and

Fortin [4] presented a stabilized finite element scheme where a triangular element used linear interpolations for velocity and pressure, but also the velocity field was enriched with bubble functions. Hughes, Franca and Balestra, [31], employed a stabilized finite element scheme to solve the Stokes problem using equal order interpolations for pressure and velocity and therefore avoiding the inf-sup condition. The inf-sup condition imposes compatibility restrictions between the interpolation fields involved in the mixed formulation, in order to assure convergence and uniqueness of the solution. Shortly after this, Hughes, Franca and Hulbert [32], developed the GLS method (*Galerkin Least Squares*). In this last method the stabilization terms are based on the residual of the governing equation. Baiocchi, Brezzi and Franca [5], showed in 1993 that the GLS method and the method based in bubble functions were equivalent. The works of Hughes [29], and Hughes, Feijoo, Mazzei and Quincy [30], presented a formulation of the *method of sub–scales*, which is a frame where other stabilization methods can be identified, formulated and justified. Codina [11], presents a comparative and detailed vision of the different stabilization methods, Codina [13] proposes a stabilization method based on the algebraic version of the Variational Multiscales approach, finally Codina [14] proposed a stabilization method based on taking the sub–scales orthogonal to the finite element space.

1.4 Structure of the Thesis

In this section the structure of this thesis is presented and briefly discussed. This work is divided in six chapters where the MHD phenomena is presented and discussed, its numerical scheme is developed and some numerical simulations, performed during the development of the research, are presented. The constituent chapters of this thesis are:

Chapter 2: An Informal Introduction to Magnetohydrodynamics
This chapter provides a brief and informal introduction to Magnetohydrodynamics. MHD is not a topic normally covered in undergraduate or graduate courses and therefore an introduction is necessary. The introduction is shallow and non exhaustive. Its main goal is to explain the physical mechanism behind the interaction between fluid velocity and magnetic fields. This chapter also explains some applications of MHD in liquid metals processing.

Chapter 3: Governing Equations of Magnetohydrodynamics
This chapter reviews the main governing equations of MHD. The Navier–Stokes equations and the Maxwell equations are covered in the frame work of Continuum Mechanics. The MHD approximation is also reviewed in order to understand the limitations of the model employed. The final MHD equations are also covered in this chapter. The Boussinesq approximation in MHD is briefly studied together with the non dimensional form of the MHD equations. Finally MHD keystone, the Hartmann flow, is presented.

Chapter 4: Numerical Schemes
The development of numerical schemes used in this work is presented in this

chapter. The variational form of MHD equations is presented together with its time discretization. Next, a simple linearization is studied in detail. The main contribution of this work, the stabilization method for the MHD problem, is also presented in this chapter. Finally the definitive numerical scheme is presented together with a convergence test.

Chapter 5: Numerical Simulations
Results from numerical simulations performed in this research are presented in this chapter. All numerical simulations were done using *ZEPHYR*. The numerical simulations presented are the Hartmann Flow, Flow Over a Step, Flow Past a Circular Cylinder, Clogging in Continuous Casting of Steel and Crystal Growth. The last two simulations are oriented toward practical applications of MHD in materials processing techniques.

Chapter 6: Conclusions
This chapter presents the conclusions and achievements of this research. Some suggestions for future research lines to be developed, as a direct consequence of this research, are also discussed.

It is worthy of mention the fact that this research effort has produced so far, three articles in journals and one in proceedings. These articles are listed next:

- R. Codina and N. Hernandez–Silva
"Stabilized finite element approximation of the stationary magnetohydrodynamics equations", Comput. Mech. Vol. 38, pp. 344–355, (2006).

- R. Codina and N. Hernández
"Approximation of the thermally coupled MHD problem using a stabilized finite element method", Submitted to Journal of Computational Physics.

- N. Hernández and R. Codina
"Finite Element Simulation of the Czochralski Process for Crystal Growth", Submitted to Finite Elements in Analysis and Design.

- N. Hernández and R. Codina
"Resolución numérica de las ecuaciones de la magnetohidrodinámica en el proceso Czochralski para la obtención de cristales semiconductores", Memorias del V Congreso Internacional de Métodos Numéricos en Ingeniería, Centro de Investigación en Matemáticas, ISBN: 978-968-5733113. Eds. S. Botello y M.A. Moreles. Guanajuato (México), Febrero 3-5, 2010.

1.5 Notation

In an area like MHD, which is a combination of two fields like Fluid Mechanics and Electromagnetism, it is important to have a clear notation in order to avoid misunderstandings or confusions. One clear example of these confusions is the use of μ which in Fluid Mechanics is used for dynamic viscosity and in Electromagnetism

is used for magnetic permeability. In order to avoid such problems the notation used in this work is presented next.

α	Thermal diffusivity
β	Thermal expansion coefficient
γ	Lorentz factor
ϵ	Electric permittivity
ϵ_0	Electric permittivity for free space
λ	Impedance
μ	Dynamic viscosity
μ_m	Magnetic permeability
μ_0	Magnetic permeability for free space
ν	Kinematic viscosity
ρ	Mass density
ρ_e	Electric charge density
ρ_r	Reference density
σ	Conductivity
$\boldsymbol{\sigma}$	Stress tensor
$\Phi(\mathbf{u})$	Rate of viscous dissipation
ψ	Heat source
$\mathbf{B}$	Magnetic flux density
B	Characteristic magnetic field for a flow
c	Speed of light in free space
c_p	Specific heat at constant pressure
$\mathbf{D}$	Rate of Deformation tensor, Electric flux density
$\mathbf{E}$	Electric field strength
$\mathbf{F}$	Body force
$\mathbf{f}$	Body force per mass unit
Gr	Grashof number
$\mathbf{H}$	Magnetic field strength
Ha	Hartmann number
$\mathbf{I}$	Identity tensor
$\mathbf{J}$	Electric current density
k_t	Heat conductivity
l	Characteristic length for a flow
p	Pressure
Pr	Prandtl number
q	Electric charge
r	Fictitious Magnetic Pressure
Re	Reynolds number
Rm	Magnetic Reynolds number
S	Coupling parameter
ϑ	Temperature
ϑ_r	Reference temperature
U	Characteristic velocity for a flow
$\mathbf{u}$	Velocity of the fluid
$\frac{D(\bullet)}{Dt}$	Material derivative
$(\mathbf{u}\cdot\nabla)(\bullet)$	Convective derivative

Chapter 2

An Informal Introduction to Magnetohydrodynamics

The objective of this chapter is to provide a brief and informal introduction to Magnetohydrodynamics. This is done in order to delineate the kind of phenomena to be studied. The first section explains what is Magnetohydrodynamics and what is the subject of study of Magnetohydrodynamics. The second section explains the physical mechanism behind the interaction between magnetic fields and conducting fluids which is the hallmark of Magnetohydrodynamics. The third and final section reviews some practical applications of Magnetohydrodynamics in Materials Processing.

2.1 What is Magnetohydrodynamics?

Magnetohydrodynamics is a branch of Physics which studies the mutual interaction between fluids in movement and magnetic fields. Although fluid flows and magnetic fields are almost ubiquitous, they only interact when the fluid in movement is an electric conductor and non magnetic. These restrictions over the kind of fluid only leave liquid metals, hot ionized gases (plasmas) and strong electrolytes as the fluids to be studied by MHD.

Although MHD can seem to be a Science Fiction topic by the general public [1] its effects are present in every day life. For instance, the ocean covers 71% of the surface of the Earth, and saline water is a strong electrolyte, therefore the Earth's magnetic field interacts with the sea water. This interaction between saline water and the Earth's magnetic field gives origin to an induced magnetic field, although it is too small to be seen without very sensitive instruments.

Another phenomenon related with MHD is the Earth's magnetic field itself. The Earth's magnetic field is generated due to the so called *Dynamo Effect* which is the process of magnetic field generation by the inductive action of a conducting fluid.

[1] Any layperson usually recalls MHD in relation with Tom Clancy's novel "The Hunt for the Red October"

It is generally believed that the convection in the outer Earth's core, combined with stirring caused by Earth's rotation gives rise to the Earth's magnetic field.

One of the most beautiful phenomenon in Nature is the Aurora Borealis which is also governed by MHD. This phenomenon is originated from the interaction between the Earth's magnetosphere and the solar wind. Both of them are ionized gases (plasma), which can conduct electricity. They are immersed in a magnetic field (Earth's magnetic field) and due to the movement of one relative to the other an electric current arises in the closed circuit that threads both plasmas. This string of natural phenomena illustrates how the MHD is not a Science Fiction topic but a useful branch of Physics.

Although MHD finds most of its applications in Astrophysics and Geophysics, there are important applications in material processing phenomena, but those applications will be reviewed in section 2.3.

2.2 Physical Mechanism of MHD

In order to gain insight of the MHD phenomena it is important to visualize the way in which MHD works. It is important to understand which kind of physical mechanism is behind the coupling between the velocity field of the flow and the magnetic field. First, it must be said that the mutual interaction between the magnetic field and the velocity field of the fluid, arises from three different physical principles which are: Faraday's Law, Ampère's Law and Lorentz's Force. Each one of these physical principles intervenes in the coupling.

It could be useful to think the coupling as a three steps process. Although this is quite artificial, it is helpful in order to understand the interaction between the magnetic field and the velocity field.

1. The relative movement between the conducting fluid and the imposed magnetic field generates, according to Faraday's Law, an Electro Motive Force (E.M.F.). This E.M.F. originates an electric current.

2. In turn, the electric current originated by the E.M.F. gives origin to a second magnetic field, according to Ampère's Law. The second magnetic field is called induced magnetic field. The induced magnetic field is added to the imposed magnetic field. The effect of the two magnetic fields is such that it seems like if the fluid were dragging the magnetic lines.

3. The resulting magnetic field (the original and the induced) interacts with the density of induced current, to give rise to a Lorentz's Force. This force acts on the conducting fluid against the relative movement between the fluid and the imposed magnetic field.

As a result of the last two points it can be said that the general effect of MHD is the reduction or vanishing of the relative movement between the fluid and the imposed magnetic field. Although this general effect is true in every case where MHD is present, there are several parameters which have influence over MHD.

These parameters, that are reviewed in section 3.5.3 together with the dimensionless numbers used at MHD phenomena, led to different outcomes on the MHD phenomena.

Basically MHD phenomena can be divided in two groups based in the characteristic length of the phenomena. When the characteristic length of the phenomena is very large as in astrophysics and geophysics, MHD phenomena is highly dominated by the advection of the magnetic field. This advection of the magnetic field gives origin to phenomena like Alfvén waves. If the characteristic length of the phenomena is not really large, like in the engineering applications, the advection of the magnetic field is less dominant, although it is still present. This research is focused in engineering applications where there is advection of the magnetic field but not as dominant as in astrophysical applications.

2.3 Applications of MHD in Materials Processing

Roughly speaking magnetic fields can be employed to melt, pump, stir and levitate liquid metals during foundry operations. Although the basic idea behind the use of magnetic field to manipulate liquid metals dates from 1917, it was not until the early 1980's when the term *Metallurgical MHD* was coined.

The main advantage of MHD in metallurgy is the fact that it offers a way to apply non invasive volumetric forces over the liquid metals. This non invasive way to manipulate liquid metals avoids the inclusion of impurities in the final cast.

2.3.1 Stirring of Liquid Metals

Today, the most used process in the metallurgical industry is continuous casting. This process consists in pouring the molten metal into a mold where it partially solidifies and then it is extracted. In this method, slabs are continuous, therefore the name of the process. The process is depicted in figures 2.1 and 2.2.

As can be seen in figure 2.2, the slab solidifies from a liquid metal reservoir. This reservoir is refilled and the process is a non stop operation. Several defects can appear in the slab during the continuous casting operation. Such defects can be segregated alloying elements, non metallic inclusions, small cavities due to the formation of gas bubbles and center–line porosities associated with shrinkage of metal during solidification. All of these defects can be reduced, if not eliminated at all, stirring the liquid metal before solidification. The stirring favors the homogeneity of the mixture ruling out the defects. Given the fact that stirring by mechanical means will contaminate the mixture, MHD non invasive means offer the perfect way to stir the metallic mixture.

The method used to stir the metallic mixture using magnetic fields is similar to the operation of induction motors. Electromagnets are placed near the mold and the rotating electromagnetic field produced stirs the liquid metal. Figure 2.3 shows the general set–up of these electromagnets in the continuous casting process.

Figure 2.1 *Continuous Casting Process*

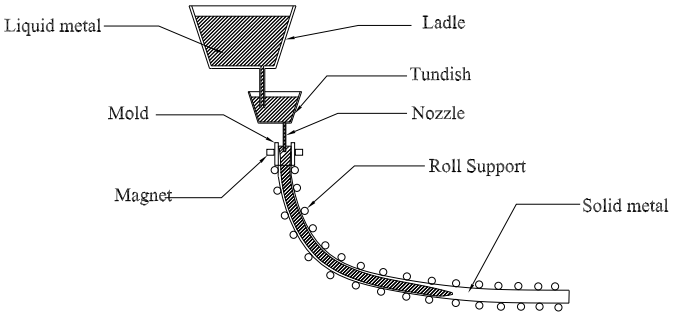

Figure 2.2 *Schematic Continuous Casting Process*

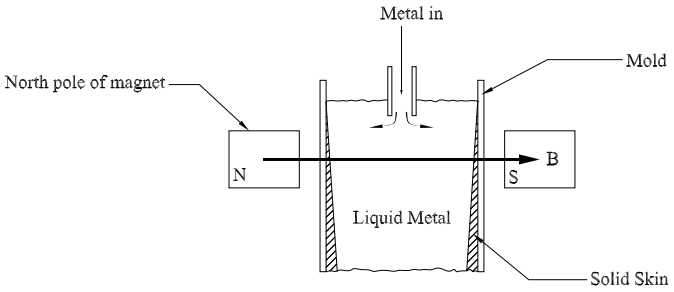

Figure 2.3 *Electromagnets in the Continuous Casting Process*

2.3.2 Damping of Movements in Liquid Metals

The method to stir liquid metals using rotating magnetic fields was discussed briefly in the last section. Some times what is needed is the suppression rather than the production of movements in the fluid. This suppression of the movements inside the fluid can be achieved using strong stationary magnetic fields. The physical mechanism behind the suppression is that the movement of the fluid through the lines of the magnetic field induces a electric current and therefore a Joule dissipation. This Joule dissipation gives origin to a lost of kinetic energy which transforms in thermal energy.

Roughly speaking, the application of strong stationary magnetic fields to liquid metals seeks the suppression of movements in the free surface of the liquid metal to avoid the entrance of any debris inside the liquid metal. This debris usually are oxides and other materials which form a scum in the surface of the liquid metal. The case of a jet of liquid metal feeding a mold is the most frequent one where the movement must be damped.

In some cases the movement is caused by natural convection and a strong stationary magnetic field can be used in order to suppress the perturbations in the liquid metal. These perturbations often affect negatively the quality of the crystalline structure. The crystalline structure is fundamental in industries like the semiconductor industry, where Bridgeman and Czochralski methods are widely used to make monocrystal semiconductor ingots that are cut in slices in order to manufacture semiconductor devices as photovoltaic cells and integrated circuits. Figure 2.4 shows one of the ingots obtained in the Czochralski process.

Figure 2.4 *Silicon Ingot obtained by Czochralski Crystal Growth Process*

In figure 2.5 the Czochralski method is depicted. In this case the objective is to produce a semiconductor mono–crystal. As it was said, applying a strong stationary magnetic field, the movements of the fluid due to differences in temperature are damped. This leads to a more regular mono–crystal with less defects.

2.3.3 Instabilities in Interfaces

In this section, a particular application of MHD for a specific metal is discussed, contrary to the sections 2.3.1 and 2.3.2 where general applications were discussed. Today most aluminum in the world is produced using the Hall– Héroult process. In this process alumina is dissolved in a bath of molten cryolite. The mixture

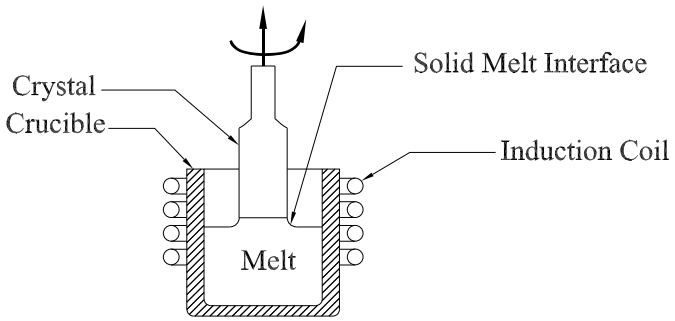

Figure 2.5 *Czochralski Crystal Growth Process*

is electrolyzed using an electric current between 180 kA and 350 kA, and liquid aluminum is produced at the cathode. The liquid aluminum is denser than the cryolite and it sinks to the bottom of the bath where it is collected. In figure 2.6 the reduction cells used in this process are depicted.

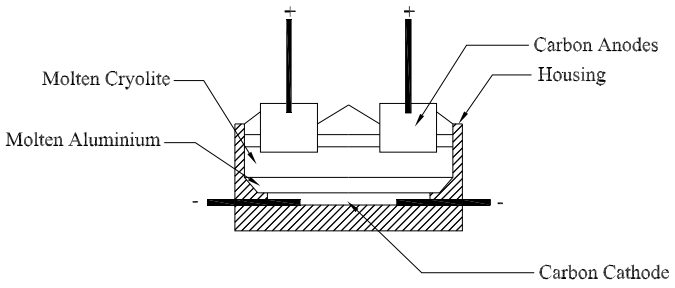

Figure 2.6 *Aluminum Reduction Cell*

The biggest concern when using the Hall–Héroult method is the huge need of electrical power. Being the cryolite the material with the biggest resistivity its level must be kept at the minimum to reduce the consumption of electricity. Nevertheless, the level of cryolite must be high enough to prevent perturbations in the interface between aluminum and cryolite, which under certain conditions can stop the production of aluminum. Therefore the level of cryolite must be the smallest one which assures stable operation with minimum consumption of electric power. The MHD equations for incompressible fluids are the governing equations of the fluids involved in the instabilities in reduction cells. Although the basic mechanism behind the instabilities is already understood, numerical simulations of this process are necessary in order to completely understand the phenomenon.

2.3.4 Cold Crucibles

Some metals like titanium or nickel are highly reactive and have a tendency to attack refractory walls of conventional furnaces. In order to deal with such metals cold crucibles are often used. These devises are designed to melt and cast the metal in a single operation. The lower part of the cold crucible acts like a casting mold and the upper part acts like an induction furnace. This devise is known as cold crucible because the liquid metal is held in a water cooled cooper crucible. Figures 2.7 and 2.8 show a real cold crucible and its schematic representation respectively.

Figure 2.7 *Cold Crucible*

In order to heat the metal properly the cold crucible design must allow the magnetic field to pass through the conducting walls. This is achieved segmenting the wall and isolating each segment so that the eddy currents are forced to circulate in each segment. In this way a smooth distribution of the current in the inner surface of the wall generates a magnetic field inside the crucible.

The cold crucible process has the potential to produce high purity parts of a

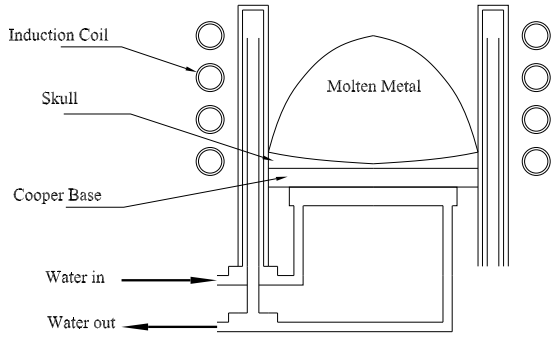

Figure 2.8 *Schematic View of a Cold Crucible*

wide variety of materials ranging from aerospace alloys to biocompatible materials for surgical implants and silicon for photovoltaic and electronic applications.

2.3.5 Electromagnetic Separation of Inclusions

One of the main problems in metallurgy is the contamination of molten metals with small solid inclusions. These inclusions are mainly oxides and carbides with a melting point higher than the metal. These inclusions are harmful for the quality of the final cast. Generally speaking these non metallic inclusions reduce the mechanical properties and increase the risk of corrosion. The aim is to remove the inclusions from the liquid metal before it solidifies. Figure 2.9 shows two non metallic inclusions under the microscope.

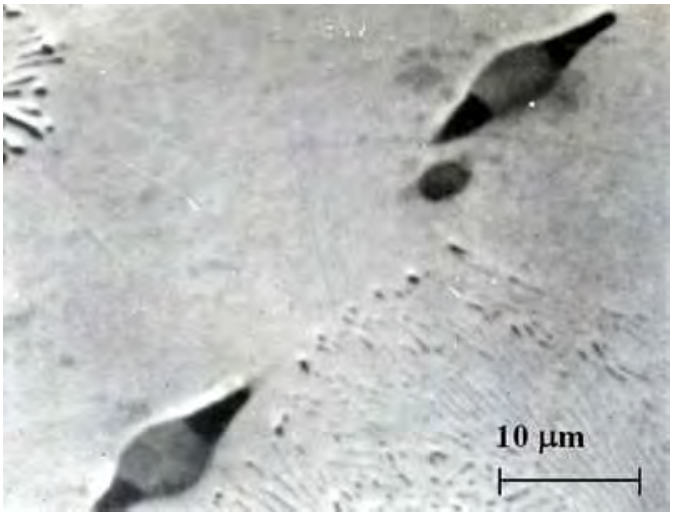

Figure 2.9 *Non Metallic Inclusions*

The most conventional methods to achieve the inclusions separation are sedi-

mentation and filtration. Sedimentation is limited by the size of the particles being removed because it cannot remove particles smaller than $100\mu\,m$. Filtration can remove particles smaller than 30 μm but often the ceramic filters used in this process contaminate the liquid metal after some time of use. In order to remedy the shortcomings of these two methods of separation, electromagnetic techniques are being investigated.

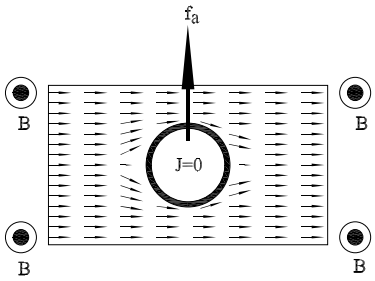

Figure 2.10 *Schematic view of Archimides Electromagnetic Force*

Basically the electromagnetic separation technique requires an externally imposed magnetic field to induce a flotation force in the non metallic inclusions. As can be seen in figure 2.10 the current density travels left to right in the molten metal. Given the fact that the particles are non metallic and nonconducting, there is no current inside the particles. The imposed magnetic field is applied pointing out the plane. The resulting Lorentz's Force points downwards. The particles present in the molten metal experience an opposite force, called Archemides Electromagnetic Force, as a result of Newton's third law. Although the electromagnetic separation process has been investigated since early 1960's, no generally accepted technique has been obtained.

Chapter 3

Governing Equations of Magnetohydrodynamics

3.1 Introduction

The main goal of this chapter is to present the governing equations of Magnetohydrodynamics. MHD is a branch of Physics that can be thought as the intersection of Fluid Mechanics and Electromagnetism, therefore the Navier–Stokes equations and the Maxwell equations are presented. First, the Navier–Stokes equations are presented briefly but as clear as possible, because these equations are usually well known. Following, the Maxwell equations are presented, paying attention to its differential form, constitutive equations and boundary conditions. The theory behind Lorentz force is also reviewed because Lorentz force is the link between mechanical and electromagnetic phenomena. The general magnetohydrodynamic problem is a quite complex task and therefore some approximations must be made in order to obtain a satisfactory solution the MHD problem. These approximations are also discussed in this chapter. The final general form of the equations of Magnetohydrodynamics is reviewed and discussed together with the way in which thermal coupling is handled through Boussinesq approximation. The non dimensional form is also reviewed. Finally the last section of this chapter is devoted to present the Hartmann flow, which can be considered the archetype of MHD flows.

3.2 Navier Stokes Equations

The Navier–Stokes equations are the governing equations for the behavior of Newtonian fluids, which are fluids that exhibit a linear relation between the velocity and the shear stress. These equations where originally proposed by the French engineer Claude–Louis–Marie–Henry Navier (1785–1836) in 1822. In the original Navier's work, he proposed a law of interaction between molecules totally inconsistent from the physical point of view, and in 1845 the English physicist George Gabriel Stokes

(1819–1903) correctly derived the same equations using an approach based in theory of continua. The Navier–Stokes equations are derived from a mass balance and a momentum balance for incompressible fluids. This analysis stars from the continuity equation:

$$\frac{1}{\rho}\frac{D\rho}{Dt} + \nabla \cdot \mathbf{u} = 0 \tag{3.2.1}$$

The derivative $\frac{D\rho}{Dt}$ is the rate of change of density following a fluid particle. The fluids under study are incompressible, therefore the density cannot change over time, that is, ρ is constant and the continuity equation becomes:

$$\nabla \cdot \mathbf{u} = 0. \tag{3.2.2}$$

Once the mass balance has been performed, the momentum balance is presented. Starting with the Cauchy equation of motion:

$$\rho\frac{D\mathbf{u}}{Dt} = \nabla \cdot \boldsymbol{\sigma} + \rho\mathbf{f} \tag{3.2.3}$$

where ρ is the mass density ($kilogram\ meter^{-3}$) of the fluid, $\boldsymbol{\sigma}$ is the stress tensor, $\mathbf{f}$ is the body force per unit mass and $\mathbf{u}$ is the velocity of the fluid ($meter\ second^{-1}$). $\frac{D(\bullet)}{Dt}$ is the material derivative and is defined as:

$$\frac{D(\bullet)}{Dt} = \frac{\partial(\bullet)}{\partial t} + (\mathbf{u} \cdot \nabla)(\bullet) \tag{3.2.4}$$

and $(\mathbf{u} \cdot \nabla)(\bullet)$ is the convective derivative. In the case of an incompressible fluid $\boldsymbol{\sigma}$ can be defined by the constitutive equation:

$$\boldsymbol{\sigma} = -p\mathbf{I} + 2\mu\mathbf{D} \tag{3.2.5}$$

where $\mathbf{D}$ is the rate of deformation tensor defined as:

$$\mathbf{D} = \frac{1}{2}\left[(\nabla\mathbf{u}) + (\nabla\mathbf{u})^T\right] \equiv \nabla^S\mathbf{u} \tag{3.2.6}$$

and μ is the dynamic viscosity ($kilogram\ meter^{-1} second^{-1}$). $\nabla^S\mathbf{u}$ is known as the symmetrical gradient of $\mathbf{u}$. If the expression (3.2.4) for $\mathbf{u}$ and the expression (3.2.5) together with (3.2.2) are substituted into (3.2.3) the Navier–Stokes equations for a Newtonian incompressible fluid are obtained:

$$\frac{\partial\mathbf{u}}{\partial t} + (\mathbf{u}\cdot\nabla)\,\mathbf{u} - \nu\Delta\mathbf{u} + \frac{1}{\rho}\nabla p = \mathbf{f} \tag{3.2.7}$$

In the last expression ν is the kinematic viscosity ($meter^2\ second^{-1}$) and is related to the dynamic viscosity μ by the expression $\nu = \mu/\rho$. Readers interested in a more detailed derivation of the Navier–Stokes equations are referred to classical books as Landau[40] and Batchelor [6].

In order to properly describe the behavior of Newtonian incompressible fluids equations (3.2.7) and (3.2.2) are the only equations needed. These equations relate

the velocity field $\mathbf{u} = \mathbf{u}(\mathbf{x}, t)$ with the pressure $p = p(\mathbf{x}, t)$ evaluated both at a point $\mathbf{x} \in \Omega$ and a time $t \in [0, T]$. The physical domain $\Omega \subset \Re^n$ where $n = 2, 3$ is the place where the variables are under study. Finally in order to properly solve the Navier–Stokes equations, initial and boundary conditions are needed. These conditions are:

$$\mathbf{u}(\mathbf{x}, 0) = \mathbf{u}_0, \quad \mathbf{x} \in \Omega \tag{3.2.8}$$

$$\mathbf{u}(\mathbf{x}, t) = 0, \quad \mathbf{x} \in \partial\Omega \tag{3.2.9}$$

The expression (3.2.9) is the so called *non slip boundary condition* and it is a restriction over the velocity of the fluid that must be null in any solid wall at rest which has contact with the fluid. This boundary condition was adopted for the sake of simplicity, although other conditions will be needed in the applications.

3.3 Maxwell Equations

The Maxwell equations rule the behavior of electromagnetic phenomena. Although these equations bear the name of the Scottish physicist James Clerk Maxwell (1831–1879), they were well known before the scientific work of Maxwell. The reason to name these equations after Maxwell is the fact that he was the first to present them in a unified way to explain the electromagnetic phenomena. Maxwell also modified the Ampère law to include the effect of time–varying electric fields over magnetic fields, the so called *displacement current*, $\frac{\partial \mathbf{D}}{\partial t}$ in Ampère law.

Maxwell presented these equations in a paper to the Royal Society in 1865 [43]. In that paper he presented the equations in scalar notation because at that time, vectorial notation was not developed yet. It was not until 1892 when Oliver Heaviside, an English electric engineer, rewrote these equations in the modern vectorial notation [28].

3.3.1 General Differential Form

In order to describe the electromagnetic phenomena, the Maxwell equations use four vector fields. These vector fields are functions of position $\mathbf{x} \in \Re^3$, and time $t \in \Re^+$, in others words, they are functions of $\Re^n \times (0, \infty)$ into $\Re^n$, where $n = 2, 3$. The vector fields are:

$\mathbf{B}(\mathbf{x}, t)$, Magnetic Flux Density ($Tesla$).

$\mathbf{H}(\mathbf{x}, t)$, Magnetic Field Strength ($Ampere\ meter^{-1}$).

$\mathbf{D}(\mathbf{x}, t)$, Electric Flux Density ($Coulomb\ meter^{-2}$).

$\mathbf{E}(\mathbf{x}, t)$, Electric Field Strength ($Volt\ meter^{-1}$).

These four vector fields together describe the electromagnetic field, which is created by a distribution of sources consisting of static electric charges and flows of electric charges. The Maxwell equations apply over the whole space $\Re^n$ occupied by the electromagnetic field and are:

$$\frac{\partial \mathbf{B}}{\partial t} + \nabla \times \mathbf{E} = \mathbf{0} \tag{3.3.1}$$

$$\frac{\partial \mathbf{D}}{\partial t} - \nabla \times \mathbf{H} = -\mathbf{J} \tag{3.3.2}$$

$$\nabla \cdot \mathbf{D} = \rho_e \tag{3.3.3}$$

$$\nabla \cdot \mathbf{B} = 0 \tag{3.3.4}$$

where ρ_e is the electric charge density ($Coulomb\ meter^{-3}$) and $\mathbf{J}$ is the electric current density ($Ampere\ meter^{-2}$). In order to clarify the concepts it is useful to mention that a electric current is the flow of q, an electric charge ($Coulomb$) .

Equation (3.3.1) is called Faraday's law and it states the relation between a time–varying magnetic field and an electric field. Equation (3.3.2) is called Ampère–Maxwell law and it states that both time–varying electric field and electric currents give origin to magnetic fields. The Divergence condition (3.3.3) over electric fields gives the effect of charge density over electric flux density. Finally the divergence condition (3.3.4) over magnetic field states that there are no magnetic monopoles. Readers interested in a more detailed explanation about the Maxwell equation are referred to the classical book of Landau [39]. Together with the Maxwell equations, it is important to mention the continuity equation for electric charge:

$$\nabla \cdot \mathbf{J} + \frac{\partial \rho_e}{\partial t} = 0 \tag{3.3.5}$$

It is worthy of attention the fact that the divergence conditions (3.3.3) and (3.3.4) can be derived from Faraday law (3.3.1) and Ampère–Maxwell equation (3.3.2), provided charge is conserved, that is, while (3.3.5) is valid. This fact does not mean that these two divergence conditions can be entirely dismissed from a mathematical model of an electromagnetic phenomena. In any case the divergence conditions (3.3.3) and (3.3.4) must be true at $t = 0$.

3.3.2 General Integral Form

Some authors prefer to state equations (3.3.1)–(3.3.4) in its integral form. This integral form can be obtained applying Gauss's and Stokes's theorems to the Maxwell equations. Although in this work the integral form will not be used, it is presented for reference purposes:

$$\oint_C \mathbf{E} \cdot d\mathbf{l} = -\frac{d}{dt} \int \int_S \mathbf{B} \cdot d\mathbf{s} \tag{3.3.6}$$

$$\oint_C \mathbf{H} \cdot d\mathbf{l} = \frac{d}{dt} \int \int_S \mathbf{D} \cdot d\mathbf{s} + \int \int_S \mathbf{J} \cdot d\mathbf{s} \tag{3.3.7}$$

$$\oint_S \mathbf{D} \cdot d\mathbf{s} = \int \int \int_V \rho_e dv \tag{3.3.8}$$

$$\oint_S \mathbf{B} \cdot d\mathbf{s} = 0 \tag{3.3.9}$$

In order to properly explain equations (3.3.6)–(3.3.9) let us consider figures 3.1–3.4. Figure 3.1 explains Faraday's law (3.3.6), which relates the voltage induced in a loop (C) by a time–varying magnetic flux density passing through the surface S formed by the loop.

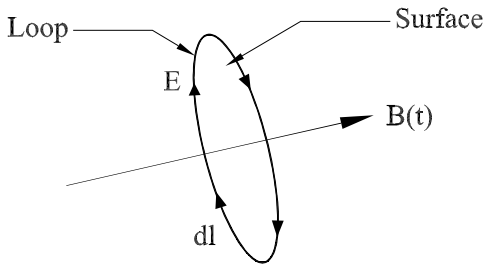

Figure 3.1 *Material surface for the integral form of Faraday law*

Figure 3.2 explains Ampère–Maxwell law (3.3.7), which relates the scalar magnetic potential induced in a loop (C) by the current and the time–varying electric field passing through the surface S formed by the loop.

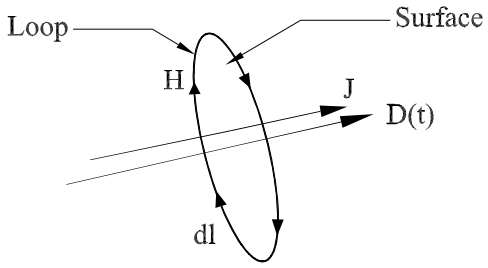

Figure 3.2 *Material surface for the integral form of Ampère law*

Figure 3.3 explains Gauss's law for electric fields (3.3.8). This law states that the electric flux emanating from a bounded volume V equals the total charge enclosed in that volume. Finally figure 3.4 explains Gauss's law for magnetic fields(3.3.9).

This law states that no magnetic flux emanates from a bounded domain, in others words, there are no magnetic monopoles in nature.

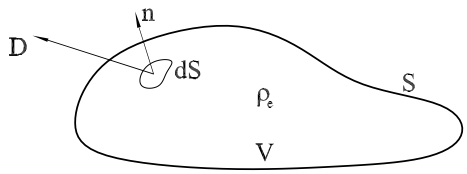

Figure 3.3 *Material volume for the integral form of Gauss law for the electric flux D*

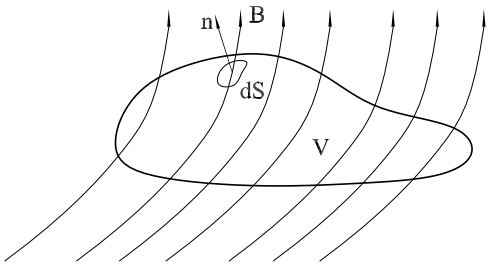

Figure 3.4 *Material surface for the integral form of Gauss law for the magnetic flux B*

3.3.3 Lorentz Force

The Lorentz force is the link between mechanical and electromagnetic phenomena. In the case of MHD, it provides one of the two coupling mechanism between the Navier–Stokes equations and the Maxwell equations. In order to present the Lorentz force, this discussion starts with the force over a single particle. The total force exerted over a particle is given by expression (3.3.10). The particle travels with velocity $\mathbf{u}$ in the presence of an electric field and a magnetic field, and has an electric charge q:

$$\mathbf{f} = q\mathbf{E}_s + q\mathbf{E}_i + q\mathbf{u} \times \mathbf{B} \tag{3.3.10}$$

The first force $q\mathbf{E}_s$ is the Coulomb Force, which arises from the repulsive or attractive forces charged particles exert over other charged particles. The second force $q\mathbf{E}_i$ is originated by the induced electric field $\mathbf{E}_i$. Induced electric fields arise when a variable magnetic field is present, as stated by Faraday's law. The third

and last force, $q\mathbf{u} \times \mathbf{B}$, is the force exerted over a charged particle which travels with velocity $\mathbf{u}$ in a magnetic field. This force is called Lorentz Force and as it can be seen, if the particle stops the force will vanish.

At this point it is important to focus upon electric and magnetic fields in moving reference frames. In the case of a magnetic field and an electric field present in a laboratory reference frame and a charged particle moving in this laboratory frame, the force over the particle is due to the electric field and the magnetic field, $\mathbf{f} = q\mathbf{E} + q\mathbf{u} \times \mathbf{B}$.

But if in order to measure the force, a different reference frame is used, and this reference frame moves in such way that the particle appears to be instantaneously at rest, the force over the particle is $\mathbf{f}_r = q\mathbf{E}_r$. This fact provides a way to link the electric fields in both reference frames, because $\mathbf{f} = \mathbf{f}_r$, and therefore the electric fields are related by:

$$\mathbf{E}_r = \mathbf{E} + \mathbf{u} \times \mathbf{B} \tag{3.3.11}$$

It is important to emphasize the fact that magnetic fields $\mathbf{B}$ and $\mathbf{B}_r$ are the same. Taking back the discussion to forces over charged particles, the expression (3.3.10) can be summarized as:

$$\mathbf{f} = q(\mathbf{E} + \mathbf{u} \times \mathbf{B}) \tag{3.3.12}$$

where the forces over the charged particle are due only to the electric field and to the Lorentz force. Expression (3.3.12) has a volumetric equivalent:

$$\mathbf{F} = \rho_e\mathbf{E} + \mathbf{J} \times \mathbf{B} \tag{3.3.13}$$

3.3.4 Constitutive Equations

In order to be well–posed, the Maxwell equations must be complemented by two constitutive equations. These constitutive equations relate $\mathbf{E}$ and $\mathbf{H}$ with $\mathbf{D}$ and $\mathbf{B}$, respectively. These constitutive equations are dependent on the material properties of the media, where the electromagnetic phenomena take place. In the following, three different scenarios are described for these constitutive equations:

1. Free Space
   If the domain where the magnetic field is located is vacuum, the constitutive equations are:

   $$\mathbf{D} = \epsilon_0\mathbf{E} \tag{3.3.14}$$

   and

   $$\mathbf{B} = \mu_0\mathbf{H} \tag{3.3.15}$$

   where ϵ_0 and μ_0 are called the electric permittivity and the magnetic permeability for the free space. The values of these constants are: $\epsilon_0 \approx 8.854 \times$

$10^{-12} Farad\ meter^{-1}$ and $\mu_0 = 4\pi \times 10^{-7} Henry\ meter^{-1}$. It is also important to mention that $c = (\epsilon_0 \mu_0)^{-1/2}$, where c is the speed of the light in vacuum ($c \approx 2.998 \times 10^8 meter\ second^{-1}$)

2. Isotropic Materials
   In case the properties of the media do not depend upon the direction and the material is linear, the constitutive equations are:

$$\mathbf{D} = \epsilon \mathbf{E} \tag{3.3.16}$$

   and

$$\mathbf{B} = \mu_m \mathbf{H} \tag{3.3.17}$$

   where ϵ and μ_m[1] are called the electric permittivity and the magnetic permeability for specific material. Both ϵ and μ_m are positive scalars.

3. Anisotropic Materials
   Some materials have electromagnetic properties which depend upon the direction. In such cases the electric permittivity and the magnetic permeability in (3.3.16) and (3.3.17) become positive definite tensors.

Ohm's Law must be mentioned together with these constitutive equations because, although it is not a fundamental law of electromagnetism, it is quite important and can be considered as a constitutive equation. If the case of a stationary conductor is considered, Ohm's Law can be enunciated as:

$$\mathbf{J} = \sigma \mathbf{E} \tag{3.3.18}$$

where σ is the conductivity ($Siemens\ meter^{-1}$). In case of a conductor in movement is considered, Ohm's law is the same but the electric field must be measured in a frame of reference. Such frame of reference must be moving with the same velocity as the conductor. In order to measure the electric field in a moving reference frame expression (3.3.11) must be used. Therefore expression (3.3.18) becomes:

$$\mathbf{J} = \sigma \mathbf{E_r} = \sigma(\mathbf{E} + \mathbf{u} \times \mathbf{B}) \tag{3.3.19}$$

3.3.5 Boundary Conditions at Interfaces

As any set of partial differential equations, the Maxwell equations must have boundary conditions to be well–posed. In order to properly describe the different boundary conditions that arise in electromagnetic phenomena, the situation depicted in figure 3.5 is analyzed.

[1] Almost all textbooks in Electromagnetism use μ for the magnetic permeability. In order to distinguish the magnetic permeability from dynamic viscosity, μ_m will be used for the former and μ for the latter.

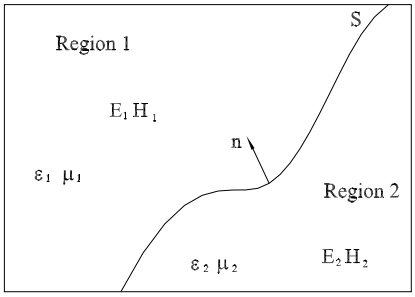

Figure 3.5 *Boundary conditions in the interface between two regions*

Region 1 and region 2 have different magnetic properties and are divided by an interface S with unit normal $\widehat{\mathbf{n}}$, pointing from region 2 into region 1. For this situation, four different boundary conditions, known as *field continuity conditions*, arise. These conditions are:

$$\widehat{\mathbf{n}} \times (\mathbf{E_1} - \mathbf{E_2}) = \mathbf{0} \tag{3.3.20}$$

$$\widehat{\mathbf{n}} \cdot (\mathbf{D_1} - \mathbf{D_2}) = \mathbf{0} \tag{3.3.21}$$

$$\widehat{\mathbf{n}} \times (\mathbf{H_1} - \mathbf{H_2}) = \mathbf{0} \tag{3.3.22}$$

$$\widehat{\mathbf{n}} \cdot (\mathbf{B_1} - \mathbf{B_2}) = \mathbf{0} \tag{3.3.23}$$

Only two of four conditions must be used. One from (3.3.20) and (3.3.23) and one from (3.3.21) and (3.3.22). If the interface has an imposed current density, $\mathbf{J}_s$ or surface charge density, ρ_s, (3.3.21) and (3.3.22) must be modified to:

$$\widehat{\mathbf{n}} \cdot (\mathbf{D_1} - \mathbf{D_2}) = \rho_s \tag{3.3.24}$$

$$\widehat{\mathbf{n}} \times (\mathbf{H_1} - \mathbf{H_2}) = \mathbf{J}_s \tag{3.3.25}$$

If one of the two materials of the interface is a perfect conductor, the electric field in that region will vanish and the boundary conditions become:

$$\widehat{\mathbf{n}} \times \mathbf{E_1} = \mathbf{0} \tag{3.3.26}$$

Expression (3.3.26) is valid if the region 2 is the perfect conductor. If the material in region 2 is not a perfect conductor but an imperfect conductor and allows the electric field to penetrate only a small distance, a better boundary condition would be the so called *impedance boundary condition*:

$$\widehat{\mathbf{n}} \times \mathbf{H_1} - \lambda(\widehat{\mathbf{n}} \times \mathbf{E_1}) \times \widehat{\mathbf{n}} = \mathbf{0} \tag{3.3.27}$$

where λ is the impedance (Ohm) and it is a positive function over the surface S of the material.

3.4 The MHD Approximation

The solution of magnetohydrodynamics equations in its full form is a rather complex task, therefore, in order to ease the difficulties, some approximations are assumed. The approximation is completely consistent with the conditions assumed in this work for liquid metals. These approximations together are named the *MHD Approximation* and are enumerated next:

1. **Non relativistic velocity of the fluid.** The velocity, in phenomena where processing techniques use MHD, is far away from relativistic velocities. Given the fact that $|u|^2 \ll c^2$, it is completely possible to use a Newtonian reference frame because the *Lorentz factor* γ, is near unity. The Lorentz factor is defined as:

$$\gamma = \sqrt{1 - \left(\frac{|u|^2}{c^2}\right)} \tag{3.4.1}$$

and it is present in the Lorentz transformation which converts measurements of space and time between two different frames, where one frame is in relative motion with respect to the other. Let us consider two frames of reference O and Q, where O uses (t, x, y, z) and Q uses (t', x', y', z') as Cartesian coordinates to measure space and time and assume that the x axis and the x' axis overlap and the y axis and the z axis are parallel to the y' axis and the z' axis respectively. If relative velocity between O and Q is v along the common x axis, the Lorentz transformation is:

$$\begin{aligned} t' &= \gamma\left(t - \frac{vx}{c^2}\right) \\ x' &= \gamma\left(x - vt\right) \\ y' &= y \\ z' &= z \end{aligned} \tag{3.4.2}$$

In the case of $\gamma \approx 1$, the well known Galilean transformation is recovered:

$$\begin{aligned} t' &= t \\ x' &= (x - vt) \\ y' &= y \\ z' &= z \end{aligned} \tag{3.4.3}$$

2. **The Induced magnetic field is small.** It is assumed that the induced magnetic field is much smaller than the applied magnetic field. This assumption also implies that the electric field is of order $\mathbf{u} \times \mathbf{B}$.

3. **Phenomena involving high frequency are not considered.** It is assumed that the displacement current $\frac{\partial \mathbf{D}}{\partial t}$ can be neglected compared with $\mathbf{J}$, the conduction current. This approximation modifies Ampère law (3.3.2), and it takes the form:

$$\nabla \times \mathbf{H} = \mathbf{J} \tag{3.4.4}$$

   which is some times called the pre–Maxwell Ampère law. This approximation also implies that the working fluid is a conductor rather than a dielectric. This is due to the fact that in dielectrics, even for low frequencies, $\frac{\partial \mathbf{D}}{\partial t}$ is still larger than $\mathbf{J}$, which is null.

4. **Electric energy can be neglected when compared with magnetic energy.** This means that the principal interaction takes place between the magnetic field and the fluid.

5. **Space charge can be neglected.** Space charge ρ_e can be neglected in some expressions. The first expression where ρ_e is neglected is the volumetric Lorentz force (3.3.13). The electrostatic force $\rho_e \mathbf{E}$, when compared with the Lorentz force $\mathbf{J} \times \mathbf{B}$, turns out to be negligible and expression (3.3.13) takes the form:

$$\mathbf{F} = \mathbf{J} \times \mathbf{B} \tag{3.4.5}$$

   Space charge can also be neglected in the equation of conservation of charge and therefore $\frac{\partial \rho_e}{\partial t} = 0$, because any net charge that lies in the interior of a conductor will move to the surface almost immediately by the action of electrostatic repulsion forces. The equation of conservation of charges takes the form:

$$\nabla \cdot \mathbf{J} = 0 \tag{3.4.6}$$

3.5 MHD Equations

This section is devoted to present the final general form of the magnetohydrodynamics equations. The deduction of the induction equation is presented and the final form of the MHD equations is also presented. The thermal coupling is discussed and finally the dimensionless form of the MHD equations is presented.

3.5.1 General Form

Equations (3.2.7) and (3.2.2) for the fluid phenomena and equations (3.3.1), (3.4.4), (3.3.4), (3.3.17), (3.3.19) and (3.4.5) for the electromagnetic phenomena are all that is needed to develop the MHD equations. Summarizing, the equations are:

$$\frac{\partial \mathbf{u}}{\partial t} + (\mathbf{u}\cdot\nabla)\,\mathbf{u} - \nu\Delta\mathbf{u} + \frac{1}{\rho}\nabla p = \mathbf{f}$$

$$\nabla \cdot \mathbf{u} = 0$$

$$\frac{\partial \mathbf{B}}{\partial t} + \nabla \times \mathbf{E} = \mathbf{0}$$

$$\nabla \times \mathbf{H} = \mathbf{J}$$

$$\mathbf{B} = \mu_m \mathbf{H}$$

$$\nabla\cdot\mathbf{B} = 0$$

$$\mathbf{J} = \sigma\,(\mathbf{E} + \mathbf{u} \times \mathbf{B})$$

$$\mathbf{F} = \mathbf{J} \times \mathbf{B}$$

In order to deduce the complete system of MHD equations, the electric field must be obtained from Ohm's law (3.3.19):

$$\mathbf{E} = \frac{1}{\sigma}\mathbf{J} - \mathbf{u} \times \mathbf{B} \tag{3.5.1}$$

The current $\mathbf{J}$ is also needed, and it is obtained after $\mathbf{H}$ from (3.3.17) is substituted into pre–Maxwell Ampère's law (3.4.4)

$$\mathbf{J} = \frac{1}{\mu_m}\,(\nabla \times \mathbf{B}) \tag{3.5.2}$$

Now expressions (3.5.1) and (3.5.2) are substituted into Faraday's law (3.3.1) and after proper reorganization the so called induction equation is obtained:

$$\frac{\partial \mathbf{B}}{\partial t} + \frac{1}{\mu_m \sigma}\nabla \times (\nabla \times \mathbf{B}) - \nabla \times (\mathbf{u} \times \mathbf{B}) = 0 \tag{3.5.3}$$

Equation (3.5.3) relates the magnetic field and the velocity of the conducting fluid. μ_m and σ are positive constants already defined in section 3.3.4. It is also necessary to substitute the expression (3.5.2) into the Lorentz force (3.4.5) and divide between the density ρ to get an expression for the force over the fluid:

$$\mathbf{f} = \frac{1}{\mu_m \rho} (\nabla \times \mathbf{B}) \times \mathbf{B}. \tag{3.5.4}$$

The force over the fluid (3.5.4) exerted by the magnetic field is really part of the right hand side of the equation (3.2.7). In order to have all unknowns in the left hand side of this equation the Lorentz force is put in the left hand side of that equation, and it takes the final form of:

$$\frac{\partial \mathbf{u}}{\partial t} + (\mathbf{u} \cdot \nabla)\mathbf{u} - \nu \Delta \mathbf{u} + \frac{1}{\rho} \nabla p - \frac{1}{\mu_m \rho} (\nabla \times \mathbf{B}) \times \mathbf{B} = \mathbf{f_u} \tag{3.5.5}$$

Arranging the equations the complete system of MHD equations is:

$$\begin{aligned} \frac{\partial \mathbf{u}}{\partial t} + (\mathbf{u} \cdot \nabla)\mathbf{u} - \nu \Delta \mathbf{u} + \frac{1}{\rho} \nabla p - \frac{1}{\mu_m \rho} (\nabla \times \mathbf{B}) \times \mathbf{B} &= \mathbf{f_u} \\ \nabla \cdot \mathbf{u} &= 0 \\ \frac{\partial \mathbf{B}}{\partial t} + \frac{1}{\mu_m \sigma} \nabla \times (\nabla \times \mathbf{B}) - \nabla \times (\mathbf{u} \times \mathbf{B}) &= \mathbf{f_b} \\ \nabla \cdot \mathbf{B} &= 0 \end{aligned} \tag{3.5.6}$$

where $\mathbf{f_u}$and $\mathbf{f_b}$ are force vectors for the fluid and the magnetic field respectively. System (3.5.6) is all that is needed to completely describe isothermal MHD phenomena.

3.5.2 Thermal Coupling

If the fluid has thermal fluctuations at the same time than the MHD phenomena takes place, it is mandatory to use the thermal energy equation, which under the Boussinesq approximation (i.e. flow speed is small compared with the speed of sound and temperature differences in the fluid are small) can be simplified to:

$$\rho c_p \left(\frac{\partial \vartheta}{\partial t} + (\mathbf{u} \cdot \nabla)\, \vartheta \right) - \nabla \cdot (k_t \nabla \vartheta) - \mathbf{J} \cdot \mathbf{E} - \Phi(\mathbf{u}) = Q \tag{3.5.7}$$

where: c_p is the specific heat, k_t is the heat conductivity, ϑ is the temperature, $\Phi(\mathbf{u})$ is the rate of viscous dissipation and Q is the heat source. The term $\mathbf{J} \cdot \mathbf{E}$ is the Joule heating and it is the process by which the flow of an electric current through a conductor releases heat. If the current in the term $\mathbf{J} \cdot \mathbf{E}$ is substituted using expression (3.5.2) and the electric field is substituted by (3.5.1) the next expression for $\mathbf{J} \cdot \mathbf{E}$ can be obtained:

$$\mathbf{J} \cdot \mathbf{E} = \frac{1}{\mu_m^2 \sigma} \|\nabla \times \mathbf{B}\|^2 \tag{3.5.8}$$

It is also necessary define the rate of viscous dissipation $\Phi(\mathbf{u})$ in equation (3.5.7) as:

$$\Phi(\mathbf{u}) = 2\mu\, \mathbf{D} : \mathbf{D} \tag{3.5.9}$$

It is important to recall that Boussinesq approximation assumes that the variations on ρ are negligible except for the body force $\rho\mathbf{g}$ where $\mathbf{g}$ is the acceleration of the gravity. In this term it is assumed that the density depends on the temperature in the following way:

$$\rho = \rho_r \left[1 - \hat{\beta}\,(\vartheta - \vartheta_r)\right] \tag{3.5.10}$$

where ρ_r is the reference density, ϑ_r is the reference temperature and $\hat{\beta}$ is thermal expansion coefficient. Considering the previous developments the MHD equations take the form:

$$\begin{aligned}
\frac{\partial \mathbf{u}}{\partial t} + (\mathbf{u}\cdot\nabla)\mathbf{u} - \nu\Delta\mathbf{u} + \frac{1}{\rho_r}\nabla p - \frac{1}{\mu_m \rho_r}(\nabla\times\mathbf{B})\times\mathbf{B} &= \mathbf{f_u} + \mathbf{g}\left[1 - \hat{\beta}\,(\vartheta - \vartheta_r)\right] \\
\nabla\cdot\mathbf{u} &= 0 \\
\frac{\partial \mathbf{B}}{\partial t} + \frac{1}{\mu_m\sigma}\nabla\times(\nabla\times\mathbf{B}) - \nabla\times(\mathbf{u}\times\mathbf{B}) &= \mathbf{f_b} \\
\nabla\cdot\mathbf{B} &= 0 \\
\rho_r c_p\left(\frac{\partial\vartheta}{\partial t} + (\mathbf{u}\cdot\nabla)\vartheta\right) - k_t\Delta\vartheta - \frac{1}{\mu_m^2\sigma}\left\|\nabla\times\mathbf{B}\right\|^2 - \Phi(\mathbf{u}) &= Q
\end{aligned} \tag{3.5.11}$$

3.5.3 Dimensionless Form

Some times it is useful to work with a dimensionless system of equations. The use of such systems gives origin to some dimensionless numbers which offer information about the kind of flow under study. In order to get a non dimensional form of the MHD systems, (3.5.6) and (3.5.11), first the dimensional variables must be replaced with non-dimensionalized variables which are: $\mathbf{u}^* = \mathbf{u}/U_0$, $\mathbf{B}^* = \mathbf{B}/B_0$, $p^* = p/\rho_r U_0^2$, $x^* = x/L_0$, $y^* = y/L_0$, $z^* = z/L_0$, $\vartheta^* = (\vartheta - \vartheta_r)/\Delta\vartheta$ and $t^* = t\,U_0/L_0$, where U_0 is the characteristic velocity of the flow, L_0 is the characteristic length of the flow, B_0 is the characteristic magnetic flux density of the flow, ρ_r is the reference density and $\Delta\vartheta = \vartheta_R - \vartheta_r$, with ϑ_R as the highest temperature of the fluid and ϑ_r the minimum temperature of the fluid. After substituting those non-dimensionalized variables in the equations and regrouping some terms the system (3.5.6) takes the following form:

$$\begin{aligned}
\frac{\partial \mathbf{u}}{\partial t} + (\mathbf{u}\cdot\nabla)\mathbf{u} - \frac{1}{Re}\Delta\mathbf{u} + \nabla p - S\,(\nabla\times\mathbf{B})\times\mathbf{B} &= \mathbf{f_u}\\
\nabla\cdot\mathbf{u} &= 0\\
\frac{\partial \mathbf{B}}{\partial t} + \frac{1}{Rm}\nabla\times(\nabla\times\mathbf{B}) - \nabla\times(\mathbf{u}\times\mathbf{B}) &= \mathbf{f_b}\\
\nabla\cdot\mathbf{B} &= 0
\end{aligned} \tag{3.5.12}$$

and the system (3.5.11) takes the following form:

$$\begin{aligned}
\frac{\partial \mathbf{u}}{\partial t} + (\mathbf{u}\cdot\nabla)\mathbf{u} - \frac{1}{Re}\Delta\mathbf{u} + \nabla p - S\,(\nabla\times\mathbf{B})\times\mathbf{B} &= \mathbf{f_u} + \frac{Gr\,\mathbf{g}}{Re^2 S\,\|\mathbf{g}\|}\vartheta\\
\nabla\cdot\mathbf{u} &= 0\\
\frac{\partial \mathbf{B}}{\partial t} + \frac{1}{Rm}\nabla\times(\nabla\times\mathbf{B}) - \nabla\times(\mathbf{u}\times\mathbf{B}) &= \mathbf{f_b}\\
\nabla\cdot\mathbf{B} &= 0\\
\frac{\partial \vartheta}{\partial t} + (\mathbf{u}\cdot\nabla)\,\vartheta - \frac{1}{Pr\,Re}\Delta\vartheta - \frac{Ha^2\,Ec}{Re\,Rm^2}\,\|\nabla\times\mathbf{B}\|^2 - \Phi(\mathbf{u}) &= Q.
\end{aligned} \tag{3.5.13}$$

The asterisks in the variables have been removed in order to simplify the expressions. Systems (3.5.12) and (3.5.13) present several non-dimensional parameters. These are defined next together with some others non-dimensional parameters that although are not used in (3.5.12) and (3.5.13) will be used in this research :

1. **Reynolds Number** Re.
   This non dimensional parameter is the ratio of inertial forces to viscous forces. The transition between laminar and turbulent flow is determined by the Reynolds number. The Reynolds number is given by:

$$Re = \frac{U_0\,L_0}{\nu} \tag{3.5.14}$$

2. **Magnetic Reynolds Number** Rm.
   The Magnetic Reynolds number is indicative of the relation between advection and diffusion of the magnetic field. When R_m is large diffusion is weak and the magnetic field lines behave as elastic bands attached to the fluid. This behavior gives origin to the so called *Alfvén waves*. On the other hand, if Rm is small, $\mathbf{u}$ has little influence on $\mathbf{B}$ and the induced magnetic field is negligible by comparison with the imposed magnetic field. In this last case the phenomenon is dissipative rather than elastic because the kinetic energy is converted in heat via Joule dissipation.

   Using the Magnetic Reynolds number it is possible to understand how the parameters μ_m,σ, U_0 and L_0 influence the outcome of MHD phenomena.

When $R_m \to 0$ the imposed magnetic field remains unperturbed. This is the case when μ_m,σ, U_0 and L_0 are all in the range of liquid metals. On the other hand when $R_m \to \infty$ the imposed and the induced magnetic field are of the same order. This last situation is often associated with astrophysical MHD because in those cases L_0 is quite large. All simulations performed in the development of this work have small R_m, because although liquid metals have an electric conductivity around $10^6\,\Omega^{-1}m^{-1}$, the velocities involved are around 1 m/s and therefore they are small. It is important to mention that although R_m in industrial phenomenon is small and the induced magnetic field is negligible, this magnetic field is strong enough to influence the fluid flow. The magnetic Reynolds number is:

$$Rm = \mu_m \sigma U_0\, L_0 \tag{3.5.15}$$

3. **Hartmann Number** Ha.
The Hartmann number represents the ratio of the Lorentz force to the viscous forces. This dimensionless number is important because it gives an indication of the influence of the magnetic field over the boundary layers developed in the flow. This parameter will be discussed further in section 3.6. It is given by:

$$Ha = B_0 L_0 \sqrt{\frac{\sigma}{\rho\nu}} \tag{3.5.16}$$

4. **Coupling Parameter** S.
This dimensionless number represents the ratio between magnetic forces and inertial forces. Sometimes the interaction parameter is called the magnetic force coefficient. When it is small the magnetic field barely affects the flow field. On the other hand if this parameter is greater than 1 the magnetic field affects the flow field extremely. The coupling parameter is:

$$S = \frac{B_0^2}{\mu_m \rho_r\, U_0^2} \tag{3.5.17}$$

5. **Grashof Number** Gr.
The Grashof number is the ratio between the buoyancy force and the viscous force. When buoyancy is the only driving force of the fluid the velocity is completely determined by the quantities in the Grashof number, given by:

$$Gr = \frac{g\hat{\beta}\Delta\vartheta L_0^3}{\nu^2} \tag{3.5.18}$$

6. **Prandtl Number** Pr.
The Prandtl number is function of the properties of the fluid. It is the ratio of momentum diffusivity and thermal diffusivity. When Pr is small it means that the heat diffuses very quickly compared to the velocity. This means

that the thickness of the boundary layer is bigger than the velocity boundary layer. The Prandtl number is very low in liquid metals, usually around 0.01. It is given by:

$$Pr = \frac{\nu}{\alpha} = \frac{c_p \mu}{k_t} \tag{3.5.19}$$

7. **Eckert Number** *Ec*.
   The Eckert number only affects the temperature field and only has to be taken into account when friction gives rise to a noticeable warming of the fluid. It is the ratio of the kinetic energy to the internal energy in the boundary layer of the fluid:

$$Ec = \frac{U_0^2}{c_p \, \Delta\vartheta} \tag{3.5.20}$$

These non-dimensional parameters provide information regarding the nature of the flow in different circumstances and also give some insight about the behavior of the phenomena under study.

3.6 Hartmann Flow

The Hartmann flow is to MHD what the Poiseuille flow is to classical fluid mechanics. The Hartmann flow consists in a flow of a conducting fluid between two parallel plates under the influence of an externally imposed magnetic field.These parallel plates can be electric conductors or insulators. The general situation of this flow is depicted in figure 3.6

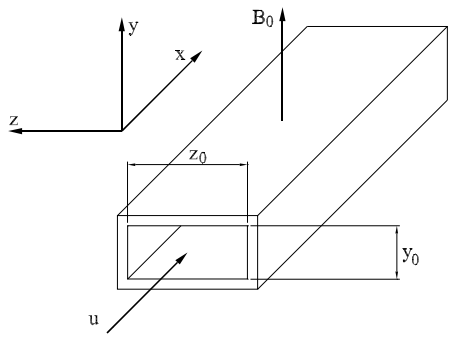

Figure 3.6 *Schematic view of the Hartmann Flow*

In order to solve this flow some assumptions must be made. First it is assumed that the width of the duct is infinite, this means that $z_0 >> y_0$. It is also assumed that the length of the duct is long enough to allow the velocity to be unidimensional. It is assumed that the velocity and the magnetic field have the

form $\mathbf{u} = (u_x(y), 0, 0)$ and $\mathbf{B} = (b_x(y), 1, 0)$. Finally the pressure is assumed to be given by:

$$p(x, y) = -Gx - \frac{Sb^2(y)}{2} + P_0$$

where G is the pressure gradient in x. After substituting the expressions for $\mathbf{u}$, $\mathbf{B}$ and $p(x, y)$ into the stationary MHD equations (3.5.12), the following system of equations is found:

$$\begin{aligned} \frac{\partial^2 u_x(y)}{\partial y^2} + Re\, S \frac{\partial b_x(y)}{\partial y} &= -G\, Re \\ \frac{\partial^2 b_x(y)}{\partial y^2} + Rm \frac{\partial u_x(y)}{\partial y} &= 0 \end{aligned} \tag{3.6.1}$$

System (3.6.1) needs to be complemented by the following boundary condition for insulating walls:

$$\mathbf{B} \times \widehat{\mathbf{n}} = \mathbf{B^d} \times \widehat{\mathbf{n}} \tag{3.6.2}$$

and a boundary condition for conducting walls which is:

$$\mathbf{B} \cdot \widehat{\mathbf{n}} = \mathbf{B^d} \cdot \widehat{\mathbf{n}} \tag{3.6.3}$$

where $\mathbf{B^d} = (0, 1)$. The solutions for system (3.6.1) are:

$$u_x(y) = \frac{G\, Re}{Ha\, \tanh(Ha)} \left(1 - \frac{\cosh(y\, Ha)}{\cosh(Ha)}\right) \tag{3.6.4}$$

$$b_x(y) = \frac{G}{S} \left(\frac{\sinh(y\, Ha)}{\sinh(Ha)} - y\right) \tag{3.6.5}$$

for insulating wall. In the case of conducting walls the solutions are:

$$u_x(y) = \frac{G\, Re}{Ha^2} \left(1 - \frac{\cosh(y\, Ha)}{\cosh(Ha)}\right) \tag{3.6.6}$$

and

$$b_x(y) = \frac{G}{S} \left(\frac{\sinh(y\, Ha)}{Ha\, \cosh(Ha)} - y\right) \tag{3.6.7}$$

The solution (3.6.4) provides an interpretation of Hartmann number Ha. If $Ha \to 0$ the parabolic velocity profile of the Poiseuille flow is recovered. If $Ha \to \infty$ the flow consists in two Hartmann layers on both walls and in the center a core of uniform flow. All the vorticity is pushed to the walls. This situation can be seen in the figure 3.7, where the parabolic profile is recovered when $Ha \to 0$ and a flat profile is formed when $Ha \to \infty$.

The behavior of the magnetic field is presented in figure 3.8. In that figure it can be seen that when $Ha = 0$ the induced magnetic field is null and when Ha grows the induced magnetic field is less intense. This is because less induced magnetic field is needed to overcome the viscous forces.

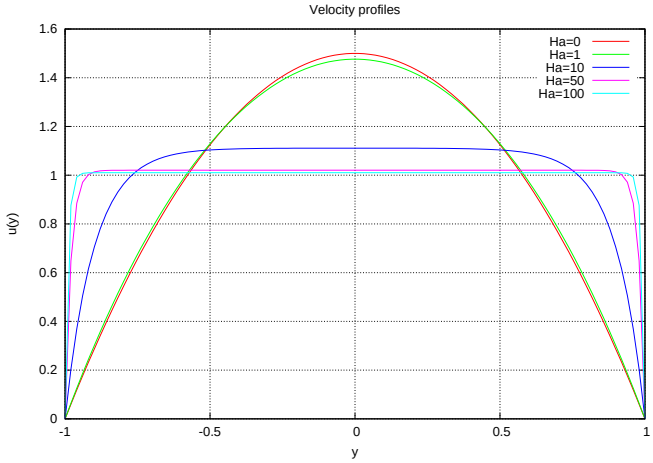

Figure 3.7 *Velocity Profiles for the Hartmann Flow*

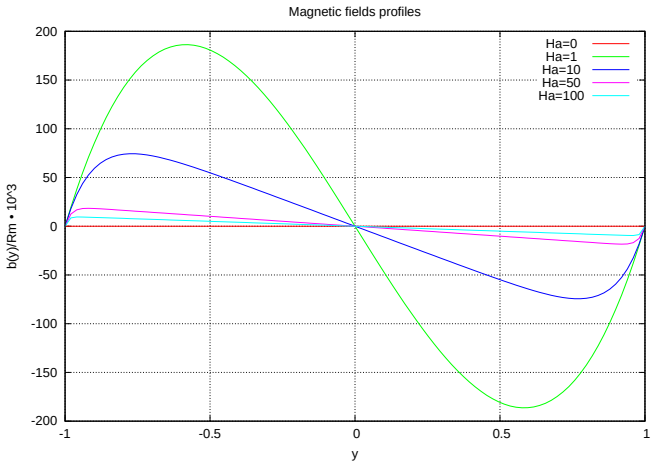

Figure 3.8 *Magnetic Field Profiles for the Hartmann Flow*

Chapter 4

Numerical Schemes

4.1 Introduction

This chapter presents the development of the numerical scheme for the magnetohydrodynamics equations. First the initial and boundary value problem is presented together with its weak form. The time discretization is reviewed after the weak form of the MHD problem is presented. The linealization scheme and the block–iterative coupling are issues also discussed. The stabilized formulation of finite elements for the linear problem is presented. Finally the complete numerical scheme is discussed and analyzed.

4.2 Problem Statement

This section is devoted to the development of the initial boundary value problem and its weak form. For the sake of brevity the development to arrive from the initial boundary value problem to its weak form is omitted and only the final result is reviewed. The initial boundary value problem, also known as strong problem, is the system of governing equations for the phenomena under studied, and in the case of MHD phenomena the system of governing equations is (3.5.11). System (3.5.11) is submitted to a very well known process in order to arrive to a weak or variational problem. The weak or variational problem can be conceived as a relaxed version of the initial boundary value problem because the weak problem demands less smoothness of the solutions. Although the weak problem demands less smoothness of the solutions, it contains all the information found in the initial boundary value problem. The process employed in order to arrive to the variational problem consists in first multiply the governing equations by appropriate weight functions and then integrating over the physical domain. After these steps, the weak form of the original problem is obtained integrating by parts using the *Green–Gauss Theorem*.

4.2.1 Initial and boundary value problem

The strong problem of MHD equations is: Find $(\mathbf{u}, p, \mathbf{B}, r, \vartheta)$ such that $\forall \mathbf{x} \in \Omega \subset \Re^n$, where $n = 2, 3$; the following system of equations holds:

$$\begin{aligned}
\partial_t \mathbf{u} + (\mathbf{u} \cdot \nabla)\mathbf{u} - \nu \Delta \mathbf{u} + \frac{1}{\rho_r} \nabla p - \frac{1}{\mu_m \rho_r} (\nabla \times \mathbf{B}) \times \mathbf{B} + \mathbf{g} \beta \vartheta &= \mathbf{f_u} + \mathbf{g} \left[1 + \beta \vartheta_r\right] \\
\nabla \cdot \mathbf{u} &= 0 \\
\partial_t \mathbf{B} + \frac{1}{\mu_m \sigma} \nabla \times (\nabla \times \mathbf{B}) - \nabla \times (\mathbf{u} \times \mathbf{B}) + \nabla r &= \mathbf{f_b} \\
\nabla \cdot \mathbf{B} &= 0 \\
\partial_t \vartheta + (\mathbf{u} \cdot \nabla)\vartheta - \frac{k_t}{\rho_r c_p} \Delta \vartheta - \frac{1}{\rho_r c_p \mu_m^2 \sigma} \left|\nabla \times \mathbf{B}\right|^2 - \frac{2\mu}{\rho_r c_p} \left|\nabla^S \mathbf{u}\right|^2 &= Q
\end{aligned} \tag{4.2.1}$$

where:

$\mathbf{u}$	is the velocity of the fluid
p	is the pressure of the fluid
$\mathbf{B}$	is the magnetic flux density
r	is the fictitious magnetic pressure
ϑ	is the temperature
$\mathbf{f_u}$	is the vector force for the momentum equation
$\mathbf{f_b}$	is the vector force for the magnetic induction equation
ν	is the kinematic viscosity
ρ_r	is the reference density
μ_m	is the magnetic permeability
$\mathbf{g}$	is the acceleration of the gravity
β	is the thermal expansion coefficient
σ	is the conductivity
k_t	is the heat conductivity
c_p	is the specific heat at constant pressure

In order to obtain the solution of system (4.2.1), the following boundary conditions must be satisfied:

$$\begin{aligned}
&\text{On} \quad \Gamma_{E,\mathbf{u}} : \mathbf{u} = \mathbf{0} \\
&\text{On} \quad \Gamma_{N,\mathbf{u}} : \mathbf{n} \cdot \boldsymbol{\sigma} = \bar{\boldsymbol{t}} \\
&\text{On} \quad \Gamma_{E,\mathbf{B}} : \mathbf{n} \times \mathbf{B} = \mathbf{0},\ r = 0 \\
&\text{On} \quad \Gamma_{N,\mathbf{B}} : \mathbf{n} \cdot \mathbf{B} = \bar{B},\ \mathbf{n} \times (\nabla \times \mathbf{B}) = \bar{\mathbf{J}} \\
&\text{On} \quad \Gamma_{E,\vartheta} : \vartheta = \bar{\vartheta} \\
&\text{On} \quad \Gamma_{N,\vartheta} : \frac{k_t}{\rho_r c_p} \mathbf{n} \cdot \nabla \vartheta = \bar{q}
\end{aligned} \tag{4.2.2}$$

together with the previous boundary conditions the following initial conditions must be satisfied:

$$\begin{aligned} \mathbf{u} &= \mathbf{u_0} \quad \text{at} \quad t = 0 \\ \mathbf{B} &= \mathbf{B_0} \quad \text{at} \quad t = 0 \\ \vartheta &= \vartheta_0 \quad \text{at} \quad t = 0 \end{aligned} \tag{4.2.3}$$

System (4.2.1) together with boundary conditions (4.2.2) and initial conditions (4.2.3) is the strong form of the MHD problem and it will be transformed into a weak or variational form. At this point it is convenient to clarify the use of r in system (4.2.1). r is a fictitious magnetic pressure used to enforce the divergence free condition for $\mathbf{B}$, (3.3.4). Its use was proposed by Jiang, Wu and Povinelli [34], and it is employed to prevent the onset of spurious solutions in the magnetic field.

It is worthy of mention the fact that the force term $\mathbf{f_b}$, introduced for generality purposes, has to be divergence free. In a similar way, the initial magnetic field $\mathbf{B_0}$ must be also solenoidal. If we take divergence of magnetic advection equation in (4.2.1) and use the essential boundary condition on the magnetic field $\mathbf{n} \times \mathbf{B} = \mathbf{0}$ it turns out that $r = 0$. Nevertheless, the introduction of r will be useful to enforce zero divergence condition over the magnetic field, while keeping the correct functional setting of the problem.

4.2.2 Weak form

As was said previously, in order to obtain the variational form of the original problem, first (4.2.1) must be multiplied by an appropriate weight function. If the unknowns of the original problem are $(\mathbf{u}, p, \mathbf{B}, r, \vartheta)$ then the proposed weight functions are $(\mathbf{v}, q, \mathbf{C}, s, \psi)$. After multiplying the strong form by the weight functions, integrating over the domain Ω and applying the *Green– Gauss Theorem*, the weak form is obtained:

For each $t \in (0, \infty)$, find $(\mathbf{u}, p, \mathbf{B}, r, \vartheta) \in (\mathbb{V}_u \times \mathbb{V}_p \times \mathbb{V}_B \times \mathbb{V}_r \times \mathbb{V}_\vartheta)$ such that:

$$\begin{aligned} (\partial_t \mathbf{u}, \mathbf{v}) + A_{uu}(\mathbf{u}, \mathbf{u}, \mathbf{v}) + A_{uB}(\mathbf{B}, \mathbf{B}, \mathbf{v}) + A_{u\vartheta}(\vartheta, \mathbf{v}) - b_u(p, \mathbf{v}) &= L_u(\mathbf{v}) \\ b_u(q, \mathbf{u}) &= 0 \\ (\partial_t \mathbf{B}, \mathbf{C}) + A_{Bu}(\mathbf{u}, \mathbf{B}, \mathbf{C}) + A_{BB}(\mathbf{B}, \mathbf{C}) + b_B(r, \mathbf{C}) &= L_{B1}(\mathbf{C}) \\ b_B(s, \mathbf{B}) &= L_{B2}(s) \\ (\partial_t \vartheta, \psi) + A_{\vartheta u,1}(\mathbf{u}, \vartheta, \psi) + A_{\vartheta u,2}(\mathbf{u}, \mathbf{u}, \psi) + A_{\vartheta B}(\mathbf{B}, \mathbf{B}, \psi) + A_{\vartheta\vartheta}(\vartheta, \psi) &= L_T(\psi) \end{aligned} \tag{4.2.4}$$

$\forall\ (\mathbf{v}, q, \mathbf{C}, s, \psi) \in (\mathbb{V}_u \times \mathbb{V}_p \times \mathbb{V}_B \times \mathbb{V}_r \times \mathbb{V}_\vartheta)$, where the spaces of functions are defined as:

$$\mathbb{V}_u = \left\{\mathbf{v} \in L^2(0,T;H^1(\Omega)^d))|\mathbf{v} = \mathbf{0} \text{ on } \Gamma_{E,\mathbf{u}}\right\} \tag{4.2.5}$$

$$\mathbb{V}_p = \left\{q \in \mathcal{D}'(0,T;L^2(\Omega))|\int_\Omega q = 0 \text{ if } \Gamma_{N,\mathbf{u}} = \emptyset\right\} \tag{4.2.6}$$

$$\mathbb{V}_B = \left\{\mathbf{C} \in L^2(0,T;H(curl,\Omega))|\mathbf{n}\times\mathbf{C} = \mathbf{0} \text{ on } \Gamma_{E,\mathbf{B}}\right\} \tag{4.2.7}$$

$$\mathbb{V}_r = \left\{s \in \mathcal{D}'(0,T;H^1(\Omega))|s = 0; \text{on } \Gamma_{E,\mathbf{B}} = \emptyset\right\} \tag{4.2.8}$$

$$\mathbb{V}_\vartheta = \left\{\psi \in L^2(0,T;H^1(\Omega))|\psi = 0; \text{on } \Gamma_{E,\vartheta}\right\} \tag{4.2.9}$$

where $\mathbf{L}^2(\Omega)$ is the space of square–integrable functions:

$$\mathbf{L}^2(\Omega) = \left\{u : \int_\Omega |u|^2\, dx < \infty\right\} \tag{4.2.10}$$

Also $H^1(\Omega)$ is the Sobolev space of order 1, the space consisting of those functions u in $\mathbf{L}^2(\Omega)$ together with all their weak partial derivatives $D^\alpha u$. This space is defined as:

$$H^1(\Omega) = \left\{u : D^\alpha u \in L^2(\Omega)\ \forall\ |\alpha| \le 1\right\} \tag{4.2.11}$$

Finally $H(curl,\Omega)$ is defined as:

$$H(curl,\Omega) = \left\{\mathbf{u} : \mathbf{u} \in \mathbf{L}^2(\Omega), \nabla\times\mathbf{u} \in \mathbf{L}^2(\Omega)\right\} \tag{4.2.12}$$

In order to completely understand this variational form, let us remember the definition of the inner product for functions belonging to $\mathbf{L}^2(\Omega)$:

$$(\mathbf{u},\mathbf{v}) = \int_\Omega \mathbf{u}\cdot\mathbf{v} \tag{4.2.13}$$

with this definition it is clear that:

$$(\partial_\mathbf{t}\mathbf{u},\mathbf{v}) = \int_\Omega \partial_\mathbf{t}\mathbf{u}\cdot\mathbf{v} \tag{4.2.14}$$

$$(\partial_\mathbf{t}\mathbf{B},\mathbf{C}) = \int_\Omega \partial_\mathbf{t}\mathbf{B}\cdot\mathbf{C} \tag{4.2.15}$$

$$(\partial_t\vartheta,\psi) = \int_\Omega \partial_t\vartheta\,\psi \tag{4.2.16}$$

Also, several multilinear forms must be defined in order to write down the variational form:

$$A_{uu}(\mathbf{u}_1, \mathbf{u}_2, \mathbf{v}) = \int_\Omega \mathbf{v} \cdot (\mathbf{u}_1 \cdot \nabla)\mathbf{u}_2 + \nu \int_\Omega \nabla \mathbf{v} : \nabla \mathbf{u}_2 \tag{4.2.17}$$

$$A_{uB}(\mathbf{B}_1, \mathbf{B}_2, \mathbf{v}) = -\frac{1}{\mu_m \rho_r} \int_\Omega \mathbf{v} \cdot (\nabla \times \mathbf{B}_1) \times \mathbf{B}_2 \tag{4.2.18}$$

$$A_{u\vartheta}(\vartheta, \mathbf{v}) = \beta \int_\Omega \mathbf{v} \cdot \mathbf{g}\vartheta \tag{4.2.19}$$

$$A_{Bu}(\mathbf{u}, \mathbf{B}, \mathbf{C}) = -\int_\Omega \mathbf{C} \cdot \nabla \times (\mathbf{u} \times \mathbf{B}) \tag{4.2.20}$$

$$A_{BB}(\mathbf{B}, \mathbf{C}) = \frac{1}{\mu_m \sigma} \int_\Omega (\nabla \times \mathbf{C}) \cdot (\nabla \times \mathbf{B}) \tag{4.2.21}$$

$$A_{\vartheta u,1}(\mathbf{u}, \vartheta, \psi) = \int_\Omega \psi \mathbf{u} \cdot \nabla \vartheta \tag{4.2.22}$$

$$A_{\vartheta u,2}(\mathbf{u}_1, \mathbf{u}_2, \psi) = -\frac{2\mu}{\rho_r c_p} \int_\Omega \psi \nabla^S \mathbf{u}_1 : \nabla^S \mathbf{u}_2 \tag{4.2.23}$$

$$A_{\vartheta B}(\mathbf{B}_1, \mathbf{B}_2, \psi) = -\frac{1}{\rho_r c_p \mu_m^2 \sigma} \int_\Omega \psi \, (\nabla \times \mathbf{B}_1) \cdot (\nabla \times \mathbf{B}_2) \tag{4.2.24}$$

$$A_{\vartheta\vartheta}(\vartheta, \psi) = \frac{k_t}{\rho_r c_p} \int_\Omega \nabla \psi \cdot \nabla \vartheta \tag{4.2.25}$$

$$b_u(q, \mathbf{v}) = \frac{1}{\rho_r} \int_\Omega q \nabla \cdot \mathbf{v} \tag{4.2.26}$$

$$b_B(s, \mathbf{C}) = \int_\Omega \nabla s \cdot \mathbf{C} \tag{4.2.27}$$

$$L_u(\mathbf{v}) = \int_\Omega \mathbf{v} \cdot [\mathbf{f}_\mathbf{u} + \mathbf{g}(1 + \beta\vartheta_r)] + \int_{\Gamma_{N,\mathbf{u}}} \mathbf{v} \cdot \bar{\mathbf{t}} \tag{4.2.28}$$

$$L_{B1}(\mathbf{C}) = \int_\Omega \mathbf{C} \cdot \mathbf{f}_\mathbf{b} + \int_{\Gamma_{N,\mathbf{B}}} \mathbf{v} \cdot \bar{\mathbf{J}} \tag{4.2.29}$$

$$L_{B2}(s) = \int_{\Gamma_{N,\mathbf{B}}} s\bar{B} \tag{4.2.30}$$

$$L_\vartheta(\psi) = \int_\Omega \psi \, Q + \int_{\Gamma_{N,\vartheta}} \psi \, \bar{q} \tag{4.2.31}$$

A more compact expression for the weak form of the MHD problem is the following:
Find $\mathbf{U}$ such that:

$$M\left(\partial_t \mathbf{U}, \mathbf{V}\right) + A\left(\mathbf{U}, \mathbf{V}\right) = L\left(\mathbf{V}\right) \tag{4.2.32}$$

$\forall \mathbf{V}$, where $\mathbf{U} = (\mathbf{u}, p, \mathbf{B}, r, \vartheta)^t$ and $\mathbf{V} = (\mathbf{v}, q, \mathbf{C}, s, \psi)^t$.
In this final form of the weak problem $M\left(\mathbf{U}, \mathbf{V}\right)$ is given by:

$$M\left(\mathbf{U}, \mathbf{V}\right) = (\mathbf{u}, \mathbf{v}) + \alpha_B \left\langle \mathbf{B}, \mathbf{C} \right\rangle + \alpha_\vartheta \left\langle \vartheta, \psi \right\rangle \tag{4.2.33}$$

$A(\mathbf{U},\mathbf{V})$ is given by:

$$\begin{aligned} A(\mathbf{U},\mathbf{V}) =& A_{uu}(\mathbf{u},\mathbf{u},\mathbf{v}) + A_{uB}(\mathbf{B},\mathbf{B},\mathbf{v}) + A_{u\vartheta}(\vartheta,\mathbf{v}) - b_u(p,\mathbf{v}) + b_u(q,\mathbf{u}) \\ &+\alpha_B\left[A_{Bu}(\mathbf{u},\mathbf{B},\mathbf{C}) + A_{BB}(\mathbf{B},\mathbf{C}) + b_B(r,\mathbf{C}) - b_B(s,\mathbf{B})\right] \\ &+\alpha_\vartheta\left[A_{\vartheta u,1}(\mathbf{u},\vartheta,\psi) + A_{\vartheta u,2}(\mathbf{u},\mathbf{u},\psi) + A_{\vartheta B}(\mathbf{B},\mathbf{B},\psi) + A_{\vartheta\vartheta}(\vartheta,\psi)\right] \end{aligned} \tag{4.2.34}$$

and $L(\mathbf{V})$ is given by:

$$L(\mathbf{V}) = L_u(\mathbf{v}) + \alpha_B\left[L_{B1}(\mathbf{C}) + L_{B2}(s)\right] + \alpha_\vartheta L_\vartheta(\psi) \tag{4.2.35}$$

where α_B and α_ϑ are scaling factors.

4.3 Time Discretization

Although system (4.2.32) has less strict requirements that (4.2.1), because it demands less smoothness of the solutions, it is still a continuous system both in time and space. Before tackling the spacial discretization it is convenient to deal with the time discretization. First let us divide the time interval $[0,T]$ into N time steps of uniform length δt. It is clear that:

$$\delta t = T/N \tag{4.3.1}$$
$$t^n = n\delta t \tag{4.3.2}$$
$$t^{n+1} = t^n + \delta t \tag{4.3.3}$$

where $n = 0,1,2,3,\ldots,n,\ldots,N$. In every time step $\mathbf{u}^n$, p^n, $\mathbf{B}^n$, r^n, ϑ^n respectively denote approximations of $\mathbf{u}(n\delta t,\mathbf{x})$, $p(n\delta t,\mathbf{x})$, $\mathbf{B}(n\delta t,\mathbf{x})$, $r(n\delta t,\mathbf{x})$, $\vartheta(n\delta t,\mathbf{x})$. The cylindrical nature of $\Omega\times[0,T]$ makes more convenient to use finite differences in time discretization. While discussing time discretization, it is better to reformulate (4.2.32) as:

$$M(\partial_t\mathbf{U},\mathbf{V}) = L(\mathbf{V}) - A(\mathbf{U},\mathbf{V}) = F(\mathbf{U},\mathbf{V}). \tag{4.3.4}$$

Now, in order to present the so called θ–method, let us define the next convex combinations:

$$x^{n+\theta} := \theta x^{n+1} + (1-\theta)x^n \tag{4.3.5}$$
$$t^{n+\theta} := \theta t^{n+1} + (1-\theta)t^n \tag{4.3.6}$$

where $\theta\in[0,1]$. Once the convex combinations are defined, the time derivative can be approximated by a weighted average of x^{n+1} and x^n at the end of the points of integration. For a problem of the form $\frac{dx}{dt} = F(x,t)$, this leads to:

$$\frac{1}{\delta t}\left(x^{n+1}-x^{n}\right)=\theta F\left(x^{n+1},t^{n+1}\right)+(1-\theta)F\left(x^{n},t^{n}\right) \tag{4.3.7}$$

this last equation is the θ–scheme. Different methods are obtained from (4.3.7) with different values of θ. If $\theta < 1/2$ the schemes are conditionally stable and the best known scheme is the *Euler method*. For values of $\theta \geq 1/2$ methods are unconditionally stables. The most common of these methods are *Backward Euler* $\theta = 1$, *Galerkin* $\theta = 2/3$ and *Crank–Nicholson* $\theta = 1/2$. Applying the θ–method to (4.3.4) the next expression is obtained:

$$M\frac{1}{\delta t}\left(\mathbf{U}^{n+1}-\mathbf{U}^{n},\mathbf{V}\right)=F\left(\mathbf{U}^{n+\theta},\mathbf{V}\right) \tag{4.3.8}$$

An equivalent form for this expression is:

$$M\frac{1}{\delta t}\left(\mathbf{U}^{n+1}-\mathbf{U}^{n},\mathbf{V}\right)+A\left(\mathbf{U}^{n+\theta},\mathbf{V}\right)=L\left(\mathbf{V}\right) \tag{4.3.9}$$

4.4 Linealization and Block-Iterative Coupling

Given the nature of the MHD problem, neither the Maxwell equations nor the Navier–Stokes equations can be solved separately and they ought to be solved in the same domain and at the same time. This requirement, of course, presents problems because in order to solve the Navier-Stokes equations it is mandatory to have the magnetic field flux density $\mathbf{B}$, which is obtained solving the Maxwell equations. In turn, in order to solve the Maxwell equations the velocity $\mathbf{u}$ is required. This situation make necessary to linearize and decouple the Maxwell equations and the Navier–Stokes equations.

4.4.1 Linearization of the stationary MHD problem

For the sake of simplicity, let us consider in this analysis problem (3.5.6), which is reproduced next:

$$\begin{aligned}(\mathbf{u}\cdot\nabla)\mathbf{u}-\nu\Delta\mathbf{u}+\frac{1}{\rho_r}\nabla p-\frac{1}{\mu_m\rho_r}(\nabla\times\mathbf{B})\times\mathbf{B}&=\mathbf{f_u}\\ \nabla\cdot\mathbf{u}&=0\\ \frac{1}{\mu_m\sigma}\nabla\times(\nabla\times\mathbf{B})-\nabla\times(\mathbf{u}\times\mathbf{B})+\nabla r&=\mathbf{f_b}\\ \nabla\cdot\mathbf{B}&=0\end{aligned}$$

Boundary conditions are not included to simplify the presentation. Grouping the unknowns and the weight functions in $\mathbf{U}=(\mathbf{u},p,\mathbf{B},r)^t$ and $\mathbf{V}=(\mathbf{v},q,\mathbf{C},s)^t$ respectively, the variational problem can be stated as:

$$A\left(\mathbf{U},\mathbf{V}\right)=L\left(\mathbf{U},\mathbf{V}\right) \tag{4.4.1}$$

where:

$$\begin{aligned} A\left(\mathbf{U},\mathbf{V}\right) = \quad & A_{uu}\left(\mathbf{u},\mathbf{u},\mathbf{v}\right) + A_{uB}\left(\mathbf{B},\mathbf{B},\mathbf{v}\right) - b_u\left(p,\mathbf{v}\right) + b_u\left(q,\mathbf{u}\right) \\ & + \alpha_B\left[A_{Bu}\left(\mathbf{u},\mathbf{B},\mathbf{C}\right) + A_{BB}\left(\mathbf{B},\mathbf{C}\right) + b_B\left(r,\mathbf{C}\right) - b_B\left(s,\mathbf{B}\right)\right] \end{aligned} \tag{4.4.2}$$

Taking the scaling coefficient as $\alpha_B = 1/(\mu_m \rho_r)$ we have:

$$\begin{aligned} A\left(\mathbf{U},\mathbf{V}\right) = & \int_\Omega \mathbf{v}\cdot\left(\mathbf{u}\cdot\nabla\right)\mathbf{u} + \nu\int_\Omega \nabla\mathbf{v} : \nabla\mathbf{u} - \frac{1}{\mu_m\rho_r}\int_\Omega \mathbf{v}\cdot\left(\nabla\times\mathbf{B}\right)\times\mathbf{B} \\ & - \frac{1}{\rho_r}\int_\Omega p\nabla\cdot\mathbf{v} + \frac{1}{\rho_r}\int_\Omega q\nabla\cdot\mathbf{u} \\ & - \frac{1}{\mu_m\rho_r}\int_\Omega \mathbf{C}\cdot\nabla\times\left(\mathbf{u}\times\mathbf{B}\right) + \frac{1}{\mu_m\rho_r}\frac{1}{\mu_m\sigma}\int_\Omega \left(\nabla\times\mathbf{C}\right)\cdot\left(\nabla\times\mathbf{B}\right) \\ & + \frac{1}{\mu_m\rho_r}\int_\Omega \nabla r\cdot\mathbf{C} - \frac{1}{\mu_m\rho_r}\int_\Omega \nabla s\cdot\mathbf{B} \end{aligned} \tag{4.4.3}$$

The simplest way to linearize this problem is by a fixed point treatment of the quadratic terms. In order to do that let us assume that the velocity and the magnetic field are known at iteration k, $\mathbf{u}^k$ and $\mathbf{B}^k$, respectively, and we have to compute these fields at iteration $k+1$. If $e_i(k) = k$ or $e_i(k) = k+1$ and $e_i'(k) = 2k+1-e_i(k)$, the approximation of $A\left(\mathbf{U},\mathbf{V}\right)$ at iteration $k+1$, using the fixed point method can be written as:

$$\begin{aligned} A^{k+1}\left(\mathbf{U},\mathbf{V}\right) = & \int_\Omega \mathbf{v}\cdot\left(\mathbf{u}^{e_1(k)}\cdot\nabla\right)\mathbf{u}^{e_1'(k)} + \nu\int_\Omega \nabla\mathbf{v} : \nabla\mathbf{u}^{k+1} \\ & - \frac{1}{\mu_m\rho_r}\int_\Omega \mathbf{v}\cdot\left(\nabla\times\mathbf{B}^{e_2(k)}\right)\times\mathbf{B}^{e_2'(k)} \\ & - \frac{1}{\rho_r}\int_\Omega p^{k+1}\nabla\cdot\mathbf{v} + \frac{1}{\rho_r}\int_\Omega q\nabla\cdot\mathbf{u}^{k+1} \\ & - \frac{1}{\mu_m\rho_r}\int_\Omega \mathbf{C}\cdot\nabla\times\left(\mathbf{u}^{e_3(k)}\times\mathbf{B}^{e_3'(k)}\right) \\ & + \frac{1}{\mu_m\rho_r}\frac{1}{\mu_m\sigma}\int_\Omega \left(\nabla\times\mathbf{C}\right)\cdot\left(\nabla\times\mathbf{B}^{k+1}\right) \\ & + \frac{1}{\mu_m\rho_r}\int_\Omega \nabla r^{k+1}\cdot\mathbf{C} - \frac{1}{\mu_m\rho_r}\int_\Omega \nabla s\cdot\mathbf{B}^{k+1} \end{aligned} \tag{4.4.4}$$

In order to have a stable problem at each iteration, we should guarantee that $A^{k+1}\left(\mathbf{U}^{k+1},\mathbf{V}^{k+1}\right) \geq 0$, which leads to conditions:

$$\int_\Omega \mathbf{u}^{k+1}\cdot\left(\mathbf{u}^{e_1(k)}\cdot\nabla\right)\mathbf{u}^{e_1'(k)} \geq 0 \tag{4.4.5}$$

$$\int_\Omega \left[-\mathbf{u}^{k+1}\cdot\left(\nabla\times\mathbf{B}^{e_2(k)}\right)\times\mathbf{B}^{e_2'(k)} - \mathbf{B}^{k+1}\cdot\nabla\times\left(\mathbf{u}^{e_3(k)}\times\mathbf{B}^{e_3'(k)}\right)\right] \geq 0 \tag{4.4.6}$$

When $\nabla \cdot \mathbf{u}^k = 0, \nabla \cdot \mathbf{B}^k = 0$, these conditions hold only if $e_1(k) = k$ (as it is well known), $e_2(k) = k$ and $e_3(k) = k+1$. Therefore, calling $\mathbf{a} \equiv \mathbf{u}^k$, $\mathbf{u} \equiv \mathbf{u}^{k+1}$, $\mathbf{b} \equiv \mathbf{B}^k$, $\mathbf{B} \equiv \mathbf{B}^{k+1}$, the only fixed point linearization of the problem that is stable is:

$$\begin{aligned} (\mathbf{a}\cdot\nabla)\mathbf{u} - \nu\Delta\mathbf{u} + \frac{1}{\rho_r}\nabla p - \frac{1}{\mu_m\rho_r}(\nabla\times\mathbf{B})\times\mathbf{b} &= \mathbf{f_u} \\ \nabla\cdot\mathbf{u} &= 0 \\ \frac{1}{\mu_m\sigma}\nabla\times(\nabla\times\mathbf{B}) - \nabla\times(\mathbf{u}\times\mathbf{b}) + \nabla r &= \mathbf{f_b} \\ \nabla\cdot\mathbf{B} &= 0 \end{aligned} \tag{4.4.7}$$

System (4.4.7) is the problem for which the stabilized finite element scheme will be built.

4.4.2 Full coupling and block–iterative coupling

Let us consider again the stationary problem, but now accounting also for the thermal coupling. Once the approach to deal with the nonlinearity has been determinated, the thermal coupling is easy to treat, since the temperature term in the momentum equation is linear. It may be considered either a full coupling or a block iterative coupling. Both options can be written in a single format as follows. If $e(k) = k$ or $e(k) = k+1$ and $e_i'(k) = 2k+1-e_i(k)$, the fully linearized and coupled problem is introduced:

$$\begin{aligned} A_{uu}(\mathbf{u}^k, \mathbf{u}^{k+1}, \mathbf{v}) + A_{uB}(\mathbf{B}^{k+1}, \mathbf{B}^k, \mathbf{v}) + A_{u\vartheta}(\vartheta^{e(k)}, \mathbf{v}) - b_u(p^{k+1}, \mathbf{v}) &= L_u(\mathbf{v}) \\ b_u\left(q, \mathbf{u}^{k+1}\right) &= 0 \\ A_{Bu}\left(\mathbf{u}^{k+1}, \mathbf{B}^k, \mathbf{C}\right) + A_{BB}\left(\mathbf{B}^{k+1}, \mathbf{C}\right) + b_B\left(r^{k+1}, \mathbf{C}\right) &= L_{B1}(\mathbf{C}) \\ b_B\left(s, \mathbf{B}^{k+1}\right) &= L_{B2}(s) \\ A_{\vartheta u,1}\left(\mathbf{u}^{e'(k)}, \vartheta^{k+1}, \psi\right) + A_{\vartheta\vartheta}(\vartheta^{k+1}, \psi) &= L_T^k(\psi) \end{aligned} \tag{4.4.8}$$

where

$$L_k^T(\psi) = L_T(\psi) - A_{\vartheta u,2}\left(\mathbf{u}^{e'(k)}, \mathbf{u}^{e'(k)}, \psi\right) - A_{\vartheta B}\left(\mathbf{B}^{e'(k)}, \mathbf{B}^{e'(k)}, \psi\right). \tag{4.4.9}$$

It is clear that when $e(k) = k+1$ and thus $e'(k) = k$, the problem needs to be solved for $\mathbf{u}^{k+1}$, p^{n+1}, $\mathbf{B}^{k+1}$, s^{k+1} and ϑ^{k+1} in a coupled way. The production of heat given by $A_{\vartheta u,2}\left(\mathbf{u}^{e'(k)}, \mathbf{u}^{e'(k)}, \psi\right)$ and $A_{\vartheta B}\left(\mathbf{B}^{e'(k)}, \mathbf{B}^{e'(k)}, \psi\right)$ needs to be evaluated at the previous iteration (unless a Newton-Raphson-type strategy is used). On the other hand, when $e(k) = k$ the problem can be solved first for $\mathbf{u}^{k+1}$, p^{n+1},

$\mathbf{B}^{k+1}$ and r^{k+1}. Once these variables are computed, temperature may be updated by solving the last equation of (4.4.8). In this case it is possible to use the variables $\mathbf{u}^{k+1}$ and $\mathbf{B}^{k+1}$ just computed, thus leading to a Gauss–Seidel–type coupling. Of course, a Jacobi coupling, in which L_T^k in (4.4.9) is evaluated with $\mathbf{u}^k$ and $\mathbf{B}^k$ is also possible. However, the computational effort is the same and convergence is known to be faster for Gauss–Seidel–type coupling. The interested reader is referred to the work of Cervera, Codina and Galindo [9] for a further discussion over this subject.

4.4.3 Time discrete and linearized scheme

The next step is to consider the time discrete problem using the generalized trapezoidal rule together with the linearization scheme described in the previous subsection (4.4.2). These leads to the following problem: For $n = 0, 1, 2, \ldots$ given $\mathbf{u}^n$,p^n,$\mathbf{B}^n$,r^n and ϑ^n, find $\mathbf{u}^{n+1}$,p^{n+1},$\mathbf{B}^{n+1}$,$r^{n+1}$and ϑ^{n+1} as the converged solutions of the following iterative algorithm:

$$
\begin{aligned}
(\delta_t \mathbf{u}^{n,k+1}, \mathbf{v}) + A_{uu}(\mathbf{u}^{n+\theta,k}, \mathbf{u}^{n+\theta,k+1}, \mathbf{v}) + A_{uB}(\mathbf{B}^{n+\theta,k+1}, \mathbf{B}^{n+\theta,k}, \mathbf{v}) & \\
+A_{u\vartheta}(\vartheta^{n+\theta,e(k)}, \mathbf{v}) - b_u(p^{n+1,k+1}, \mathbf{v}) &= L_u^{n+\theta}(\mathbf{v}) \\
b_u(q, \mathbf{u}^{n+1,k+1}) &= 0 \\
(\delta_t \mathbf{B}^{n,k+1}, \mathbf{C}) + A_{Bu}(\mathbf{u}^{n+\theta,k+1}, \mathbf{B}^{n+\theta,k}, \mathbf{C}) + A_{BB}(\mathbf{B}^{n+\theta,k+1}, \mathbf{C}) & \\
+b_B(r^{n+1,k+1}, \mathbf{C}) &= L_{B1}^{n+\theta}(\mathbf{C}) \\
b_B(s, \mathbf{B}^{n+1,k+1}) &= L_{B2}^{n+\theta}(s) \\
(\delta_t \vartheta^{n,k+1}, \psi) + A_{\vartheta u,1}(\mathbf{u}^{n+\theta,e'(k)}, \vartheta^{n+\theta,k+1}, \psi) + A_{\vartheta\vartheta}(\vartheta^{n+\theta,k+1}, \psi) &= L_T^{n+\theta,k}(\psi)
\end{aligned}
\tag{4.4.10}
$$

with the definition:

$$
\begin{aligned}
L_T^{n+\theta,k}(\psi) = L_T^{n+\theta}(\psi) - A_{\vartheta u,2}(\mathbf{u}^{n+\theta,e'(k)}, \mathbf{u}^{n+\theta,e'(k)}, \psi) - & \\
A_{\vartheta B}(\mathbf{B}^{n+\theta,e'(k)}, \mathbf{B}^{n+\theta,e'(k)}, \psi). &
\end{aligned}
\tag{4.4.11}
$$

For implementation purposes, it is very convenient to write the problem to be solved as a time–discrete system of linear convection–diffusion–reaction equations (CDR equations). Let us consider the case $e(k) = k+1$ in (4.4.8), the case $e(k) = k$ being similar, and let us call $\mathbf{a} \equiv \mathbf{u}^{n+\theta,k}$, $\mathbf{u} \equiv \mathbf{u}^{n+\theta,k+1}$, $\mathbf{b} \equiv \mathbf{B}^{n+\theta,k}$, $\mathbf{B} \equiv \mathbf{B}^{n+\theta,k+1}$. The differential equations associated to system (4.4.10) are:

$$\begin{aligned}
\delta_t \mathbf{u} + (\mathbf{a}\cdot\nabla)\mathbf{u} - \nu\Delta\mathbf{u} + \frac{1}{\rho_r}\nabla p - \frac{1}{\mu_m\rho_r}(\nabla\times\mathbf{B})\times\mathbf{b} + \mathbf{g}\beta\vartheta &= \mathbf{f}_u \\
\nabla\cdot\mathbf{u} &= 0 \\
\delta_t \mathbf{B} + \frac{1}{\mu_m\sigma}\nabla\times(\nabla\times\mathbf{B}) - \nabla\times(\mathbf{u}\times\mathbf{b}) + \nabla r &= \mathbf{f}_b \\
\nabla\cdot\mathbf{B} &= 0 \\
\delta_t\vartheta + (\mathbf{a}\cdot\nabla)\vartheta - \frac{k_t}{\rho_r c_p}\Delta\vartheta &= Q_{tot}
\end{aligned} \tag{4.4.12}$$

where:

$$Q_{tot} = Q - \frac{1}{\rho_r c_p \mu_m^2 \sigma}\left|\nabla\times\mathbf{b}\right|^2 - \frac{2\mu_m}{\rho_r c_p}\left|\nabla^S\mathbf{a}\right|^2. \tag{4.4.13}$$

The problem considered can be written as the vector differential equation:

$$\mathbf{M}\delta_t\mathbf{U} + \mathcal{L}(\mathbf{U}) = \mathbf{F} \quad \text{in} \quad \Omega \tag{4.4.14}$$

where $\mathbf{M}$ is defined as $\mathbf{M} = \mathrm{diag}(\mathbf{I}, 0, \alpha_B\mathbf{I}, 0, \alpha_\vartheta)$, $\mathbf{I}$ being the $d\times d$ identity, and $\delta_t\mathbf{U} = (\delta t)^{-1}(\mathbf{U} - \mathbf{U}^n)$, with $\mathbf{U}^n$ known, $\mathbf{F} = [\mathbf{f}_u, 0, \mathbf{f}_b, 0, Q_{tot}]^t$ is a known vector of $n_{unk} = 2d+3$ components and the operator $\mathcal{L}$ is given by:

$$\mathcal{L}(\mathbf{U}) = \begin{bmatrix}
(\mathbf{a}\cdot\nabla)\mathbf{u} - \nu\Delta\mathbf{u} + \frac{1}{\rho_r}\nabla p - \frac{1}{\mu_m\rho_r}(\nabla\times\mathbf{B})\times\mathbf{b} + \mathbf{g}\beta\vartheta \\
\nabla\cdot\mathbf{u} \\
\frac{1}{\mu_m\sigma}\nabla\times(\nabla\times\mathbf{B}) - \nabla\times(\mathbf{u}\times\mathbf{b}) + \nabla r \\
\nabla\cdot\mathbf{B} \\
(\mathbf{a}\cdot\nabla)\vartheta - \frac{k_t}{\rho_r c_p}\Delta\vartheta
\end{bmatrix} \tag{4.4.15}$$

This is an operator of the form:

$$\mathcal{L}(\mathbf{U}) := \mathbf{A}_i\frac{\partial\mathbf{U}}{\partial x_i} - \frac{\partial}{\partial x_i}\left(\mathbf{K}_{ij}\frac{\partial\mathbf{U}}{\partial x_j}\right) + \mathbf{S}\mathbf{U}, \tag{4.4.16}$$

where $\mathbf{A}_i$, $\mathbf{K}_{ij}$ and $\mathbf{S}$ are $n_{unk}\times n_{unk}$ matrices $(i,j = 1,\dots d)$. $\mathbf{A}_i$ are the convective matrices, $\mathbf{K}_{ij}$ are the diffusive matrices and $\mathbf{S}$ is the reaction matrix. Let matrices $\mathbf{A}_i$ be split as $\mathbf{A}_i = \mathbf{A}_i^c + \mathbf{A}_i^f$, where $\mathbf{A}_i^c$ is the part of the convection matrices which is *not* integrated by parts and $\mathbf{A}_i^f$ is the part that *is* integrated by parts. In our case, matrices $\mathbf{A}_i^f$ come from the first order derivatives of the hydrodynamic pressure p. It would be also possible to integrate by parts the first order derivatives corresponding to the terms $(\mathbf{u}\cdot\nabla)\mathbf{u}$ and $\nabla\times(\mathbf{u}\times\mathbf{B})$. The weak form of the problem supplied with the appropriate homogeneous boundary conditions can be written again as the time discrete and linearized counterpart of (4.2.34):

$$\mathbf{M}(\delta_t\mathbf{U}, \mathbf{V}) + A^{lin}(\mathbf{U}, \mathbf{V}) = L(\mathbf{V}) \tag{4.4.17}$$

where:

$$\begin{aligned} A^{lin}(\mathbf{U},\mathbf{V}) &:= \int_\Omega \mathbf{V}^t \mathbf{A}_i^c \frac{\partial \mathbf{U}}{\partial x_i} - \int_\Omega \frac{\partial}{\partial x_i}\left(\mathbf{V}^t \mathbf{A}_i^f\right)\mathbf{U} + \int_\Omega \frac{\partial \mathbf{V}^t}{\partial x_i}\mathbf{K}_{ij}\frac{\partial \mathbf{U}}{\partial x_i} \\ L(\mathbf{V}) &:= \int_\Omega \mathbf{V}^t \mathbf{F}. \end{aligned} \tag{4.4.18}$$

For the particular case of the MHD problem:

$$\begin{aligned} A^{lin}(\mathbf{U},\mathbf{V}) = &\int_\Omega \mathbf{v}\cdot(\mathbf{a}\cdot\nabla)\,\mathbf{u} + \nu\int_\Omega \nabla\mathbf{v} : \nabla\mathbf{u} - \frac{1}{\mu_m\rho_r}\int_\Omega \mathbf{v}\cdot(\nabla\times\mathbf{B})\times\mathbf{b} \\ &- \frac{1}{\rho_r}\int_\Omega p\nabla\cdot\mathbf{v} + \frac{1}{\rho_r}\int_\Omega q\nabla\cdot\mathbf{u} \\ &- \frac{1}{\mu_m\rho_r}\int_\Omega \mathbf{C}\cdot\nabla\times(\mathbf{u}\times\mathbf{b}) + \frac{1}{\mu_m\rho_r}\frac{1}{\mu_m\sigma}\int_\Omega(\nabla\times\mathbf{C})\cdot(\nabla\times\mathbf{B}) \\ &+ \frac{1}{\mu_m\rho_r}\int_\Omega \nabla r\cdot\mathbf{C} - \frac{1}{\mu_m\rho_r}\int_\Omega \nabla s\cdot\mathbf{B} \end{aligned} \tag{4.4.19}$$

From now on, the kinematic pressure will be used and therefore $p \leftarrow p/\rho$.

4.5 Stabilized Formulation for the Stationary, Linearized and Thermally Uncoupled Problem

In order to prevent the onset of numerical oscillations and spurious modes, the numerical scheme must be stabilized. Basically, the stabilization is aimed to circumvent the div–stability condition, ensuring that as $h \to 0$ at least, that discretely solenoidal functions tend to solenoidal functions. In this section the formulation of the stabilized scheme is presented for the stationary, linearized and thermally uncoupled problem.

4.5.1 Stability of the Galerkin approximation

As the first step in the building of the stabilized formulation of the numerical scheme for the MHD equations, the linearized uncoupled stationary problem is considered. Its variational form is: Find $\mathbf{U} \in W$ such that

$$A^{lin}(\mathbf{U},\mathbf{V}) = L(\mathbf{V}) \quad \forall \mathbf{V} \in W \tag{4.5.1}$$

Assuming that $\nabla\cdot\mathbf{a} = \mathbf{0}$ and $\nabla\cdot\mathbf{b} = \mathbf{0}$, A^{lin} satisfies the stability estimate:

$$A^{lin}(\mathbf{U},\mathbf{V}) = \nu\left\|\nabla u\right\|^2 + \frac{1}{\mu_m\rho_r}\frac{1}{\mu_m\sigma}\left\|\nabla\times\mathbf{B}\right\|^2. \tag{4.5.2}$$

This stability estimate together with the classical inf–sup conditions between $\left(H_0^1(\Omega)\right)^d$ and $L_0^2(\Omega)$ and between $H_0(curl,\Omega)$ and $H_0^1(\Omega)$, given respectively by:

$$\inf_{q\in L_0^2(\Omega)} \sup_{\mathbf{v}\in(H_0^1(\Omega))^d} \frac{(q,\nabla\cdot v)}{\|q\|\,\|\nabla v\|} \geq \beta_f > 0, \tag{4.5.3}$$

$$\inf_{s\in H_0^1(\Omega)} \sup_{\mathbf{C}\in H_0(curl,\Omega)} \frac{(\nabla s,\mathbf{C})}{\|\nabla s\|\left(\|\nabla\times\mathbf{C}\|+\|\mathbf{C}\|\right)} \geq \beta_m > 0, \tag{4.5.4}$$

where β_f and β_m are constants, are enough to guarantee that the linearized problem is well posed. Therefore, for each iteration k, given $\mathbf{u}^k$ and $\mathbf{B}^k$, there is a unique $\mathbf{U}^{k+1}=\left(\mathbf{u}^{k+1},p^{k+1},\mathbf{B}^k,s^{k+1}\right)$, solution of the linearized problem (4.5.1).

It can be shown that, under the same conditions for which the non linear problem has a unique solution, the sequence $\left\{\mathbf{U}^k\right\}_{k\geq 0}$ strongly converges to the unique solution of the nonlinear problem, the interested reader is referred to [58]. The proof of this result is technical, but quite simple, and follows the same strategy as for the stationary Navier–Stokes equation without magnetic coupling, for further detains see [15].

4.5.2 The Subgrid Scale Framework for a General CDR system of Equations

The basic idea of the stabilization method proposed here is based on the subgrid scale concept introduced by Hughes [29]. The ideas and concepts presented are a summary of the approach described in [12].

The starting idea is to split the continuous space as $W=W_h\oplus\widetilde{W}$, where W_h is the finite element space in which the approximate solution will be sought. $\widetilde{W}$ is called the *space of subscales* or *subgrid scales*. Keeping this split of spaces in mind, it is possible to write the continuous problem as the following system of equations:

$$A^{lin}(\mathbf{U}_h,\mathbf{V}_h)+A^{lin}(\widetilde{\mathbf{U}},\mathbf{V}_h)=L(\mathbf{V}_h)\quad\forall\mathbf{V}_h\in W_h \tag{4.5.5}$$

$$A^{lin}(\mathbf{U}_h,\widetilde{\mathbf{V}})+A^{lin}(\widetilde{\mathbf{U}},\widetilde{\mathbf{V}})=L\left(\widetilde{\mathbf{V}}\right)\quad\forall\widetilde{\mathbf{V}}\in\widetilde{W} \tag{4.5.6}$$

where $\mathbf{U}=\mathbf{U}_h+\widetilde{\mathbf{U}}$ and $\mathbf{U}\in W_h,\widetilde{\mathbf{U}}\in\widetilde{W}$. It is useful for the following to introduce the notation:

$$\int_{\Omega'}:=\sum_{e=1}^{n_el}\int_{\Omega^e},\int_{\partial\Omega'}:=\sum_{e=1}^{n_el}\int_{\partial\Omega^e}$$

where n_{el} is the number of elements of the finite element partition used to built W_h and Ω^e denotes the domain of element e. The next step is integrating by parts all terms in $A^{lin}(\widetilde{\mathbf{U}},\mathbf{V}_h)$ in (4.5.5) and the left hand side term of (4.5.6) within each element domain, this yields the following expression:

$$A^{lin}(\mathbf{U}_h,\mathbf{V}_h)+\int_{\partial\Omega'}\widetilde{\mathbf{U}}^t n_i\left(\mathbf{K}_{ij}\frac{\partial\mathbf{V}_h}{\partial x_j}-\mathbf{A}_i^f\mathbf{V}_h\right)+\int_{\Omega'}\widetilde{\mathbf{U}}^t\mathcal{L}^*\left(\mathbf{V}_h\right)=L\left(\mathbf{V}_h\right) \quad (4.5.7)$$

$$\int_{\partial\Omega'}\widetilde{\mathbf{V}}^t n_i(\mathbf{K}_{ij}\frac{\partial}{\partial x_j}(\mathbf{U}_h+\widetilde{\mathbf{U}})-\mathbf{A}_i^f(\mathbf{U}_h+\widetilde{\mathbf{U}}))+\int_{\Omega'}\widetilde{\mathbf{V}}^t\mathcal{L}(\mathbf{U}_h)=\int_{\Omega'}\widetilde{\mathbf{V}}^t\left[\mathbf{F}-\mathcal{L}\left(\mathbf{U}_h\right)\right] \quad (4.5.8)$$

where n_i is the i-th component of the exterior normal to $\partial\Omega^e$ and $\mathcal{L}^*$ is the adjoint operator of $\mathcal{L}$ with homogeneous Dirichlet boundary conditions, given by:

$$\mathcal{L}^*(\mathbf{U}):=-\frac{\partial}{\partial x_i}\left(\mathbf{A}_i^t\mathbf{U}\right)-\frac{\partial}{\partial x_i}\left(\mathbf{K}_{ij}^t\frac{\partial\mathbf{U}}{\partial x_j}\right) \quad (4.5.9)$$

Equation (4.5.8) is equivalent to:

$$\mathcal{L}(\widetilde{\mathbf{U}})=\mathbf{F}-\mathcal{L}(\mathbf{U}_h)+\mathbf{V}_{h,ort} \quad \text{in} \quad \Omega^e, \quad (4.5.10)$$

$$\widetilde{\mathbf{U}}=\widetilde{\mathbf{U}}_{ske} \quad \text{on} \quad \partial\Omega^e, \quad (4.5.11)$$

where $\mathbf{V}_{h,ort}$ is obtained from the condition that $\widetilde{\mathbf{U}}$ must belong to $\widetilde{W}$, not to the whole space W, and $\widetilde{\mathbf{U}}_{ske}$ is a function defined on the element boundaries and it is such that:

$$\mathbf{q}_n:=n_i\left(\mathbf{K}_{ij}\frac{\partial}{\partial x_j}(\mathbf{U}_h+\widetilde{\mathbf{U}})-\mathbf{A}_i^f(\mathbf{U}_h+\widetilde{\mathbf{U}})\right) \quad (4.5.12)$$

is continuous across inter–element boundaries, and therefore the first term in the left-hand-side of (4.5.8) vanishes.

Different subgrid scale (SGS) stabilization methods can be devised depending on the way problem (4.5.10)-(4.5.11) is approximated. The intent of this research is not to propose a new methodology but rather how to apply a well established formulation to the incompressible MHD problem. This well known method can be obtained by approximating the subscales by the algebraic expression:

$$\widetilde{\mathbf{U}}\approx\boldsymbol{\tau}\left[\mathbf{F}-\mathcal{L}\left(\mathbf{U}_h\right)\right] \quad (4.5.13)$$

where $\boldsymbol{\tau}$ is a $n_{unk}\times n_{unk}$ matrix of stabilization parameters, the expression of which is discussed in the following subsection. To close the approximation, the inter–elements boundary terms in (4.5.7) is neglected, this can be understood as taking $\widetilde{\mathbf{U}}_{ske}=\mathbf{0}$ on the inter–elements boundaries. The final problem is: Find $\mathbf{U}_h\in W_h$ such that:

$$A^{lin}(\mathbf{U}_h,\mathbf{V}_h)+\int_{\Omega'}\widetilde{\mathbf{U}}^t\mathcal{L}^*\left(\mathbf{V}_h\right)=L\left(\mathbf{V}_h\right)\quad\forall\mathbf{V}_h\in W_h$$

which, upon substitution of the subscales given by (4.5.13), yields the following discrete problem: Find $\mathbf{U}_h\in W_h$ such that:

$$A_{stab}^{lin}(\mathbf{U}_h, \mathbf{V}_h) = L_{stab}(\mathbf{V}_h) \quad \forall \mathbf{V}_h W_h \tag{4.5.14}$$

where the bilinear form A_{stab}^{lin} and the linear form L_{stab} are now given by:

$$A_{stab}^{lin}(\mathbf{U}_h, \mathbf{V}_h) = A^{lin}(\mathbf{U}_h, \mathbf{V}_h) - \int_{\Omega'} \mathcal{L}^*(\mathbf{V}_h)^t \boldsymbol{\tau} \mathcal{L}(\mathbf{U}_h), \tag{4.5.15}$$

$$L_{stab}(\mathbf{V}_h) = L(\mathbf{V}_h) - \int_{\Omega'} \mathcal{L}^*(\mathbf{V}_h)^t \boldsymbol{\tau} \mathbf{F}. \tag{4.5.16}$$

4.5.3 Stabilized Finite Element Approximation for the Linearized MHD Problem

In this section, a stabilized finite element to approximate problem (4.5.1) is presented. The first step is to recast the problem as a system of linear convection–diffusion equations. It is in this general setting that the finite element approximation will be described.

Stabilization for this problem has several goals. The first one is to avoid the need to satisfy the discrete version of the inf–sup conditions (4.5.3) and (4.5.4), which will allow us to use different interpolation for the variational problem, therefore avoiding the discrete version of the inf–sup conditions will lead to use equal order and continuous interpolation for all unknowns. The second goal is to obtain error estimates valid in the limit $\nu \to 0$ and $\mu_m \sigma \to \infty$, that is, convection dominated flows, both in the Navier–Stokes equations and in the Maxwell equations. Finally the third goal is to account properly for the coupling of the hydrodynamic and the magnetic problems ($\mu_m \rho_r \to 0$). That these goals are all satisfied will be seen in the error estimate to be presented.

Up to now, the *algebraic* version of the SGS stabilization has been described in a general setting. The goal now is to apply this stabilization to the MHD problem under consideration. In order to accomplish this task, the adjoint operator of the linearized uncoupled MHD problem $\mathcal{L}^*(\mathbf{V}_h)$ is now given by:

$$\mathcal{L}^* = \begin{bmatrix} -\mathbf{a}\cdot\nabla\mathbf{v} - \nu\Delta\mathbf{v} - \nabla q - \frac{1}{\mu_m\rho_r}\mathbf{b}\times(\nabla\times\mathbf{C}) \\ -\nabla\cdot\mathbf{v} \\ \frac{1}{\mu_m\rho_r}\nabla\times(\mathbf{v}\times\mathbf{b}) + \frac{1}{\mu_m\rho_r}\frac{1}{\mu_m\sigma}\nabla\times(\nabla\times\mathbf{C}) - \frac{1}{\mu_m\rho_r}\nabla s \\ -\frac{1}{\mu_m\rho_r}\nabla\cdot\mathbf{C} \end{bmatrix} \tag{4.5.17}$$

To define the method for the particular MHD problem, an expression for the matrix of stabilization parameters τ needs to be proposed. There is no general way to define it for system of equations (4.2.1). It must be defined for each particular problem taking into account its stability deficiencies.

The stability of the numerical scheme can be improved maintaining optimal accuracy by taking a simple diagonal expression for τ, with one scalar component for each of the equations. In the 3D case the expression for τ is:

$$\boldsymbol{\tau} = \mathrm{diag}(\tau_1, \tau_1, \tau_1, \tau_2, \tau_3, \tau_3, \tau_3, \tau_4) \tag{4.5.18}$$

Using this expression and (4.5.17), it follows that the stabilized bilinear form that needs to be considered in problem (4.5.14) is:

$$
\begin{aligned}
&A^{lin}_{stab}(\mathbf{U}_h,\mathbf{V}_h) = A^{lin}(\mathbf{U}_h,\mathbf{V}_h) - \int_{\Omega'} \mathcal{L}^*\left(\mathbf{V}_h\right)^t \boldsymbol{\tau}\mathcal{L}\left(\mathbf{U}_h\right) = \\
&\left(\mathbf{a}\cdot\nabla\mathbf{v}_h,\mathbf{v}_h\right) + \nu\left(\nabla\mathbf{u}_h,\nabla\mathbf{v}_h\right) - \left(p_h,\nabla\cdot\mathbf{v}_h\right) + \left(q_h,\nabla\cdot\mathbf{u}_h\right) \\
&+ \frac{1}{\mu_m\rho_r}\left(\mathbf{B}_h,\nabla\times\left(\mathbf{v}_h\times\mathbf{b}\right)\right) - \frac{1}{\mu_m\rho_r}\left(\mathbf{C}_h,\nabla\times\left(\mathbf{u}_h\times\mathbf{b}\right)\right) \\
&+ \frac{1}{\mu_m\rho_r}\frac{1}{\mu_m\sigma}\left(\nabla\times\mathbf{B}_h,\nabla\times\mathbf{C}_h\right) \\
&+ \frac{1}{\mu_m\rho_r}\left(\nabla r_h,\mathbf{C}_h\right) - \frac{1}{\mu_m\rho_r}\left(\nabla s_h,\mathbf{B}_h\right) \\
&+ \left(X_u\left(\mathbf{v}_h,q_h,\mathbf{C}_h\right) + \nu\Delta\mathbf{v}_h, \tau_1\left(X_u\left(\mathbf{u}_h,p_h,\mathbf{B}_h\right) - \nu\Delta\mathbf{u}_h\right)\right)_h \\
&+ \left(\nabla\cdot\mathbf{v}_h,\tau_2(\nabla\cdot\mathbf{u}_h)\right)_h \\
&+ \left(X_B(s_h,\mathbf{v}_h) - \frac{1}{\mu_m^2\rho_r\sigma}\nabla\times(\nabla\times\mathbf{C}_h), \tau_3(X_B(r_h,\mathbf{u}_h) - \frac{1}{\mu_m^2\rho_r\sigma}\nabla\times(\nabla\times\mathbf{B}_h))\right)_h \\
&+ \frac{1}{\mu_m^2\rho_r^2}\left(\nabla\cdot\mathbf{C}_h,\tau_4(\nabla\cdot\mathbf{B}_h)\right)_h
\end{aligned}
\tag{4.5.19}
$$

where the following abbreviations have been introduced:

$$
X_u\left(\mathbf{v}_h,q_h,\mathbf{C}_h\right) := \mathbf{a}\cdot\nabla\mathbf{v}_h + \nabla q_h + \frac{1}{\mu_m\rho_r}\mathbf{b}\times\left(\nabla\times\mathbf{C}_h\right),
$$

$$
X_B(s_h,\mathbf{v}_h) = -\frac{1}{\mu_m\rho_r}\nabla\times\left(\mathbf{v}_h\times\mathbf{b}\right) + \frac{1}{\mu_m\rho_r}\nabla s_h,
$$

and $(\bullet,\bullet)_h$ is defined as:

$$
\left(f,g\right)_h := \sum_{e=1}^{n_e l}\int_{\Omega^e} fg.
$$

Finally, the right–hand–side of the stabilized problem (4.5.14) is given by:

$$
\begin{aligned}
L_{stab}\left(\mathbf{V}_h\right) &= L\left(\mathbf{V}_h\right) - \int_{\Omega'}\mathcal{L}^*\left(\mathbf{V}_h\right)^t\boldsymbol{\tau}\mathbf{F} \\
&= \left\langle\mathbf{f}_f,\mathbf{v}\right\rangle + \frac{1}{\mu_m\rho_r}\left(\mathbf{f}_m,\mathbf{C}\right) \\
&+ \left(X_u(\mathbf{v}_h,q_h,\mathbf{C}_h) + \nu\Delta\mathbf{v}_h, \tau_1\mathbf{f}_f\right)_h \\
&+ \left(X_B(s_h,\mathbf{v}_h) - \frac{1}{\mu_m^2\rho_r\sigma}\nabla\times(\nabla\times\mathbf{C}_h), \tau_3\mathbf{f}_m\right)_h
\end{aligned}
\tag{4.5.20}
$$

The definition of the stabilized finite element method is now complete up to the expression of the stabilization parameters. The expression proposed for the MHD problem is:

$$\tau_1 = \alpha^{-1}\left(1+\frac{1}{\sqrt{\alpha\gamma}}\beta\right)^{-1} \tag{4.5.21}$$

$$\tau_2 = c_5\frac{h^2}{\tau_1} \tag{4.5.22}$$

$$\tau_3 = \gamma^{-1}\left(1+\frac{1}{\sqrt{\alpha\gamma}}\beta\right)^{-1} \tag{4.5.23}$$

$$\tau_4 = c_6\rho_r^2\mu_m^2\frac{h^2}{\tau_3} \tag{4.5.24}$$

where α, β and γ are given by:

$$\alpha: = c_1\frac{a}{h}+c_2\frac{\nu}{h^2} \tag{4.5.25}$$

$$\beta: = c_3\frac{1}{\mu_m\rho_r}\frac{b}{h} \tag{4.5.26}$$

$$\gamma: = c_4\frac{1}{\mu_m\rho_r}\frac{1}{\mu_m\sigma}\frac{1}{h^2} \tag{4.5.27}$$

It is understood that this expressions are evaluated element by element. Here, a is the maximum norm of the velocity field $\mathbf{a}$ computed in the element under consideration. Likewise, b denotes the maximum norm of the magnetic field intensity $\mathbf{b}$ in the same element and h denotes the diameter of the element. The constants c_i with $i = 1,2,3,4,5,6$ are independent of the physical parameters of the problem and the mesh discretization. In the numerical calculations the values for this constants are $c_1 = 2$, $c_2 = 4$, $c_3 = 1$, $c_4 = 4$, $c_5 = 1$ and $c_6 = 1$.

In the following subsection this choice is justified from the numerical analysis of the problem. The approach is constructive, posing conditions on the stabilization parameters obtained from the requirement that the method is stable (coercive) and optimally accurate. For simplicity, the parameters τ_i with $i = 1,2,3,4$ are considered constant.

4.5.4 Numerical Analysis and Design of the Stabilization Parameters

In this subsection, the formulation introduced before is analyzed and, in particular, to justify the choice (4.5.21)–(4.5.24). For the sake of simplicity, a and b are assumed constant. Likewise, the finite element meshes are assumed quasi–uniform. In this case, h in (4.5.21)–(4.5.24) can be taken the same for all elements (the maximum element diameter), and therefore τ_i with $i = 1,2,3,4$ are also constant. Moreover, for quasi–uniform meshes the following estimates hold:

$$\|\nabla v_h\| \leq \frac{C_{inv}}{h}\|v_h\|, \qquad \|\nabla\nabla v_h\| \leq \frac{C_{inv}}{h}\|\nabla v_h\| \tag{4.5.28}$$

for any function v_h in the finite element space and for a certain constant C_{inv}.

The stability and convergence analysis will be made using the following mesh–dependent norm:

$$\begin{aligned}
|||\mathbf{U}_h||| :=& \nu \left\|\nabla \mathbf{u}_h\right\|^2 + \frac{1}{\mu_m \rho_r}\frac{1}{\mu_m \sigma}\left\|\nabla \times \mathbf{B}_h\right\|^2 \\
&+ \tau_1 \left\| \mathbf{a}\cdot\nabla\mathbf{u}_h + \nabla p_h + \frac{1}{\mu_m\rho_r}\mathbf{b}\times(\nabla\times\mathbf{B}_h)\right\|^2 + \tau_2\left\|\nabla\cdot\mathbf{u}_h\right\| \\
&+ \tau_3 \frac{1}{\mu_m^2\rho_r^2}\left\|-\nabla\times(\mathbf{u}_h\times\mathbf{b}) + \nabla r_h\right\|^2 + \tau_4\frac{1}{\mu_m^2\rho_r^2}\left\|\nabla\cdot\mathbf{B}_h\right\|^2 \\
&\equiv \nu\left\|\nabla\mathbf{u}_h\right\|^2 + \frac{1}{\mu_m\rho_r}\frac{1}{\mu_m\sigma}\left\|\nabla\times\mathbf{B}_h\right\|^2 \\
&+ \tau_1\left\|X_u(\mathbf{u}_h,p_h,\mathbf{B}_h)\right\|^2 + \tau_2\left\|\nabla\cdot\mathbf{u}_h\right\|^2 \\
&+ \tau_3\left\|X_B(r_h,\mathbf{u}_h)\right\|^2 + \tau_4\frac{1}{\mu_m^2\rho_r^2}\left\|\nabla\cdot\mathbf{B}_h\right\|^2
\end{aligned} \tag{4.5.29}$$

In all that follows, C will denote a positive constant, not necessarily the same at different appearances.

4.5.4.1 Coercivity

The first step is proving stability in the form of coercivity of the bilinear form (4.5.19). It is immediately checked that:

$$\begin{aligned}
A_{stab}^{lin}(\mathbf{U}_h,\mathbf{V}_h) =& A^{lin}(\mathbf{U}_h,\mathbf{V}_h) - \int_{\Omega'}\mathcal{L}^*\left(\mathbf{V}_h\right)^t\boldsymbol{\tau}\mathcal{L}\left(\mathbf{U}_h\right) \\
=& \nu\left\|\nabla\mathbf{u}\right\|^2 + \frac{1}{\mu_m\rho_r}\frac{1}{\mu_m\sigma}\left\|\nabla\times\mathbf{B}\right\|^2 \\
&+\tau_1\left\|X_u(\mathbf{u}_h,p_h,\mathbf{B}_h)\right\|^2 - \tau_1\nu^2\left\|\Delta\mathbf{u}_h\right\|^2 + \tau_2\left\|\nabla\cdot\mathbf{u}_h\right\|^2 \\
&+\tau_3\left\|X_B\left(r_h,\mathbf{u}_h\right)\right\|^2 - \tau_3\frac{1}{\mu_m^2\rho_r^2}\frac{1}{\mu_m^2\sigma^2}\left\|\nabla\times\nabla\times\mathbf{B}\right\|^2 \\
&+\tau_4\frac{1}{\mu_m^2\rho_r^2}\left\|\nabla\cdot\mathbf{B}_h\right\|^2
\end{aligned} \tag{4.5.30}$$

Using the second inverse estimate in (4.5.28), it is clear that the necessary and sufficient condition for A_{stab}^{lin} to be coercive is that:

$$\nu - \tau_1\nu^2\frac{C_{inv}^2}{h^2} \geq \alpha\nu \Longleftrightarrow \tau_1 \leq (1-\alpha)\frac{1}{\nu}\frac{h^2}{C_{inv}^2}, \tag{4.5.31}$$

$$\frac{1}{\mu_m^2\rho_r\sigma} - \tau_3\frac{1}{\mu_m^4\rho_r^2\sigma^2}\frac{C_{inv}^2}{h^2} \geq \alpha\frac{1}{\mu_m^2\rho_r\sigma} \Longleftrightarrow \tau_3 \leq (1-\alpha)\mu_m^2\rho_r\sigma\frac{h^2}{C_{inv}^2} \tag{4.5.32}$$

with $0 < \alpha < 1$. Conditions (4.5.31) and (4.5.32) yield:

$$A^{lin}_{stab}(\mathbf{U}_h, \mathbf{V}_h) \geq C \, |||\mathbf{U}_h||| \tag{4.5.33}$$

for a constant C independent of the discretization and of the physical parameters. Constant C only depends on the constants of the stabilization parameters.

4.5.4.2 Optimal Accuracy

In the previous subsection, conditions (4.5.31) and (4.5.32) over the stabilization parameters were obtained by requiring stability, the rest of the conditions will be obtained by imposing that the stabilized method proposed is optimally accurate, which will lead to optimal convergence.

For a function v, let $\pi_h(v)$ be its optimal finite approximation. It is assumed that the following interpolation estimate holds:

$$\epsilon_i(v) := \|v - \pi_h(v)\|_{H^i(\Omega)} \leq C h^{k+1-i} \|v\|_{H^{k+1}(\Omega)} \qquad i = 0, 1, \tag{4.5.34}$$

where $\|v\|_{H^q(\Omega)}$ is the $H^q(\Omega)$–norm of v, that is, the sum of the $L^2(\Omega)$–norm of the derivatives of v up to degree q, and k is the degree of the finite element approximation.

Next, it will be proved that the error function of the formulation is:

$$E(h) := \tau_1^{-1/2} \epsilon_0(\mathbf{u}) + \tau_2^{-1/2} \epsilon_0(p) + \tau_3^{-1/2} \epsilon_0(\mathbf{B}) + \tau_4^{-1/2} \epsilon_0(r) \tag{4.5.35}$$

the conditions on the stabilization parameters to be obtained, will in fact show that this is indeed the error function and that this error functional is optimal.

Let $\mathbf{U}$ be the solution of the continuous problem and $\pi_h(\mathbf{U})$ its optimal finite element approximation. The accuracy estimate that will be needed to prove convergence later on is:

$$A^{lin}_{stab}(\mathbf{U} - \pi_h(\mathbf{U}), \mathbf{V}_h) \leq C E(h) \, |||\mathbf{V}_h|||\,, \tag{4.5.36}$$

for any finite element function $\mathbf{V}_h$. This can be proved by showing that both the Galerkin and the stabilization terms in A^{lin}_{stab} satisfy estimate (4.5.36). Starting with Galerkin contribution:

$$
\begin{aligned}
&A^{lin}(\mathbf{U}-\pi_h(\mathbf{U}),\mathbf{V}_h)=\\
&-(\mathbf{u}-\pi_h(\mathbf{u}),\mathbf{a}\cdot\nabla\mathbf{v}_h)+\nu(\nabla(\mathbf{u}-\pi_h(\mathbf{u})),\nabla\mathbf{v}_h)\\
&-(p-\pi_h(p),\nabla\cdot\mathbf{v}_h)-(\nabla q_h,\mathbf{u}-\pi_h(\mathbf{u}))\\
&-\frac{1}{\mu_m\rho_r}(\mathbf{u}-\pi_h(\mathbf{u}),\mathbf{b}\times\nabla\times\mathbf{C}_h)+\frac{1}{\mu_m\rho_r}(\mathbf{B}-\pi_h(\mathbf{B}),\nabla\times(\mathbf{v}_h\times\mathbf{b}))\\
&+\frac{1}{\mu_m^2\rho_r\sigma}(\nabla\times\mathbf{C}_h,(\mathbf{B}-\pi_h(\mathbf{B})))-\frac{1}{\mu_m\rho_r}(r-\pi_h(r),\nabla\cdot\mathbf{C}_h)\\
&-\frac{1}{\mu_m\rho_r}(\nabla s_h,\mathbf{B}-\pi_h(\mathbf{B}))\\
&\leq C(\epsilon_0(\mathbf{u})\tau_1^{-1/2}\tau_1^{1/2}\left\|X_u(\mathbf{v}_h,q_h,\mathbf{C}_h)\right\|+\nu^{1/2}\epsilon_1(\mathbf{u})\nu^{1/2}\left\|\nabla\mathbf{v}_h\right\|\\
&+\epsilon_0(p)\tau_2^{-1/2}\tau_2^{1/2}\left\|\nabla\cdot\mathbf{v}_h\right\|\\
&+\epsilon_0(\mathbf{B})\tau_3^{-1/2}\tau_3^{1/2}\left\|X_B(s_h,\mathbf{v}_h)\right\|+\frac{1}{(\mu_m\rho_r\mu_m\sigma)^{1/2}}\epsilon_1(\mathbf{B})\frac{1}{(\mu_m\rho_r\mu_m\sigma)^{1/2}}\left\|\nabla\times\mathbf{C}_h\right\|\\
&+\epsilon_0(r)\tau_4^{-1/2}\tau_4^{1/2}\frac{1}{\mu_m\rho_r}\left\|\nabla\cdot\mathbf{C}_h\right\|)
\end{aligned}
\tag{4.5.37}
$$

Conditions (4.5.31) and (4.5.32) and the expression of the interpolation errors imply:

$$
\nu^{1/2}\epsilon_1(\mathbf{u})\leq C\epsilon_0(\mathbf{u})\tau_1^{-1/2},\qquad\frac{1}{(\mu_m\rho_r\mu_m\sigma)^{1/2}}\epsilon_1(\mathbf{B})\leq C\epsilon_0(\mathbf{B})\tau_3^{-1/2}
$$

and therefore from (4.5.37) it follows that the Galerkin contribution $A^{lin}(\mathbf{U}-\pi_h(\mathbf{U}),\mathbf{V}_h)$ to $A^{lin}_{stab}(\mathbf{U}-\pi_h(\mathbf{U}),\mathbf{V}_h)$ can be found in (4.5.36). It remains to prove that also the stabilization terms can be bounded in this way:

$$
\begin{aligned}
&-\int_{\Omega'} \mathcal{L}^*(\mathbf{V}_h)^t \boldsymbol{\tau} \mathcal{L}(\mathbf{U}-\pi_h(\mathbf{U}))\\
&=(X_u(\mathbf{u}-\pi_h(\mathbf{u}),p-\pi_h(p),\mathbf{B}-\pi_h(\mathbf{B}))-\nu\Delta(\mathbf{u}-\pi_h(\mathbf{u})),\\
&\quad \tau_1(X_u(\mathbf{v}_h,q_h,\mathbf{C}_h)+\nu\Delta\mathbf{v}_h)_h\\
&+(\nabla\cdot(\mathbf{u}-\pi_h(\mathbf{u})),\tau_2\nabla\cdot\mathbf{v}_h)_h\\
&+(X_B(r-\pi_h(r),\mathbf{u}-\pi_h(\mathbf{u}))+\frac{1}{\mu_m\rho_r\mu_m\sigma}\nabla\times\nabla\times(\mathbf{B}-\pi_h(\mathbf{B})),\\
&\quad \tau_3 X_B(s_h,\mathbf{v}_h)-\frac{1}{\mu_m\rho_r\mu_m\sigma}\nabla\times\nabla\times\mathbf{C}_h)_h\\
&+\frac{1}{\mu_m^2\rho_r^2}(\nabla\cdot(\mathbf{B}-\pi_h(\mathbf{B})),\tau_4\nabla\cdot\mathbf{C}_h)_h\\
&\leq C(\tau_1^{1/2}\left\|X_u(\mathbf{u}-\pi_h(\mathbf{u}),p-\pi_h(p),\mathbf{B}-\pi_h(\mathbf{B}))\right\|+\tau_1^{1/2}\nu\left\|\Delta(\mathbf{u}-\pi_h(\mathbf{u}))\right\|)\\
&\times(|||\mathbf{V}_h|||+\tau_1^{1/2}\nu\left\|\Delta\mathbf{v}_h\right\|)\\
&+C\tau_2^{1/2}\epsilon_1(\mathbf{u})\left\|\mathbf{V}_h\right\|\\
&+C(\tau_3^{1/2}\left\|X_B(r-\pi_h(r),\mathbf{u}-\pi_h(\mathbf{u}))\right\|+\tau_3^{1/2}\frac{1}{\mu_m\rho_r\mu_m\sigma}\left\|\nabla\times\nabla\times(\mathbf{B}-\pi_h(\mathbf{B}))\right\|)\\
&\times(|||\mathbf{V}_h|||+\tau_3^{1/2}\frac{1}{\mu_m\rho_r\mu_m\sigma}\left\|\nabla\times\nabla\times\mathbf{C}_h\right\|)\\
&+C\tau_4^{1/2}\frac{1}{\mu_m\rho_r}\epsilon_1(\mathbf{B})\left\|\mathbf{V}_h\right\|
\end{aligned}
\tag{4.5.38}
$$

Using once again conditions (4.5.31) and (4.5.32) and the inverse estimates (4.5.28), the following expressions are obtained:

$$
\tau_1^{1/2}\nu\left\|\Delta\mathbf{v}_h\right\|\leq C\tau_1^{1/2}\nu^{1/2}\frac{C_{inv}}{h}\nu^{1/2}\left\|\nabla\mathbf{v}_h\right\|\leq C\left|||\mathbf{V}_h|||\right., \tag{4.5.39}
$$

$$
\begin{aligned}
\tau_3^{1/2}\frac{1}{\mu_m^2\rho_r\sigma}\left\|\nabla\times\nabla\times\mathbf{C}_h\right\|\leq C\tau_3^{1/2}\frac{1}{(\mu_m^2\rho_r\sigma)^{1/2}}\frac{C_{inv}}{h}\frac{1}{(\mu_m^2\rho_r\sigma)^{1/2}}\left\|\nabla\times\mathbf{C}_h\right\|\\
\leq C\left|||\mathbf{V}_h|||\right.
\end{aligned}
\tag{4.5.40}
$$

So far, any aditional condition has been posed on the stabilization parameters other than (4.5.31) and (4.5.32), found from the requirement of coercivity. The rest of the conditions will come from the requirement of optimal accuracy.

From (4.5.38), the next expression can be obtained:

$$
\begin{aligned}
&-\int_{\Omega'} \mathcal{L}^*(\mathbf{V}_h)^t \boldsymbol{\tau} \mathcal{L}(\mathbf{U}-\pi_h(\mathbf{U})) \\
&\leq C\,|||\mathbf{V}_h|||\,\tau_1^{1/2}\left(\frac{a}{h}\epsilon_0(\mathbf{u})+\frac{\nu}{h^2}\epsilon_0(\mathbf{u})+\frac{1}{h}\epsilon_0(p)+\frac{1}{\mu_m\rho_r}\frac{b}{h}\epsilon_0(\mathbf{B})\right) \\
&+C\,|||\mathbf{V}_h|||\,\tau_2^{1/2}\frac{1}{h}\epsilon_0(\mathbf{u}) \\
&+C\,|||\mathbf{V}_h|||\,\tau_3^{1/2}\frac{1}{\mu_m\rho_r}\left(\frac{b}{h}\epsilon_0(\mathbf{u})+\frac{1}{\mu_m\sigma}\frac{1}{h^2}\epsilon_0(\mathbf{B})+\frac{1}{h}\epsilon_0(r)\right) \\
&+C\,|||\mathbf{V}_h|||\,\tau_4^{1/2}\frac{1}{\mu_m\rho_r}\frac{1}{h}\epsilon_0(\mathbf{B}) \\
&\leq C\,|||\mathbf{V}_h|||\left[\tau_1^{1/2}(\frac{a}{h}+\frac{\nu}{h^2})+\frac{\tau_3^{1/2}}{\mu_m\rho_r}\frac{b}{h}+\tau_2^{1/2}\frac{1}{h}\right]\epsilon_0(\mathbf{u}) \\
&+C\,|||\mathbf{V}_h|||\left[\tau_1^{1/2}\frac{1}{h}\right]\epsilon_0(p) \\
&+C\,|||\mathbf{V}_h|||\left[\frac{\tau_1^{1/2}}{\mu_m\rho_r}\frac{b}{h}+\frac{\tau_3^{1/2}}{\mu_m\rho_r}\frac{1}{\mu_m\sigma}\frac{1}{h^2}+\frac{\tau_4^{1/2}}{\mu_m\rho_r}\frac{b}{h}\right]\epsilon_0(\mathbf{B}) \\
&+C\,|||\mathbf{V}_h|||\left[\frac{\tau_3^{1/2}}{\mu_m\rho_r}\frac{1}{h}\right]\epsilon_0(r)
\end{aligned}
\tag{4.5.41}
$$

From the definitions (4.5.21)–(4.5.24) of the stabilization parameters it follows that these terms can be bounded also as indicated in (4.5.36).

4.5.4.3 Convergence

As a trivial consequence of the properties of stability and accuracy in the sense of (4.5.36), it is trivial to show that the method is optimally convergent. From the orthogonality property $A_{stab}^{lin}(\mathbf{U}-\mathbf{U}_h,\mathbf{V})=0$ for any finite element function $\mathbf{V}_h$, a consequence of the consistency of the method, the next expression is obtained:

$$
\begin{aligned}
C\,\|\pi_h(\mathbf{U})-\mathbf{U}_h\|^2 \leq & A_{stab}^{lin}(\pi_h(\mathbf{U})-\mathbf{U}_h,\pi_h(\mathbf{U})-\mathbf{U}_h) \\
\leq & A_{stab}^{lin}(\pi_h(\mathbf{U})-\mathbf{U},\pi_h(\mathbf{U})-\mathbf{U}_h) \\
\leq & CE(h)\,|||\pi_h(\mathbf{U})-\mathbf{U}_h|||\,,
\end{aligned}
\tag{4.5.42}
$$

from where $|||\pi_h(\mathbf{U})-\mathbf{U}_h||| \leq CE(h)$. Now the triangle inequality implies:

$$
\begin{aligned}
|||\mathbf{U}-\mathbf{U}_h||| &\leq |||\mathbf{U}-\pi_h\mathbf{U}||| + |||\pi_h(\mathbf{U})-\mathbf{U}_h||| \\
&\leq |||\mathbf{U}-\pi_h\mathbf{U}||| + CE(h)
\end{aligned}
\tag{4.5.43}
$$

A trivial check using the expression of the norm $|||\bullet|||$ given by (4.5.29). the interpolation estimates (4.5.34) and the stabilization parameters (4.5.21)–(4.5.24) shows that $|||\mathbf{U} - \pi_h\mathbf{U}||| \leq CE(h)$, from where:

$$|||\mathbf{U} - \mathbf{U}_h||| \leq CE(h). \tag{4.5.44}$$

The fact that this error estimate is exactly the same as the estimate for the interpolation error $|||\mathbf{U} - \pi_h\mathbf{U}||| \leq CE(h)$ justifies why it has to be considered "optimal". Moreover, a simple inspection of what happens in the limit of dominant second order terms shows that in this case the error estimate reduces to the estimate that could be found using the Galerkin method using finite element spaces satisfying the discrete form of (4.5.3)–(4.5.4), but now, however, using equal interpolation for all the variables. Likewise, in the limit $\nu \to 0$ and $\mu_m\sigma \to \infty$, the error estimate (4.5.44) does not blow up and the result can also be considered optimal. The interested reader is referred to [13] for a similar discussion.

4.5.4.4 Remarks on Non Smooth Solutions

It known that problems involving the Maxwell equations may exhibit solutions strictly in $H_0(curl, \Omega)$ for the magnetic field, i.e. non smooth solutions. These solutions appear when the domain Ω is non convex, i.e. the domain presents re–entrant corners. Methods based on penalization used to enforce divergence condition on the magnetic field, fail to converge to these non smooth solutions. In order to address this problem, we need to weight the terms that introduce this divergence control or use mixed interpolations. Neither of these options is easily applicable. The former option is not easy to apply to general three dimensional problems and the latter option requires the discrete version of the inf–sup condition (4.5.4). These drawbacks render stabilization methods, as the one proposed in this research, as the only alternative to use the simple continuous Lagrangian approximation of the magnetic field. However, in the formulation we propose the last term in (4.5.19)gives control to the divergence in the magnetic field, therefore expressions for τ_4 smaller than the one given in (4.5.24) might be required.

4.6 Final Numerical Scheme

The final numerical scheme that is proposed is obtained by applying the finite element stabilization technique described in Section 4.5 to the time discrete and linearized problem (4.4.10). The space discretization of these equations, adding stabilization terms as those that appear in (4.5.19) and (4.5.20) for the stationary thermally uncoupled problem, will lead to the following algorithm:

For $n = 0, 1, 2, \ldots$, given $\mathbf{u}^n, p^n, \mathbf{B}^n, r^n$ and ϑ^n, find $\mathbf{u}_h^{n+1}, p_h^{n+1}, \mathbf{B}_h^{n+1}, r_h^{n+1}$ and ϑ_h^{n+1}, as the converged solutions of the following iterative algorithm:

$$
\begin{aligned}
(\delta_t \mathbf{u}_h^{n,k+1}, \mathbf{v}_h) &+ A_{uu}(\mathbf{u}_h^{n+\theta,k}, \mathbf{u}_h^{n+\theta,k+1}, \mathbf{v}_h) + A_{uB}(\mathbf{B}_h^{n+\theta,k+1}, \mathbf{B}_h^{n+\theta,k}, \mathbf{v}_h) \\
&+ A_{u\vartheta}(\vartheta_h^{n+\theta,e(k)}, \mathbf{v}_h) - b_u(p_h^{n+1,k+1}, \mathbf{v}_h) \\
&+ \tau_1^{n+\theta,k} \left(\mathbf{u}_h^{n+\theta,k} \cdot \nabla \mathbf{v}_h + \nu \Delta \mathbf{v}_h, \mathbf{R}_{h,u}^{n+\theta,k+1} \right)_h \\
&+ \tau_2^{n+\theta,k} \left(\nabla \cdot \mathbf{v}_h, R_{h,p}^{n+\theta,k+1} \right)_h \\
&+ \tau_3^{n+\theta,k} \left(-\nabla \times (\mathbf{v}_h \times \mathbf{B}_h^{n+\theta}), \mathbf{R}_{h,B}^{n+\theta,k+1} \right)_h = L_u^{n+\theta}(\mathbf{v}_h)
\end{aligned}
\tag{4.6.1}
$$

$$
b_u(q_h, \mathbf{u}_h^{n+1,k+1}) + \tau_1^{n+\theta,k} \left(\frac{1}{\rho_r} \nabla q_h, \mathbf{R}_{h,u}^{n+\theta,k+1} \right)_h \tag{4.6.2}
$$

$$
\begin{aligned}
(\delta_t \mathbf{B}_h^{n,k+1}, \mathbf{C}_h) &+ A_{Bu}(\mathbf{u}_h^{n+\theta,k+1}, \mathbf{B}_h^{n+\theta,k}, \mathbf{C}_h) + A_{BB}(\mathbf{B}_h^{n+\theta,k+1}, \mathbf{C}_h) \\
&+ b_B(r_h^{n+1,k+1}, \mathbf{C}_h) \\
&+ \tau_1^{n+\theta,k} \left(-\frac{1}{\mu_m \rho_r} (\nabla \times \mathbf{C}_h) \times \mathbf{B}_h^{n+\theta,k}, \mathbf{R}_{h,u}^{n+\theta,k+1} \right)_h \\
&+ \tau_3^{n+\theta,k} \left(\frac{1}{\mu_m \sigma} \nabla \times (\nabla \times \mathbf{C}_h), \mathbf{R}_{h,B}^{n+\theta,k+1} \right)_h \\
&+ \tau_4^{n+\theta,k} \left(\nabla \cdot \mathbf{C}_h, R_{h,r}^{n+\theta,k+1} \right)_h = L_{B1}^{n+\theta}(\mathbf{C}_h)
\end{aligned}
\tag{4.6.3}
$$

$$
b_B(s_h, \mathbf{B}_h^{n+1,k+1}) + \tau_3^{n+\theta,k} \left(\nabla s_h, \mathbf{R}_{h,B}^{n+\theta,k+1} \right)_h = L_{B2}^{n+\theta}(s_h) \tag{4.6.4}
$$

$$
\begin{aligned}
(\delta_t \vartheta_h^{n,k+1}, \psi_h) &+ A_{\vartheta u,1}(\mathbf{u}_h^{n+\theta,e'(k)}, \vartheta_h^{n+\theta,k+1}, \psi_h) + A_{\vartheta\vartheta}(\vartheta_h^{n+\theta,k+1}, \psi_h) \\
&\tau_5^{n+\theta,k} \left(\mathbf{u}_h^{n+\theta,k} \cdot \nabla \psi_h + \frac{k_t}{\rho_r c_p} \Delta \psi_h, R_{h,\vartheta}^{n+\theta,k+1} \right)_h = L_T^{n+\theta,k}(\psi_h)
\end{aligned}
\tag{4.6.5}
$$

where the *residuals* have been introduced:

$$
\begin{aligned}
\mathbf{R}_{h,u} &:= \delta_t \mathbf{u}_h + \mathbf{a} \cdot \nabla \mathbf{u}_h - \nu \Delta \mathbf{u}_h + \frac{1}{\rho_r} \nabla p_h - \frac{1}{\mu_m \rho_r} (\nabla \times \mathbf{B}_h) \times \mathbf{b} + \mathbf{g} \beta \vartheta_h - \mathbf{f}_f \\
R_{h,p} &:= \nabla \cdot \mathbf{u}_h \\
\mathbf{R}_{h,B} &:= \delta_t \mathbf{B}_h + \frac{1}{\mu_m \sigma} \nabla \times (\nabla \times \mathbf{B}_h) - \nabla \times (\mathbf{u}_h \times \mathbf{b}) + \nabla r_h - \mathbf{f}_m \\
R_{h,r} &:= \nabla \cdot \mathbf{B}_h \\
R_{h,\vartheta} &:= \delta_t \vartheta_h + \mathbf{a} \cdot \nabla \vartheta_h - \frac{k_t}{\rho_r c_p} \Delta \vartheta_h - Q_{tot}
\end{aligned}
$$

The superscript $n+\theta, k+1$ in (4.6.1)-(4.6.5) denotes that these residuals are evaluated with $\mathbf{u}_h$, p_h, $\mathbf{B}_h$, r_h and ϑ_h at this time step and iteration counter, whereas now $\mathbf{a} \equiv \mathbf{u}_h^{n+\theta,k}$ and $\mathbf{b} \equiv \mathbf{B}_h^{n+\theta,k}$.

The stabilization parameters $\tau_i, \quad i = 1, 2, 3, 4$ are given in (4.5.21)-(4.5.24), whereas

$$\tau_5 = \left(c_1 \frac{a}{h} + c_2 \frac{k_t}{\rho_r c_p h^2} \right)^{-1} \tag{4.6.6}$$

Note that the thermal coupling effect has been neglected in the design of the stabilization terms.

4.7 Programming Notes

In order to have the final numerical scheme (4.6.1)-(4.6.5) implemented, the CDR module of *ZEPHYR*[1] was used. The CDR module allows to implement finite element schemes of any system of partial differential equations that can be expressed in a Convection Diffusion Reaction form. A nonlinear system of convection-diffusion-reaction equations has the form presented in equation (4.4.16). Basically the CDR module works performing a do loop over the elements as is shown in algorithm (1).

Algorithm 1 Basic Algorithm of the CDR module

```
1:  for ielem = 0 to nelem do
2:    for igaus = 1 to ngaus do
3:      Calculate Cartesian derivatives and Jacobian
4:      Calculate the CDR matrices and the τ terms
5:      Calculate contribution from Galerkin terms
6:      Calculate the perturbation from the Galerkin test functions
7:      Calculate the residual within each element
8:      Multiply test functions by residuals
9:      Add Gauss point contribution
10:   end for
11:   if nboun > 0 then
12:     for iboun = 0 to nboun do
13:       Compute boundary matrix and RHS for the CDR equations
14:       Modify the element stiffness matrix to impose Dirichlet boundary
          conditions
15:       Assembly the RHS
16:       Assembly the matrix for the CDR equation.
17:     end for
18:   end if
19:   Solve the algebraic system
20: end for
```

[1] *ZEPHYR* is an in house finite element code developed at Prof. R. Codina's research group

In algorithm (1) *nelem* is the number of elements in the finite element mesh, *ngaus* is the number of Gauss points for the particular type of element used and *nboun* is the number of Dirichlet boundaries.

In order to implement the numerical scheme presented in algorithm 1 explicit expressions for the CDR matrices must be used. The convective matrices $\mathbf{A}_i$, diffusion matrices $\mathbf{K}_{ij}$ and the reaction vector $\mathbf{S}$ are presented next. For $d = 3$ there are three convective matrices $\mathbf{A}_1$, $\mathbf{A}_2$ and $\mathbf{A}_3$ and nine difussive matrices $\mathbf{K}_{11}$, $\mathbf{K}_{12}$, $\mathbf{K}_{13}$, $\mathbf{K}_{21}$, $\mathbf{K}_{22}$, $\mathbf{K}_{23}$, $\mathbf{K}_{31}$, $\mathbf{K}_{32}$ and $\mathbf{K}_{33}$. Finally there is a reaction matrix $\mathbf{S}$.

Explicit expressions for these matrices are given next:

$$\mathbf{A}_1 = \begin{bmatrix} a_1 & 0 & 0 & \frac{1}{\rho_r} & 0 & \frac{b_2}{\mu_m \rho_r} & \frac{b_3}{\mu_m \rho_r} & 0 & 0 \\ 0 & a_1 & 0 & 0 & 0 & -\frac{b_1}{\mu_m \rho_r} & 0 & 0 & 0 \\ 0 & 0 & a_1 & 0 & 0 & 0 & \frac{b_1}{\mu_m \rho_r} & 0 & 0 \\ 1 & 0 & 0 & 0 & 0 & 0 & 0 & 0 & 0 \\ 0 & 0 & 0 & 0 & 0 & 0 & 0 & 1 & 0 \\ b_2 & -b_1 & 0 & 0 & 0 & 0 & 0 & 0 & 0 \\ b_3 & 0 & -b_1 & 0 & 0 & 0 & 0 & 0 & 0 \\ 0 & 0 & 0 & 0 & 1 & 0 & 0 & 0 & 0 \\ 0 & 0 & 0 & 0 & 0 & 0 & 0 & 0 & -a_1 \rho_r c_p \end{bmatrix} \tag{4.7.1}$$

$$\mathbf{A}_2 = \begin{bmatrix} a_2 & 0 & 0 & 0 & -\frac{b_2}{\mu_m \rho_r} & 0 & 0 & 0 & 0 \\ 0 & a_2 & 0 & \frac{1}{\rho_r} & \frac{b_1}{\mu_m \rho_r} & 0 & \frac{b_3}{\mu_m \rho_r} & 0 & 0 \\ 0 & 0 & a_2 & 0 & 0 & 0 & -\frac{b_2}{\mu_m \rho_r} & 0 & 0 \\ 0 & 1 & 0 & 0 & 0 & 0 & 0 & 0 & 0 \\ -b_2 & b_1 & 0 & 0 & 0 & 0 & 0 & 0 & 0 \\ 0 & 0 & 0 & 0 & 0 & 0 & 0 & 1 & 0 \\ 0 & b_3 & -b_2 & 0 & 0 & 0 & 0 & 0 & 0 \\ 0 & 0 & 0 & 0 & 0 & 1 & 0 & 0 & 0 \\ 0 & 0 & 0 & 0 & 0 & 0 & 0 & 0 & -a_2 \rho_r c_p \end{bmatrix} \tag{4.7.2}$$

$$\mathbf{A}_3 = \begin{bmatrix} a_3 & 0 & 0 & 0 & -\frac{b_3}{\mu_m \rho_r} & 0 & 0 & 0 & 0 \\ 0 & a_3 & 0 & 0 & 0 & -\frac{b_3}{\mu_m \rho_r} & 0 & 0 & 0 \\ 0 & 0 & a_3 & \frac{1}{\rho_r} & \frac{b_1}{\mu_m \rho_r} & \frac{b_2}{\mu_m \rho_r} & 0 & 0 & 0 \\ 0 & 0 & 1 & 0 & 0 & 0 & 0 & 0 & 0 \\ -b_3 & 0 & b_1 & 0 & 0 & 0 & 0 & 0 & 0 \\ 0 & -b_3 & b_2 & 0 & 0 & 0 & 0 & 0 & 0 \\ 0 & 0 & 0 & 0 & 0 & 0 & 0 & 1 & 0 \\ 0 & 0 & 0 & 0 & 0 & 0 & 1 & 0 & 0 \\ 0 & 0 & 0 & 0 & 0 & 0 & 0 & 0 & -a_3 \rho_r c_p \end{bmatrix} \tag{4.7.3}$$

$$\mathbf{K}_{11} = \begin{bmatrix} \nu & 0 & 0 & 0 & 0 & 0 & 0 & 0 & 0 \\ 0 & \nu & 0 & 0 & 0 & 0 & 0 & 0 & 0 \\ 0 & 0 & \nu & 0 & 0 & 0 & 0 & 0 & 0 \\ 0 & 0 & 0 & 0 & 0 & 0 & 0 & 0 & 0 \\ 0 & 0 & 0 & 0 & 0 & 0 & 0 & 0 & 0 \\ 0 & 0 & 0 & 0 & 0 & \frac{1}{\mu_m \sigma} & 0 & 0 & 0 \\ 0 & 0 & 0 & 0 & 0 & 0 & \frac{1}{\mu_m \sigma} & 0 & 0 \\ 0 & 0 & 0 & 0 & 0 & 0 & 0 & 0 & 0 \\ 0 & 0 & 0 & 0 & 0 & 0 & 0 & 0 & k_t \end{bmatrix} \tag{4.7.4}$$

$$\mathbf{K}_{12} = \begin{bmatrix} 0 & 0 & 0 & 0 & 0 & 0 & 0 & 0 & 0 \\ 0 & 0 & 0 & 0 & 0 & 0 & 0 & 0 & 0 \\ 0 & 0 & 0 & 0 & 0 & 0 & 0 & 0 & 0 \\ 0 & 0 & 0 & 0 & 0 & 0 & 0 & 0 & 0 \\ 0 & 0 & 0 & 0 & 0 & 0 & 0 & 0 & 0 \\ 0 & 0 & 0 & 0 & -\frac{1}{\mu_m \sigma} & 0 & 0 & 0 & 0 \\ 0 & 0 & 0 & 0 & 0 & 0 & 0 & 0 & 0 \\ 0 & 0 & 0 & 0 & 0 & 0 & 0 & 0 & 0 \\ 0 & 0 & 0 & 0 & 0 & 0 & 0 & 0 & 0 \end{bmatrix} \tag{4.7.5}$$

$$\mathbf{K}_{13} = \begin{bmatrix} 0 & 0 & 0 & 0 & 0 & 0 & 0 & 0 & 0 \\ 0 & 0 & 0 & 0 & 0 & 0 & 0 & 0 & 0 \\ 0 & 0 & 0 & 0 & 0 & 0 & 0 & 0 & 0 \\ 0 & 0 & 0 & 0 & 0 & 0 & 0 & 0 & 0 \\ 0 & 0 & 0 & 0 & 0 & 0 & 0 & 0 & 0 \\ 0 & 0 & 0 & 0 & 0 & 0 & 0 & 0 & 0 \\ 0 & 0 & 0 & 0 & -\frac{1}{\mu_m \sigma} & 0 & 0 & 0 & 0 \\ 0 & 0 & 0 & 0 & 0 & 0 & 0 & 0 & 0 \\ 0 & 0 & 0 & 0 & 0 & 0 & 0 & 0 & 0 \end{bmatrix} \tag{4.7.6}$$

$$\mathbf{K}_{21} = \begin{bmatrix} 0 & 0 & 0 & 0 & 0 & 0 & 0 & 0 & 0 \\ 0 & 0 & 0 & 0 & 0 & 0 & 0 & 0 & 0 \\ 0 & 0 & 0 & 0 & 0 & 0 & 0 & 0 & 0 \\ 0 & 0 & 0 & 0 & 0 & 0 & 0 & 0 & 0 \\ 0 & 0 & 0 & 0 & 0 & -\frac{1}{\mu_m \sigma} & 0 & 0 & 0 \\ 0 & 0 & 0 & 0 & 0 & 0 & 0 & 0 & 0 \\ 0 & 0 & 0 & 0 & 0 & 0 & 0 & 0 & 0 \\ 0 & 0 & 0 & 0 & 0 & 0 & 0 & 0 & 0 \\ 0 & 0 & 0 & 0 & 0 & 0 & 0 & 0 & 0 \end{bmatrix} \tag{4.7.7}$$

$$\mathbf{K}_{22} = \begin{bmatrix} \nu & 0 & 0 & 0 & 0 & 0 & 0 & 0 & 0 \\ 0 & \nu & 0 & 0 & 0 & 0 & 0 & 0 & 0 \\ 0 & 0 & \nu & 0 & 0 & 0 & 0 & 0 & 0 \\ 0 & 0 & 0 & 0 & 0 & 0 & 0 & 0 & 0 \\ 0 & 0 & 0 & 0 & \frac{1}{\mu_m \sigma} & 0 & 0 & 0 & 0 \\ 0 & 0 & 0 & 0 & 0 & 0 & 0 & 0 & 0 \\ 0 & 0 & 0 & 0 & 0 & 0 & \frac{1}{\mu_m \sigma} & 0 & 0 \\ 0 & 0 & 0 & 0 & 0 & 0 & 0 & 0 & 0 \\ 0 & 0 & 0 & 0 & 0 & 0 & 0 & 0 & k_t \end{bmatrix} \tag{4.7.8}$$

$$\mathbf{K}_{23} = \begin{bmatrix} 0 & 0 & 0 & 0 & 0 & 0 & 0 & 0 & 0 \\ 0 & 0 & 0 & 0 & 0 & 0 & 0 & 0 & 0 \\ 0 & 0 & 0 & 0 & 0 & 0 & 0 & 0 & 0 \\ 0 & 0 & 0 & 0 & 0 & 0 & 0 & 0 & 0 \\ 0 & 0 & 0 & 0 & 0 & 0 & 0 & 0 & 0 \\ 0 & 0 & 0 & 0 & 0 & 0 & 0 & 0 & 0 \\ 0 & 0 & 0 & 0 & 0 & -\frac{1}{\mu_m \sigma} & 0 & 0 & 0 \\ 0 & 0 & 0 & 0 & 0 & 0 & 0 & 0 & 0 \\ 0 & 0 & 0 & 0 & 0 & 0 & 0 & 0 & 0 \end{bmatrix} \tag{4.7.9}$$

$$\mathbf{K}_{31} = \begin{bmatrix} 0 & 0 & 0 & 0 & 0 & 0 & 0 & 0 & 0 \\ 0 & 0 & 0 & 0 & 0 & 0 & 0 & 0 & 0 \\ 0 & 0 & 0 & 0 & 0 & 0 & 0 & 0 & 0 \\ 0 & 0 & 0 & 0 & 0 & 0 & 0 & 0 & 0 \\ 0 & 0 & 0 & 0 & 0 & 0 & -\frac{1}{\mu_m \sigma} & 0 & 0 \\ 0 & 0 & 0 & 0 & 0 & 0 & 0 & 0 & 0 \\ 0 & 0 & 0 & 0 & 0 & 0 & 0 & 0 & 0 \\ 0 & 0 & 0 & 0 & 0 & 0 & 0 & 0 & 0 \\ 0 & 0 & 0 & 0 & 0 & 0 & 0 & 0 & 0 \end{bmatrix} \tag{4.7.10}$$

$$\mathbf{K}_{32} = \begin{bmatrix} 0 & 0 & 0 & 0 & 0 & 0 & 0 & 0 & 0 \\ 0 & 0 & 0 & 0 & 0 & 0 & 0 & 0 & 0 \\ 0 & 0 & 0 & 0 & 0 & 0 & 0 & 0 & 0 \\ 0 & 0 & 0 & 0 & 0 & 0 & 0 & 0 & 0 \\ 0 & 0 & 0 & 0 & 0 & 0 & 0 & 0 & 0 \\ 0 & 0 & 0 & 0 & 0 & 0 & -\frac{1}{\mu_m \sigma} & 0 & 0 \\ 0 & 0 & 0 & 0 & 0 & 0 & 0 & 0 & 0 \\ 0 & 0 & 0 & 0 & 0 & 0 & 0 & 0 & 0 \\ 0 & 0 & 0 & 0 & 0 & 0 & 0 & 0 & 0 \end{bmatrix} \tag{4.7.11}$$

$$\mathbf{K}_{33} = \begin{bmatrix} \nu & 0 & 0 & 0 & 0 & 0 & 0 & 0 & 0 \\ 0 & \nu & 0 & 0 & 0 & 0 & 0 & 0 & 0 \\ 0 & 0 & \nu & 0 & 0 & 0 & 0 & 0 & 0 \\ 0 & 0 & 0 & 0 & 0 & 0 & 0 & 0 & 0 \\ 0 & 0 & 0 & 0 & \frac{1}{\mu_m \sigma} & 0 & 0 & 0 & 0 \\ 0 & 0 & 0 & 0 & 0 & \frac{1}{\mu_m \sigma} & 0 & 0 & 0 \\ 0 & 0 & 0 & 0 & 0 & 0 & 0 & 0 & 0 \\ 0 & 0 & 0 & 0 & 0 & 0 & 0 & 0 & 0 \\ 0 & 0 & 0 & 0 & 0 & 0 & 0 & 0 & k_t \end{bmatrix} \tag{4.7.12}$$

$$\mathbf{S} = \begin{bmatrix} 0 & 0 & 0 & 0 & 0 & 0 & 0 & 0 & g_x\beta \\ 0 & 0 & 0 & 0 & 0 & 0 & 0 & 0 & g_y\beta \\ 0 & 0 & 0 & 0 & 0 & 0 & 0 & 0 & g_z\beta \\ 0 & 0 & 0 & 0 & 0 & 0 & 0 & 0 & 0 \\ 0 & 0 & 0 & 0 & 0 & 0 & 0 & 0 & 0 \\ 0 & 0 & 0 & 0 & 0 & 0 & 0 & 0 & 0 \\ 0 & 0 & 0 & 0 & 0 & 0 & 0 & 0 & 0 \\ 0 & 0 & 0 & 0 & 0 & 0 & 0 & 0 & 0 \\ 0 & 0 & 0 & 0 & 0 & 0 & 0 & 0 & 0 \end{bmatrix} \tag{4.7.13}$$

It is necessary to mention that, for the matrix **S**, the terms arising from the linearization of the Joule effect have not been considered. Basically the CDR matrices are used to calculate the contributions to Galerkin term from advective, diffusive and reactive terms. Following algorithm (1) provides the method to solve an steady problem (time independent), but the real nature of the MHD phenomena involve evolutive (time dependent) problems.

In order to have an adequate temporal discretization for the MHD problem the following algorithm was implemented:

Algorithm 2 Algorithm for the time discretization

1: **while** $ctime <= timef - epsilon$ and $istep >= nsmax$ **do**
2: Computes the time step
3: Update boundary conditions
4: Get an initial guess for the unknown
5: Solve the internal problem for CDR equations
6: Checks the general convergence of the run
7: Close the time step
8: **end while**

Algorithm (2) shows the basic steps that must be taken in order to perform a time discretization for the CDR equations. In this algorithm (2) *ctime* is the current time, $timef$ is the final time, *epsilon* is a tolerance for the time and *nsmax* is the maximum number of steps. The time step used in algorithm (2) is calculated using θ–scheme.

4.8 Convergence Test

In order to analyze the convergence properties of the stabilized finite element approximation presented, a two dimensional problem in the square domain $\Omega =]0,1[\times]0,1[$ is considered. This problem possesses a closed form analytical solution. The components of the body forces $\mathbf{f_u} = \left(f_{u_x}, f_{u_y}\right)$ and $\mathbf{f_b} = \left(f_{b_x}, f_{b_y}\right)$ are prescribed as:

$$\begin{aligned}
f_{u_x} &= f_1(x)\left(d'_1(y)\right)^2 f'_1(x) \\
&- f'_1(x) d_1(y) f_1(x) d''_1(y) \\
&- \frac{1}{Re}\left[f''_1(x) d'_1(y) + f_1(x) d'''_1(y)\right] \\
&+ S\left[f'_2(x) d_2(y)\left(f''_2(x) d_2(y) + f_2(x) d''_2(y)\right)\right] \\
f_{u_y} &= -f_1(x) d'_1(y) f''_1(x) d_1(y) \\
&+ \left(f'_1(x)\right)^2 d_1(y) d'_1(y) \\
&+ \frac{1}{Re}\left[d_1(y) f'''_1(x) + d''_1(y) f'_1(x)\right] \\
&+ S\left[f_2(x) d'_2(y)\left(f''_2(x) d_2(y) + f_2(x) d''_2(y)\right)\right]
\end{aligned}$$

$$\begin{aligned}
f_{b_x} &= f_1(x) f'_2(x)\left[d''_1(y) d_2(y) + d'_1(y) d'_2(y)\right] \\
&- f'_1(x) f_2(x)\left[d'_1(y) d'_2(y) + d_1(y) d''_2(y)\right] \\
&- \frac{1}{Rm}\left[f''_2(x) d'''_2(y) + f_2(x) d_2(y)\right] \\
f_{b_y} &= -d'_1(y) d_2(y)\left[f'_1(x) f'_2(x) + f_1(x) f''_2(x)\right] \\
&- d_1(y) d'_2(y)\left[f''_1(x) f_2(x) + f'_1(x) f'_2(x)\right] \\
&+ \frac{1}{Rm}\left[f'''_2(x) d_2(y) + f'_2(x) d''_2(y)\right]
\end{aligned}$$

where the prime denotes differentiation. Note that in this example we use the dimensionless numbers Re, Rm and S to characterize the problem. Endowed with this body forces the 2D problem has an exact solution for the velocity given by $\mathbf{u} = (u_x, u_y)$ where:

$$\begin{aligned}
u_x(x,y) &:= f_1(x) d'_1(y) \\
u_y(x,y) &:= -f'_1(x) d_1(y)
\end{aligned}$$

The analytical solution for the magnetic field is $\mathbf{B} = (B_x, B_y)$ now with:

$$\begin{aligned}
B_x(x,y) &:= f_2(x) d'_2(y) \\
B_y(x,y) &:= -f'_2(x) d_2(y).
\end{aligned}$$

In this particular example, the functions $f_1(x), f_2(x), d_1(y)$ and $d_2(y)$ are chosen as:

$$
\begin{aligned}
f_1(x) &= x^2(1-x)^2 \\
f_2(x) &= x^2(1-x)^2 \\
d_1(y) &= y^2(1-y)^2 \\
d_2(y) &= y^2(1-y)^2
\end{aligned}
$$

The square domain Ω has been discretized with five different uniform meshes of $2 \times 25 \times 25$,$2 \times 50 \times 50$,$2 \times 75 \times 75$,$2 \times 100 \times 100$ and $2 \times 125 \times 125$ triangular linear elements. The characteristic length of the meshes are $h = 1/25, 1/50, 1/75, 1/100$ and $1/125$.

The convergence plots measured in the discrete $L^2(\Omega)$–norm for the velocity and the magnetic field are shown in figures 4.1 and 4.2 respectively. The slope of the convergence curve has to be compared with the line of slope two also shown in the figures. It is observed that the numerical convergence has also approximately slope two (1.93 for the velocity and 2.03 for the magnetic field), which is optimal for the linear elements employed in the calculation.

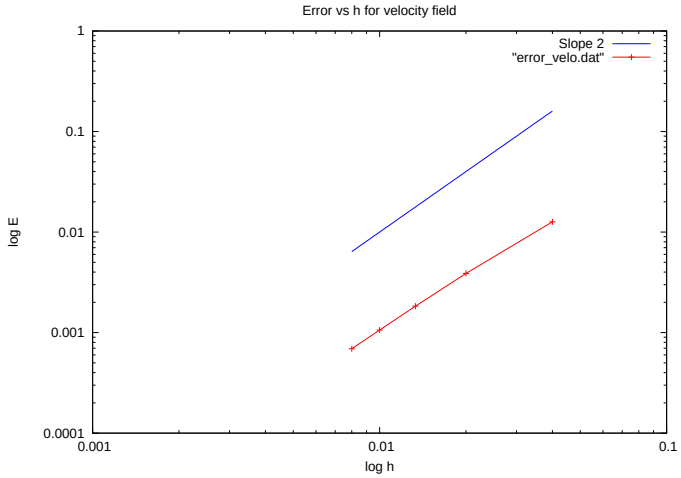

Figure 4.1 *Velocity field error versus element size*

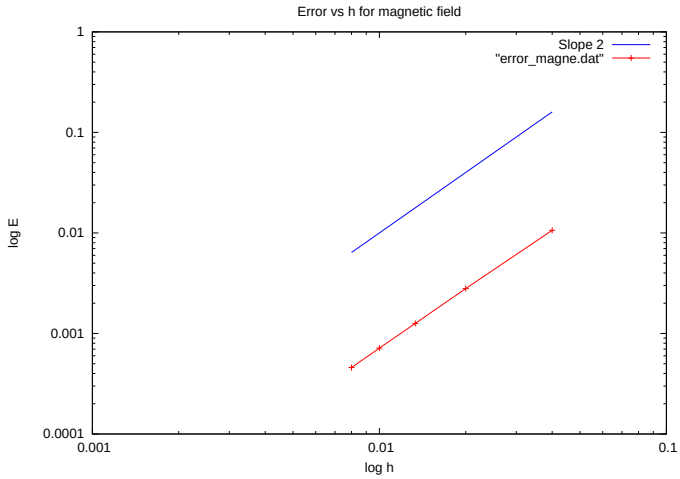

Figure 4.2 *Magnetic field error versus element size*

Chapter 5

Numerical Simulations

The numerical simulations, performed while this research was developed, are presented in this chapter. Five numerical simulations were performed. The first numerical simulation presented is the Hartmann flow. This flow was chosen because it can be used to check the accuracy of the numerical scheme. The flow over a step is the second numerical simulation presented. In this numerical simulation the qualitative behavior of the vorticity is analyzed. The third numerical simulation presented is the flow past a circular cylinder. This simulation is time dependent and allows the analysis of the temporal behavior of the numerical scheme. The fourth numerical simulation is the clogging in continuous casting of steel. This simulation is also time dependent and it applies the numerical scheme in a simplified industrial case. The final numerical simulation is a Czochralski crystal growth process. This simulation is also an application of the numerical scheme to a simplified industrial case, which presents thermal coupling and therefore convection movements in the fluid are present.

5.1 Hartmann Flow

The Hartmann flow is the simplest of all incompressible MHD flows. Due to its simplicity it is a really practical benchmark for the numerical scheme developed in this research. The general characteristics of the Hartmann flow were briefly discussed in section 3.6. In that section the boundary conditions (3.6.2), (3.6.3) and the solutions for the velocity and the magnetic field, (3.6.4), (3.6.5), (3.6.6) and (3.6.7) were presented. Those boundary conditions and solutions were used to build a benchmark, whose results are presented in this section.

In order to implement the numerical benchmark, first a rectangular domain was built using *GiD*,[1] and the boundary conditions were imposed over that domain. Figure 5.1 shows schematically the domain and the boundary conditions.

The boundary conditions over the domain consist of non slip boundary conditions on the walls and imposed parabolic profile at the inlet and the outlet for

[1] *GiD* is a pre and post process software developed at CIMNE

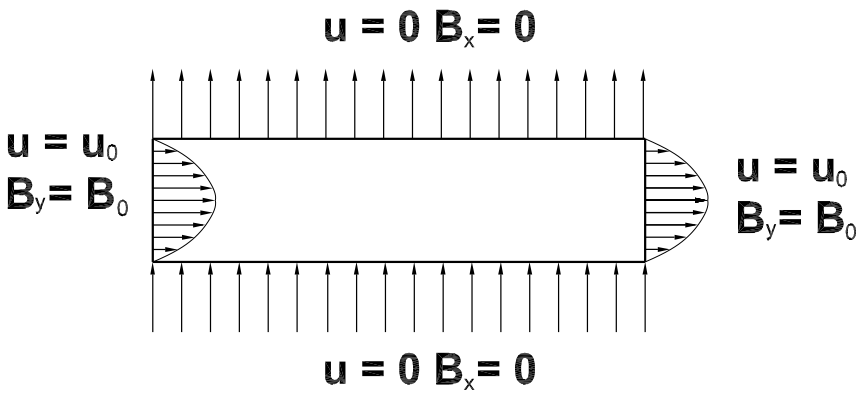

Figure 5.1 *Boundary Conditions for Hartmann flow*

the velocity. In the case of the magnetic field, the boundary conditions over the domain consist of an imposed normal component of the magnetic field on the walls and an imposed tangential component at the inlet and the outlet. The variable r is set to $r = 0$ over the whole boundary. The rectangular domain used for this simulation was meshed using *GiD*. Four different meshes were build using linear triangular elements. The number of elements and nodes for the four meshes used are presented in the table 5.1. Mesh number 1 is shown in figure 5.2.

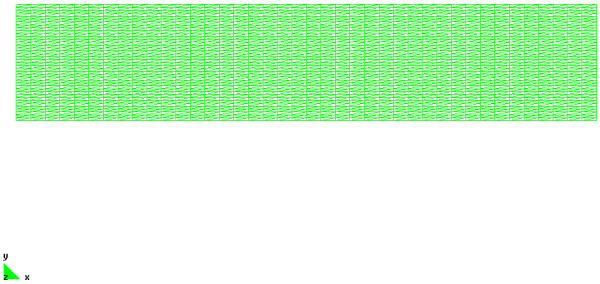

Figure 5.2 *Uniform Mesh used for Hartmann flow*

The fact that there can be two different cases for the magnetic field profile was presented in section 3.6. The first case takes place when insulating walls are employed and the second case takes place when conducting walls are used. Therefore the numerical simulations for Hartmann flow cover these two situations.

The objective of this numerical simulation in both cases is to observe the change in the velocity profile while the intensity of the magnetic field is increased. In order to appreciate the effects of the increasing magnetic coupling over the velocity profile the simulations were performed for the following Hartmann numbers: $Ha =$

Mesh	Elements	Nodes
1	3200	1681
2	6400	3321
3	12800	6601
4	25600	13161

Table 5.1 *Number of Elements and Nodes for Uniform Meshes*

$0.0, 5.0, 10.0$. The effect of increasing the Hartmann number over the velocity is to flat the velocity profile. In other words the effect of the magnetic field tends to homogenize the velocity of the fluid along the y axis.

Although four different meshes were used, only results for mesh number 2 are presented. This is done in order to keep the presentation as simple as possible and not to overwhelm the reader with several graphics. Also, it is worth of remark that, although the simulations were performed over a complete rectangular domain, it is better for visualization purposes, to use a cut on the domain in order to clearly see the profiles of velocity and magnetic field in their x–component.

Figures 5.3 to 5.8 show the velocity and magnetic profiles for mesh 2 and for the cases of $Ha = 0.0, 5.0, 10.0$. These figures belong to the insulating walls case. In figure 5.3 the velocity profile for $Ha = 0.0$ is shown. As can be seen, there is no effect over the profile because there is no magnetic field. The lack of magnetic field for $Ha = 0.0$ can be seen in figure 5.4. Figure 5.5 shows the velocity profile for $Ha = 5.0$. In this case, it can be seen a clear flattening of the profile, contrary to $Ha = 0.0$, because now there is a magnetic field as can be seen in figure 5.6. This flattening effect is further increased for $Ha = 10.0$. The numerical solutions obtained in the case of isolating walls in the Hartmann flow match the analytical solutions provided by (3.6.4), (3.6.5).

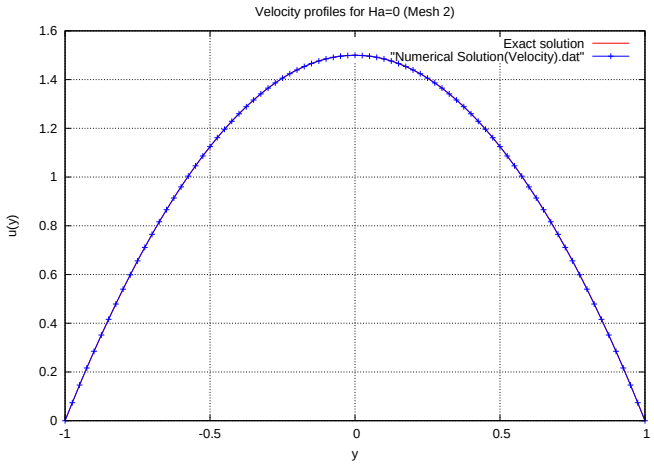

Figure 5.3 *Velocity Profile for Ha=0 and Mesh 2, Insulating Walls*

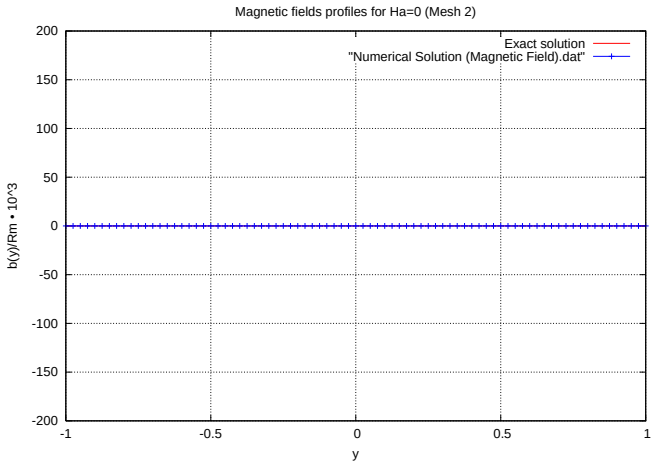

Figure 5.4 *Magnetic Profile for Ha=0 and Mesh 2, Insulating Walls*

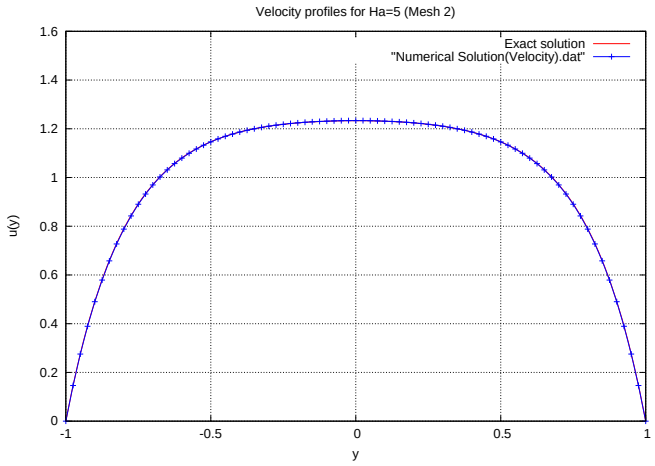

Figure 5.5 *Velocity Profile for Ha=5 and Mesh 2, Insulating Walls*

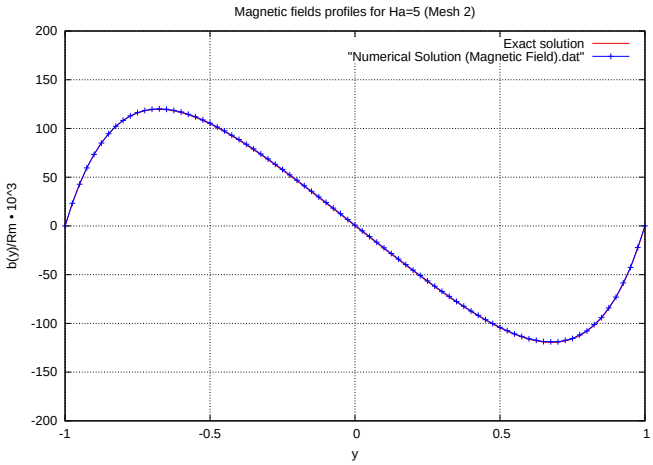

Figure 5.6 *Magnetic Profile for Ha=5 and Mesh 2, Insulating Walls*

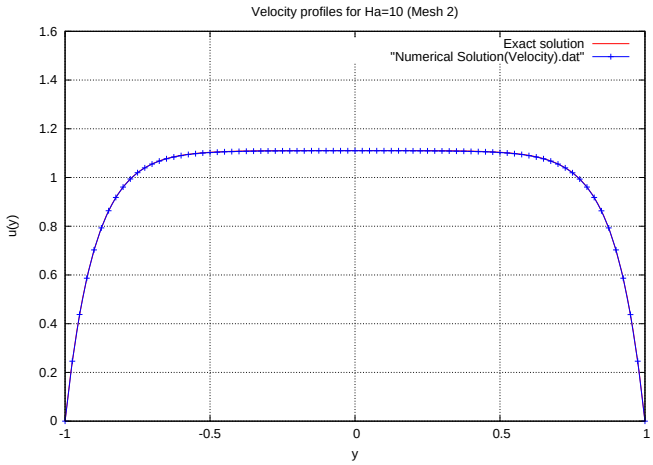

Figure 5.7 *Velocity Profile for Ha=10 and Mesh 2, Insulating Walls*

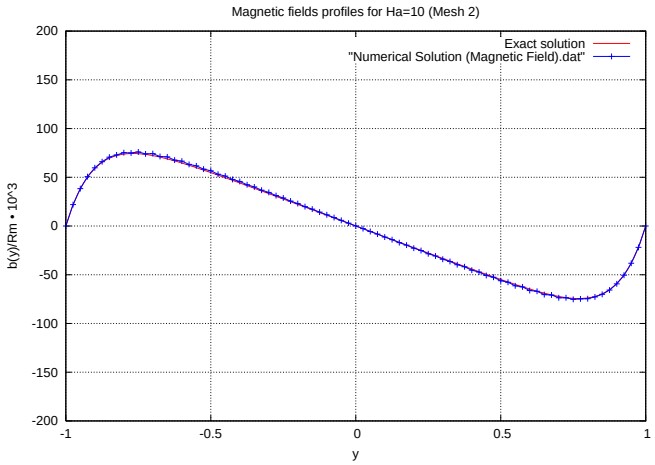

Figure 5.8 *Magnetic Profile for Ha=10 and Mesh 2, Insulating Walls*

In figures 5.9 to 5.13 the velocity and magnetic field profiles for the case of conducting walls in Hartman flow are presented. As in the previous case the Hartmann number takes the values of $Ha = 0.0, 5.0, 10.0$. The velocity profile takes the same values as in the case of isolating walls, but the magnetic profile is quite different, because the boundary condition for the magnetic field is imposed over its derivative. As in the previous case the general effect of the increase of the Hartmann number is to flat the velocity profile along the y axis. It is worth of mentioning the fact that the values of the induced magnetic field are really small, as can be seen in the figures. Although the induced magnetic field is small, it is still strong enough to modify the behavior of the fluid. In order to properly show the induced magnetic field in the figures, its value has been divided by the Reynolds Magnetic Rm, and multiplied by 1000.

As a final conclusion it can be said that the numerical benchmark, provided by the Hartmann flow, offers a good match between the numerical and the analytical solutions of the flow. This numerical simulations confirms the general behavior of MHD where the vorticity is killed by the magnetic field.

5.2 Flow Over a Step

This numerical simulation was originally proposed by Gerbeau in [21]. The objective is to model the flow of a fluid in a duct with a step while a magnetic field is imposed. The domain under study is shown in figure 5.14 together with the imposed boundary conditions.

The boundary conditions for the velocity consist of non slip condition in the walls of the duct and imposed profiles at the inlet and the outlet. In the case of the magnetic field the boundary conditions consist of imposed normal component for the magnetic field in the walls of the duct and tangential component imposed over

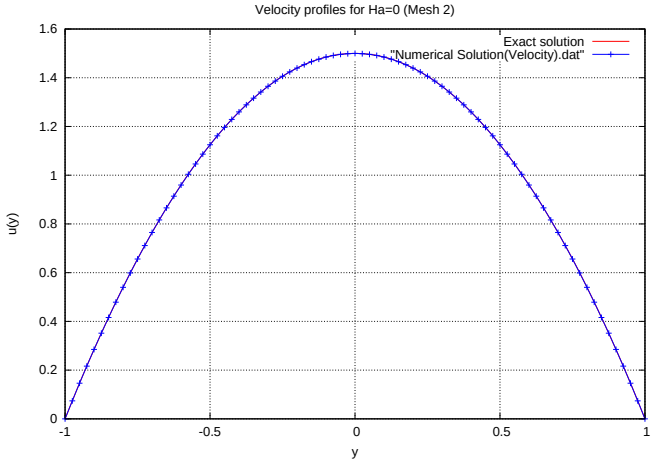

Figure 5.9 *Velocity Profile for Ha=0 and Mesh 2, Conducting Walls*

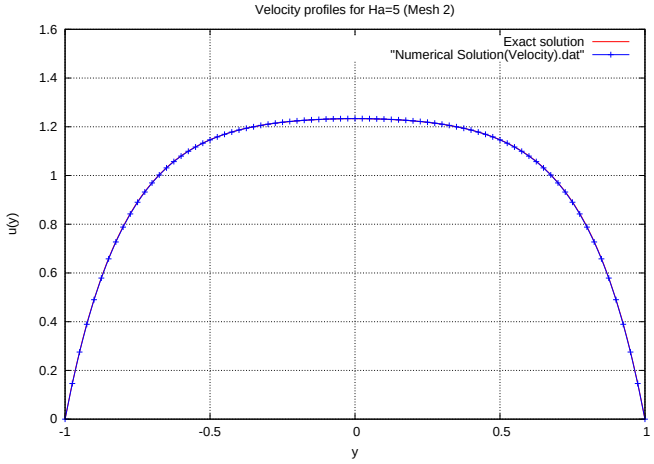

Figure 5.10 *Velocity Profile for Ha=5 and Mesh 2, Conducting Walls*

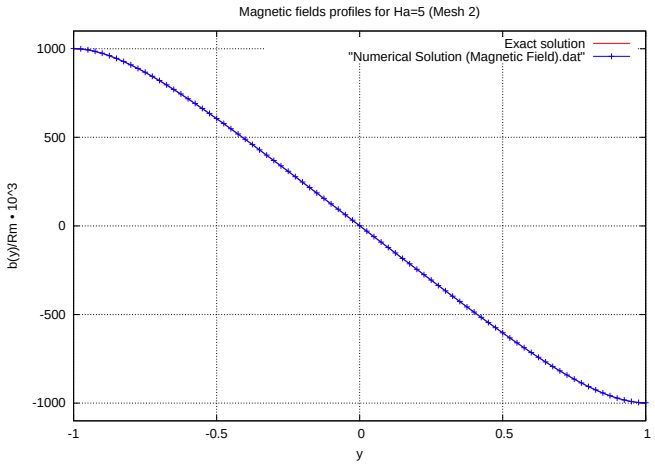

Figure 5.11 *Magnetic Profile for Ha=5 and Mesh 2, Conducting Walls*

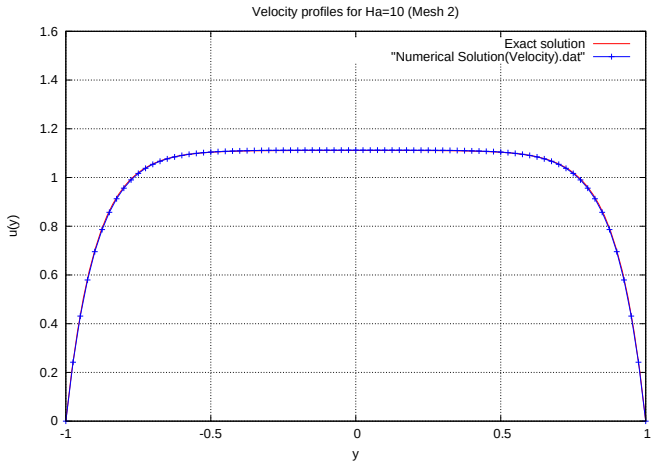

Figure 5.12 *Velocity Profile for Ha=10 and Mesh 2, Conducting Walls*

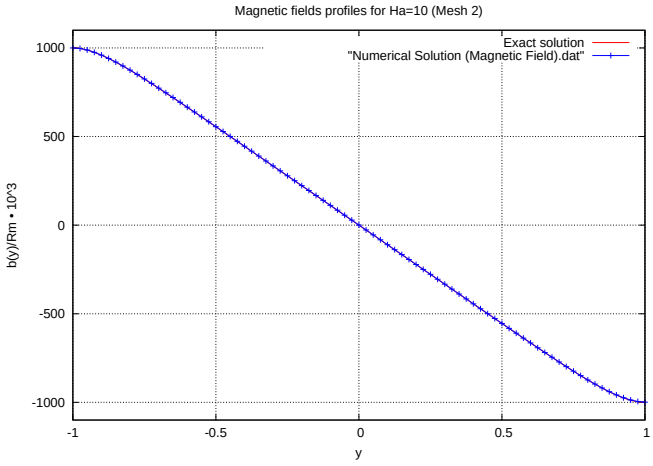

Figure 5.13 *Magnetic Profile for Ha=10 and Mesh 2, Conducting Walls*

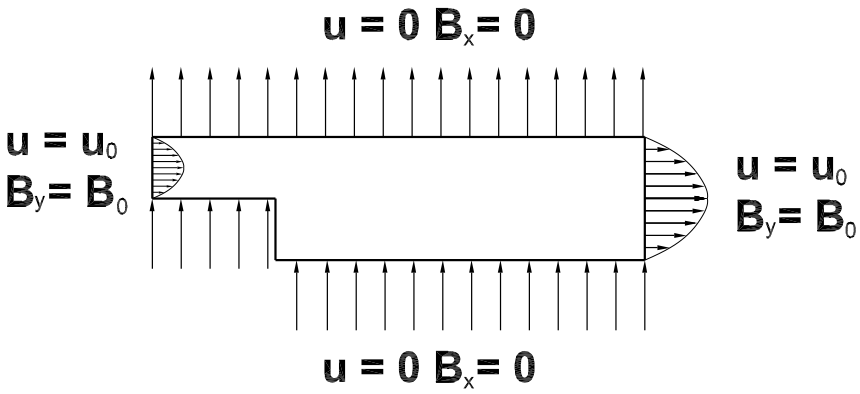

Figure 5.14 *Domain and boundary conditions for the flow over a step*

the magnetic field at the inlet and the outlet. Although the velocity profiles imposed at the inlet and the outlet should be Hartmann profiles the original Pouiseille profiles proposed by Gerbeau are used. The domain of this simulation is meshed using *GiD* and the mesh consists of 7771 linear triangular elements and 4029 nodes. This mesh is shown in the figure 5.15.

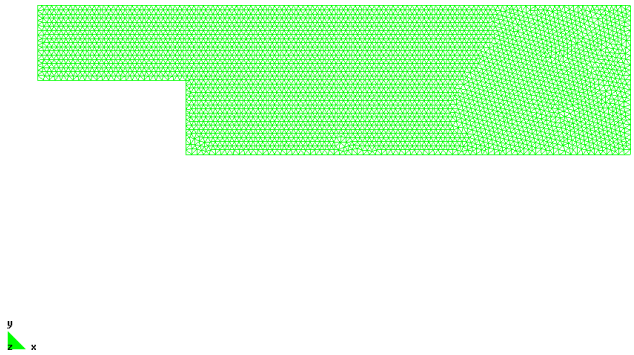

Figure 5.15 *Mesh used for the flow over a step*

The general effect to be observed is the vanishing of the whirlpool over the step and the uniformity of the flow when the magnetic field is applied. Figures 5.16 to 5.20 show the flow and how it is affected when the magnetic field is applied. These figures clearly show that the whirlpool vanishes while the intensity of the magnetic field is increased.

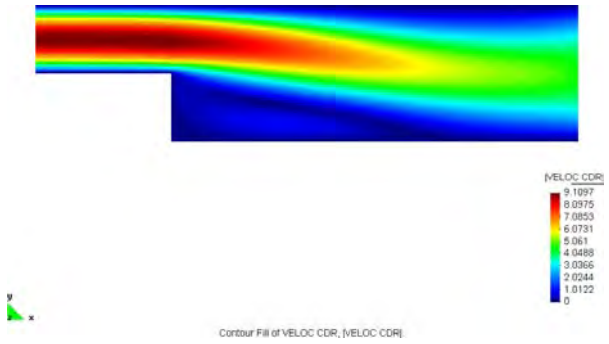

Figure 5.16 *Velocity in the Flow Over a Step for Ha=0*

As can be seen in figure 5.18 the flow stars to get uniform when the Hartmann number is equal to $Ha = 5.0$. This uniformity deepens as the Hartmann number increases. Figures 5.19 to 5.20 show how the flow finally gets very uniform when $Ha = 10.0$ and $Ha = 20.0$.

Special attention must be paid to the whirlpool over the step. Figures 5.21 to 5.23 show a zoom on the area immediately over the step. In order to clearly show

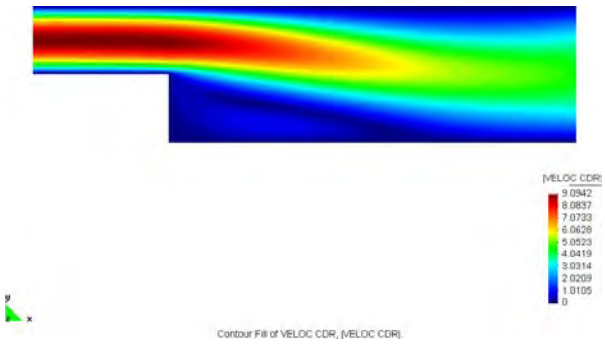

Figure 5.17 *Velocity in the Flow Over a Step for Ha=1*

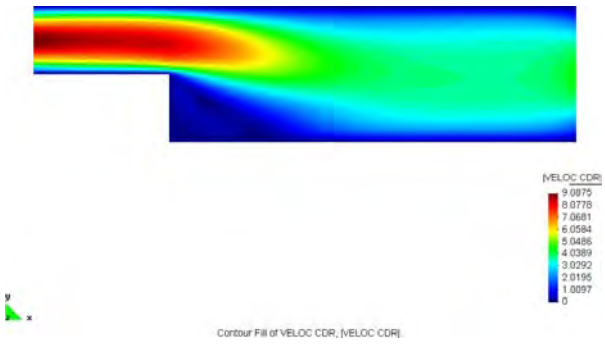

Figure 5.18 *Velocity in the Flow Over a Step for Ha=5*

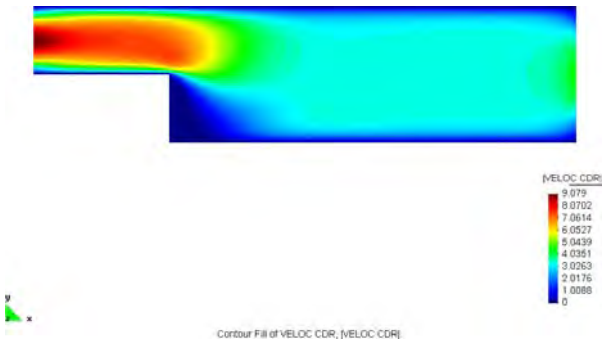

Figure 5.19 *Velocity in the Flow Over a Step for Ha=10*

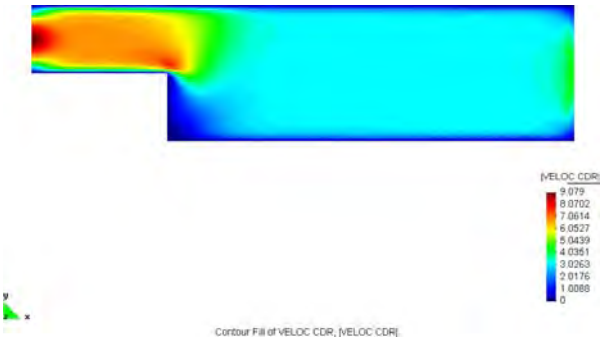

Figure 5.20 *Velocity in the Flow Over a Step for Ha=20*

the whirlpool over the step, the velocity is depicted using vectors. The figures show how the whirlpool is unaffected when the Hartmann number is $Ha = 0.0$. This situation shows little change for $Ha = 5.0$ because at this Hartmann number, recirculation is still present in the flow. When the intensity of the magnetic field is increased the recirculation will vanish as can be seen at $Ha = 10.0$ where the whirlpool is completely gone, but the flow is not completely uniform.

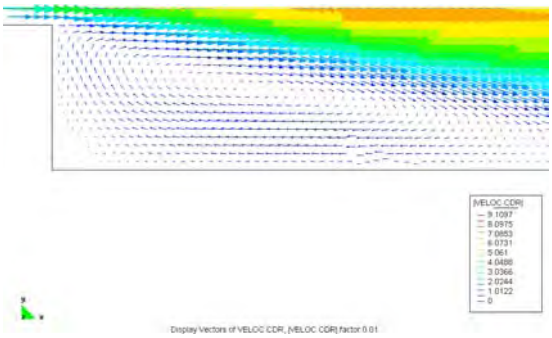

Figure 5.21 *Vortex over the step for Ha=0*

Figures 5.24 and 5.25 show how the recirculation vanishes under the influence of the magnetic field. The vortex over the step is no longer there and the flow is very uniform. This fact is explained because the magnetic field exerts forces over the fluid. Those forces act contrary to the movement of the fluid and the flow gets uniform. Although this is a pure academic example, it shows an important hallmark of MHD, the suppression of unwanted movements in the fluid. This characteristic of MHD is extensively used in industries where the fluids involved are electrical conductors.

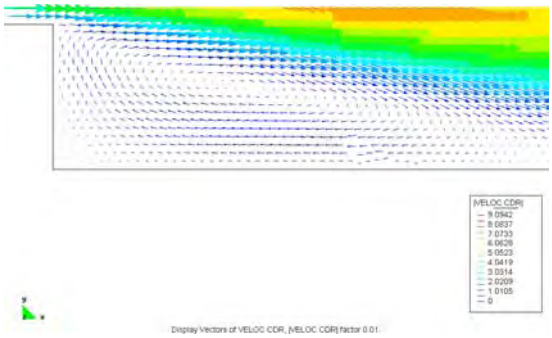

Figure 5.22 *Vortex over the step for Ha=1*

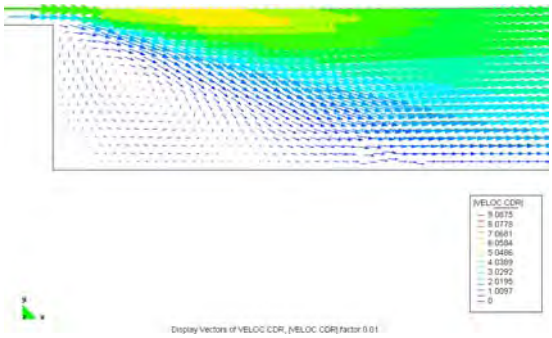

Figure 5.23 *Vortex over the step for Ha=5*

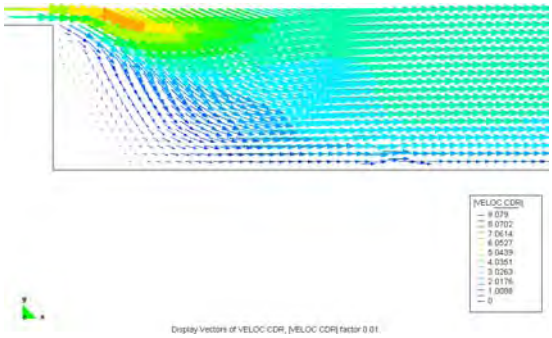

Figure 5.24 *Vorticity over the step for Ha=10*

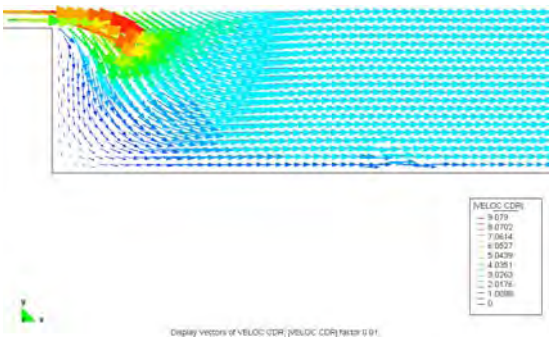

Figure 5.25 *Vorticity over the step for Ha=20*

Finally, figures 5.27 to 5.30, show the x component in the magnetic field. This component is the induced magnetic field and as can be seen in the figures, before the step it resembles the induced magnetic field found in the Hartmann flow. Also can be seen in the figures that the highest intensity in this induced magnetic field is located where the fluid velocity gradient is highest. It worthy of mention the fact that this induced magnetic field is behind the suppression of movement in the fluid.

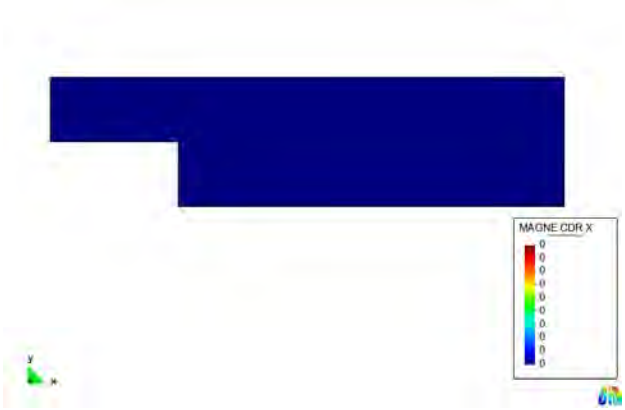

Figure 5.26 *Induced Magnetic Field in the Flow Over a Step for Ha=0*

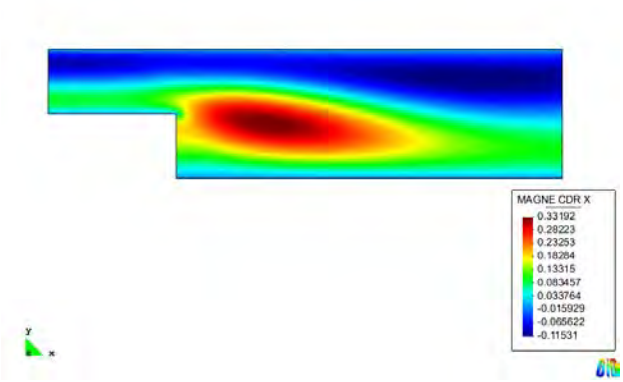

Figure 5.27 *Induced Magnetic Field in the Flow Over a Step for Ha=1*

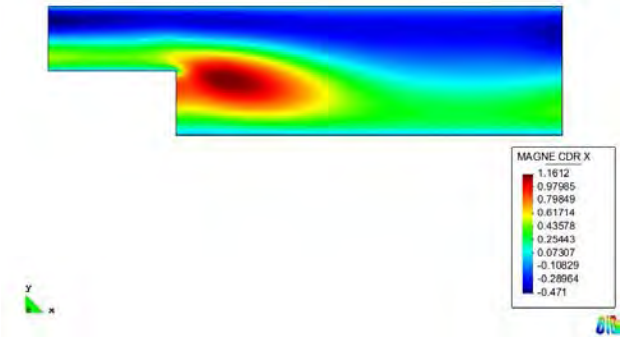

Figure 5.28 *Induced Magnetic Field in the Flow Over a Step for Ha=5*

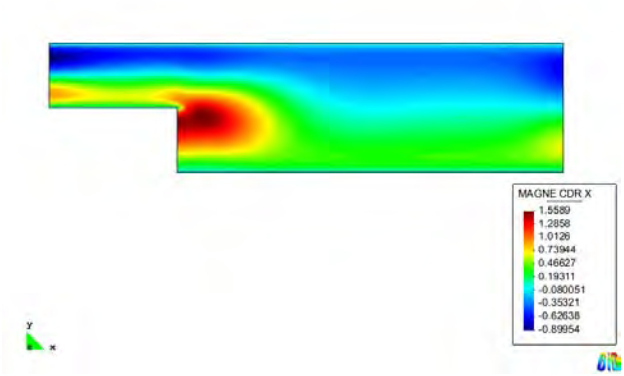

Figure 5.29 *Induced Magnetic Field in the Flow Over a Step for Ha=10*

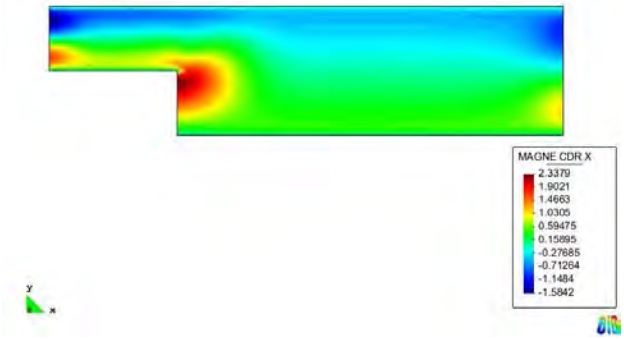

Figure 5.30 *Induced Magnetic Field in the Flow Over a Step for Ha=20*

5.3 Flow Past a Circular Cylinder

This numerical simulation was taken from Armero and Simo [3]. The problem consists on the flow of a conducting fluid around a circular cylinder while a magnetic field is imposed. The flow around a circular cylinder gives origin to the very well known phenomenon of Von Kármán's Vortex Street. Although it is named after Hungarian scientist Theodore Von Kármán, this phenomenon was well known before Von Kármán's birth. Von Kármán himself acknowledges this fact in [37]. The main objective in this numerical simulation is to observe the vanishing of the vortexes shed by the cylinder. Another important result that can be obtained from this simulation is the variation over time of the drag coefficient, the lift coefficient, the velocities and the pressure.

In order to implement this simulation the domain was built using *GiD* and adequate boundary conditions were imposed in that domain boundary. The domain and the boundary conditions are shown in figure 5.31. In order to evaluate the solution obtained from the numerical scheme, several points in the domain are specified in order to follow the temporal variation of velocity and pressure at those points. These points are shown in figure 5.32 and their coordinates are presented in table 5.2.

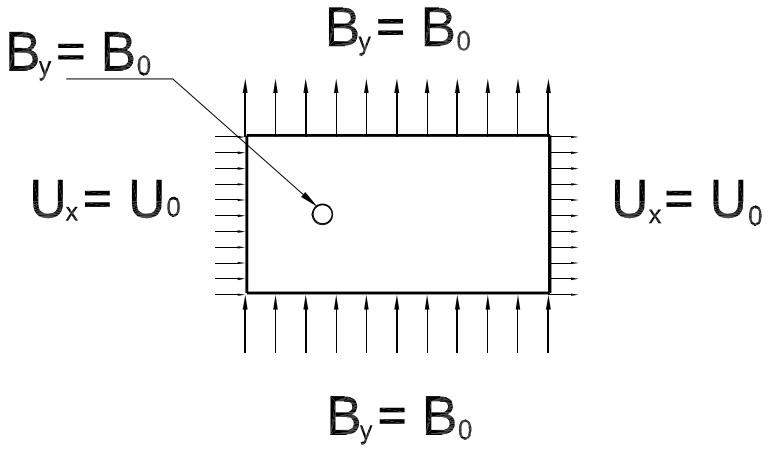

Figure 5.31 *Domain and boudary conditions used in the Von Kármán's Vortex Street*

The boundary conditions for this simulation consist of an imposed constant velocity at the inlet, zero velocity in the upper and lower parts of the domain in the initial time and free velocity at the outlet. The boundary conditions for the magnetic field consist of an imposed normal component in the upper and lower parts of the domain and an imposed tangent component at the inlet and the outlet. In the circular cylinder, the non slip boundary condition is imposed on the surface of the cylinder and the magnetic field is fixed in its y components.

The domain in this simulation was meshed using *GiD*. The mesh is presented in the figure 5.33 and it consists of 4000 linear triangular elements and 2100 nodes.

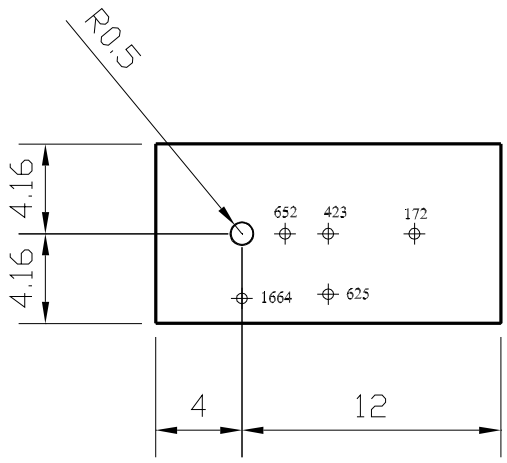

Figure 5.32 *Dimensions and points used in the domain for the Von Kármán's Vortex Street*

Point	x	y
172	12.0	4.0
423	8.0	4.0
625	8.0	1.2
652	6.0	4.0
1664	4.0	1.0

Table 5.2 *Points used in the Von Kármán's Vortex Street and their coordinates*

As can be seen in figure 5.33 the mesh is symmetrical in order to properly simulate the vortex formation.

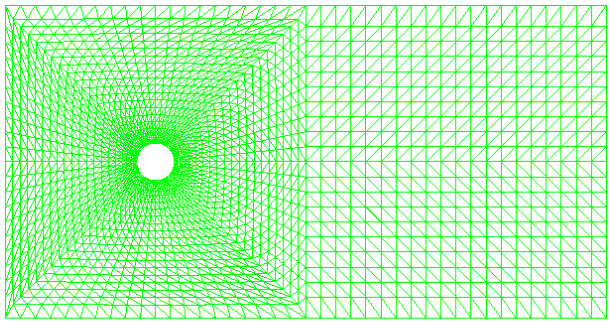

Figure 5.33 *Mesh used in the Von Kármán's Vortex Street*

The numerical simulation is performed for the following Hartmann numbers: $Ha = 0.0, 0.5, 1.0, 2.5, 5.0, 10.0$. These Hartmann numbers are obtained increasing the imposed magnetic field. The intended effect of this increment in the magnetic field is to suppress the vortexes. This effect can be observed in the following sequence of figures where the magnetic field was increased starting from 0.0 until it reached 10.0

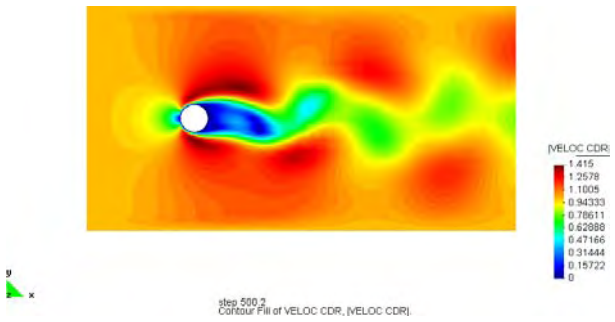

Figure 5.34 *Velocity in the Von Kármán's Vortex Street for Ha=0.0*

Figures 5.34 to 5.39 show how the progressive increment of the intensity in the magnetic field turns off the shedding of the vortexes from the circular cylinder. This is due to the fact that the general effect of Magnetohydrodynamics is to prevent relative movement between the magnetic field and the fluid. This effect gives rise to a more uniform flow, and therefore no vortexes appear in the flow. This uniformity of the velocities in the flow precludes the de–attachment of the boundary layer in the cylinder or any other profile under study. As can be seen in the figures, even low Hartmann numbers preclude the shedding of vortexes. Figure 5.37 shows how

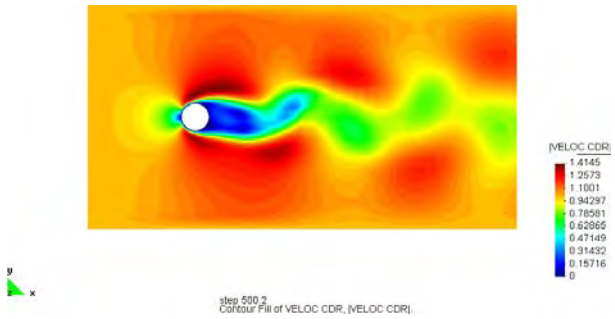

Figure 5.35 *Velocity in the Von Kármán's Vortex Street for Ha=0.5*

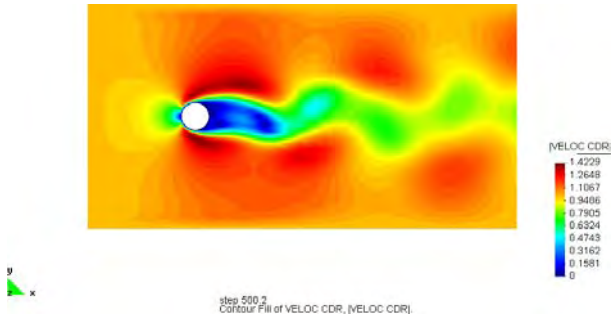

Figure 5.36 *Velocity in the Von Kármán's Vortex Street for Ha=1.0*

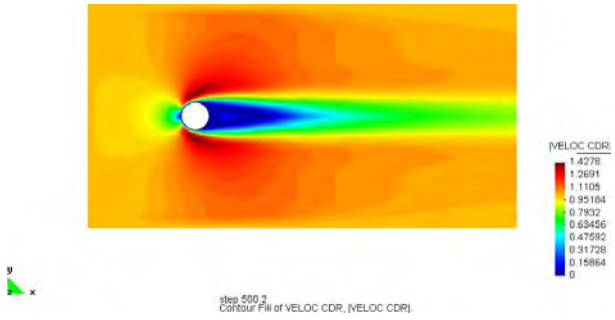

Figure 5.37 *Velocity in the Von Kármán's Vortex Street for Ha=2.5*

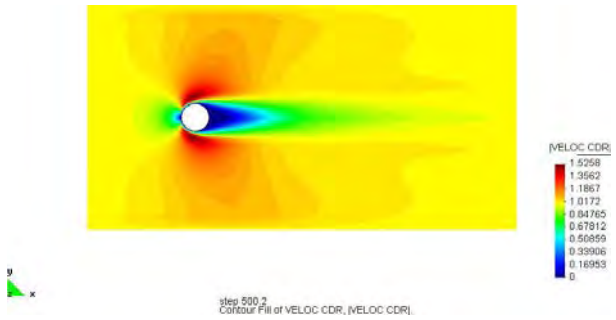

Figure 5.38 *Velocity in the Von Kármán's Vortex Street for Ha=5.0*

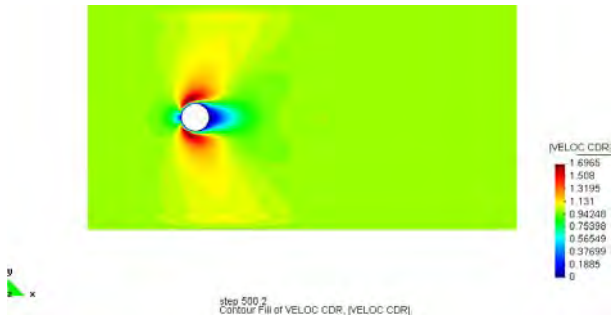

Figure 5.39 *Velocity in the Von Kármán's Vortex Street for Ha=10.0*

at Hartman $Ha = 2.5$ the vortexes have completely vanished. Other important parameters that can be measured are the drag and lift coefficients. These are also important results from this numerical simulation and are defined in equations (5.3.1) and (5.3.2):

$$C_D = \frac{F_D}{\frac{1}{2}\rho\, u^2\, A_P} \tag{5.3.1}$$

$$C_L = \frac{F_L}{\frac{1}{2}\rho\, u^2\, A_P} \tag{5.3.2}$$

where C_D is the drag coefficient, C_L is the lift coefficient, F_D is the drag force, F_L is the lift force, A_P is the frontal area of the circular cylinder, ρ is the density and u is the velocity of the fluid. These coefficients are non dimensional forces over the circular cylinder and provide a way to analyze the flow in time. The variations over time of the drag coefficient are shown in figures 5.40 to 5.45 and the variation over time of the lift coefficient are shown in figures 5.46 to 5.51.

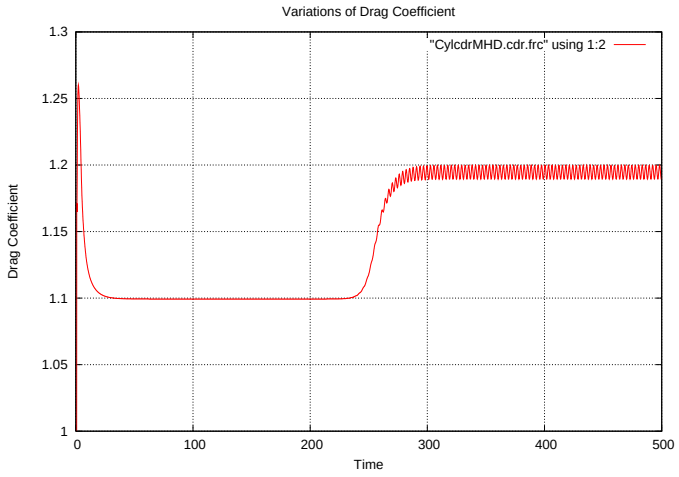

Figure 5.40 *Drag Coefficient in the Von Kármán's Vortex Street for Ha=0.0*

The variations in the drag and lift coefficients show that the suppression of the vortexes affects the forces exerted in the circular cylinder. The biggest effect is upon the lift force which actually vanishes. This fact can be explained by the lack of fluctuations in the pressure. The drag coefficient only diminishes and does not vanish because the velocity in the x axis is still present, but the drag force due to pressure and the vorticity behind the cylinder have disappeared. The effects over the drag an lift coefficients have made MHD an interesting option to control the drag forces and separation control over ships propellers, although this approach is still under investigation [49].

The five points, presented in table 5.2, were selected in order to monitor the values of pressure and velocity in x an y. The values of velocity and pressure are presented for each of the six different Hartmann numbers employed in this

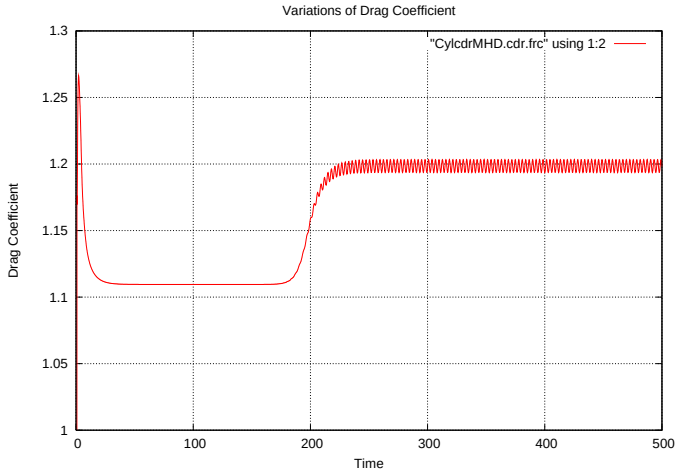

Figure 5.41 *Drag Coefficient in the Von Kármán's Vortex Street for Ha=0.5*

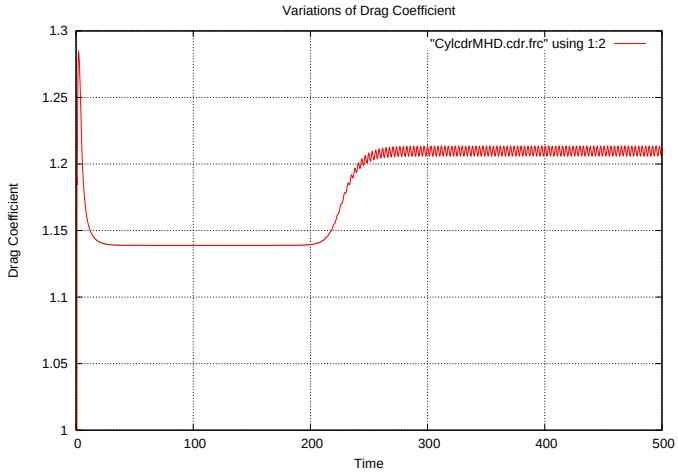

Figure 5.42 *Drag Coefficient in the Von Kármán's Vortex Street for Ha=1.0*

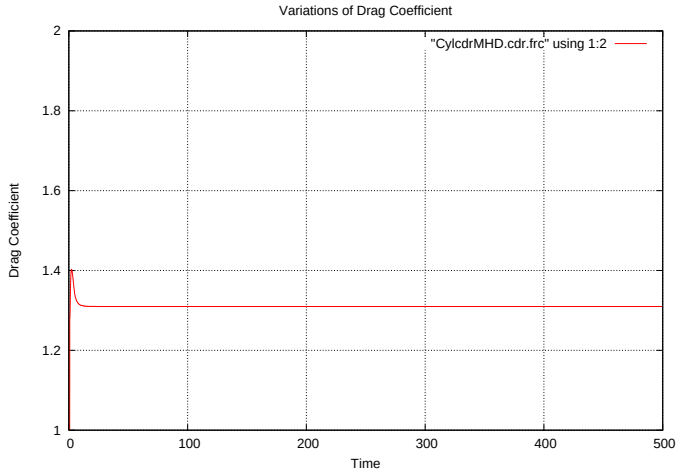

Figure 5.43 *Drag Coefficient in the Von Kármán's Vortex Street for Ha=2.5*

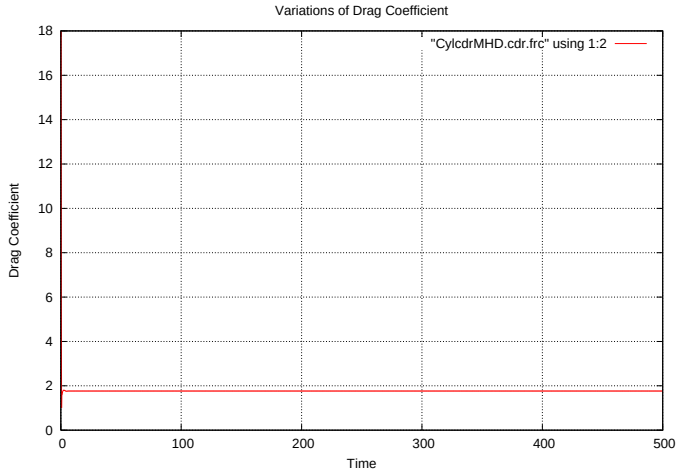

Figure 5.44 *Drag Coefficient in the Von Kármán's Vortex Street for Ha=5.0*

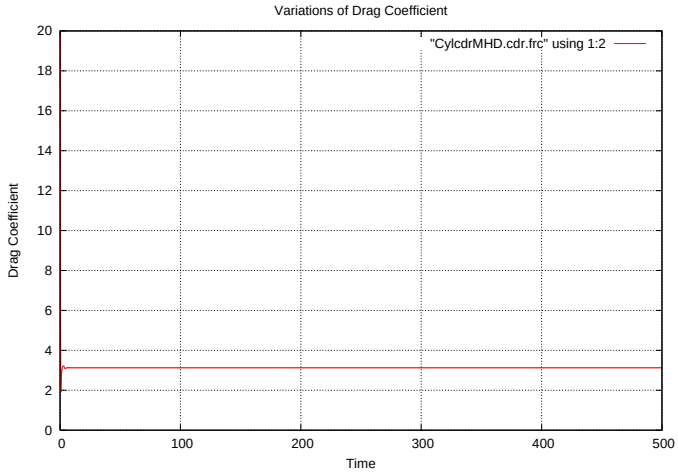

Figure 5.45 *Drag Coefficient in the Von Kármán's Vortex Street for Ha=10.0*
Ha=1.0

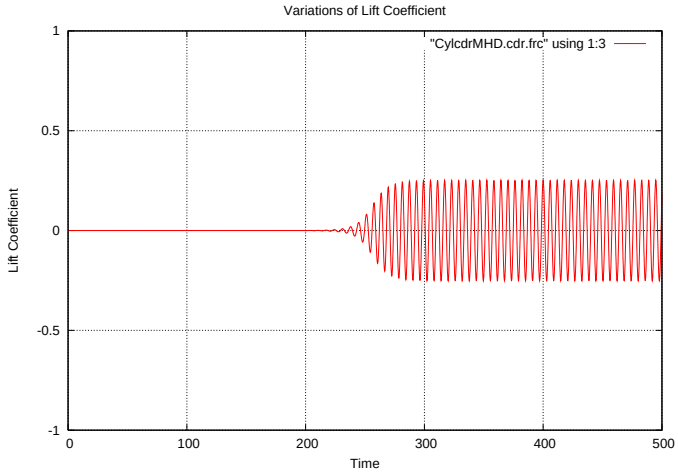

Figure 5.46 *Lift Coefficient in the Von Kármán's Vortex Street for Ha=0.0*

Ha=1.0

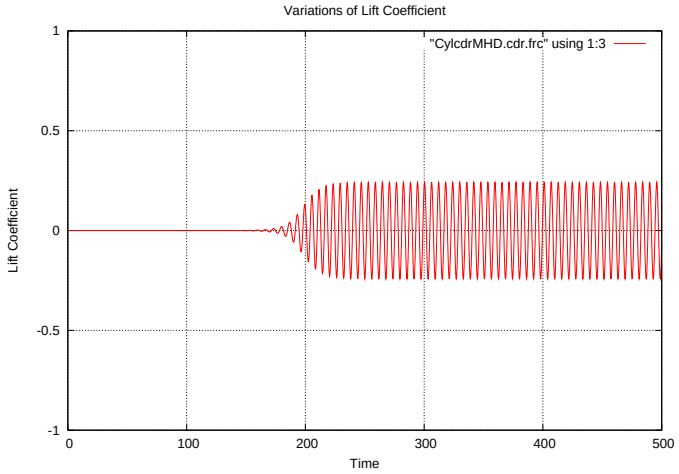

Figure 5.47 *Lift Coefficient in the Von Kármán's Vortex Street for Ha=0.5*

Ha=1.0

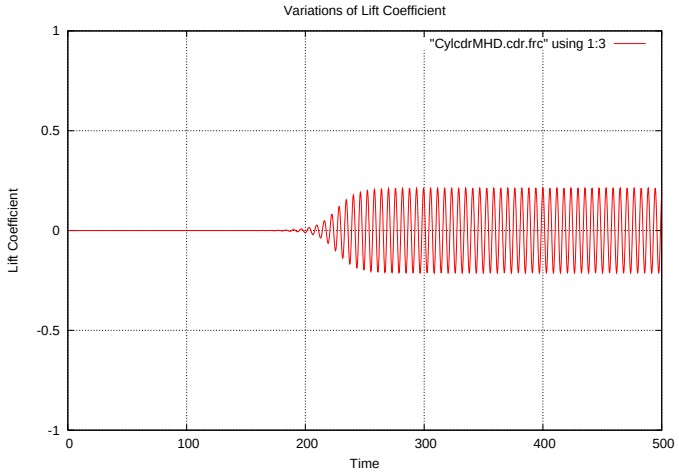

Figure 5.48 *Lift Coefficient in the Von Kármán's Vortex Street for Ha=1.0*

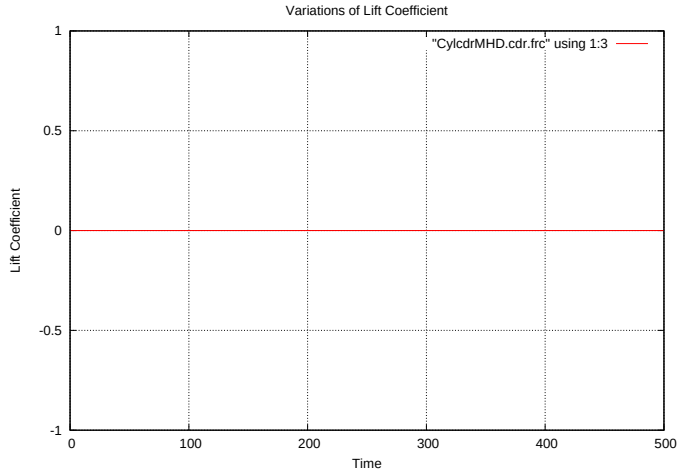

Figure 5.49 *Lift Coefficient in the Von Kármán's Vortex Street for Ha=2.5*

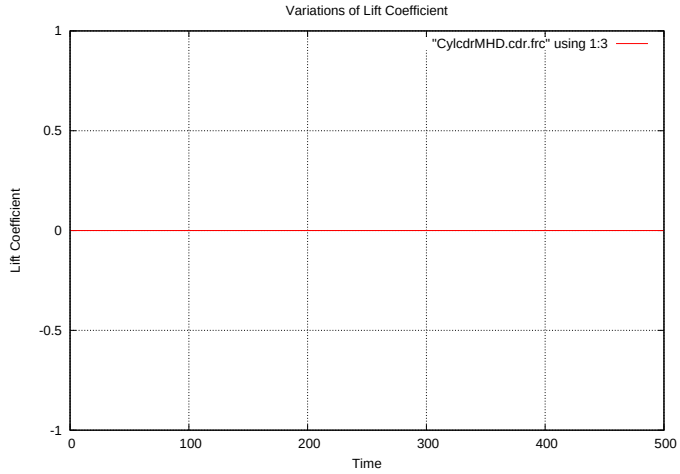

Figure 5.50 *Lift Coefficient in the Von Kármán's Vortex Street for Ha=5.0*

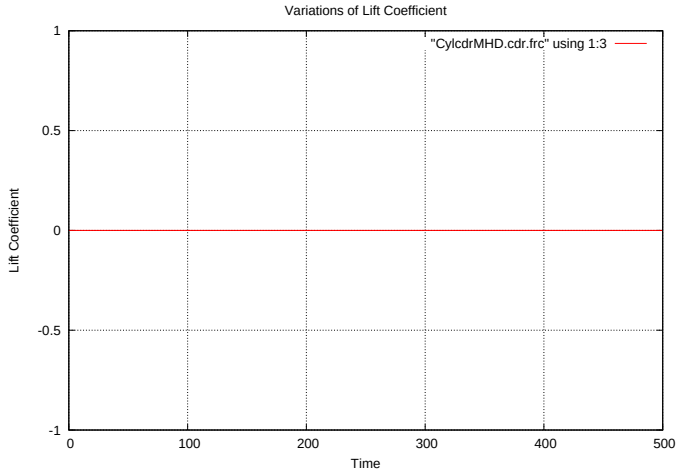

Figure 5.51 *Lift Coefficient in the Von Kármán's Vortex Street for Ha=10.0*

numerical simulation, and as can be seen in the figures its behavior matches the previously presented behavior of the drag and lift coefficients.

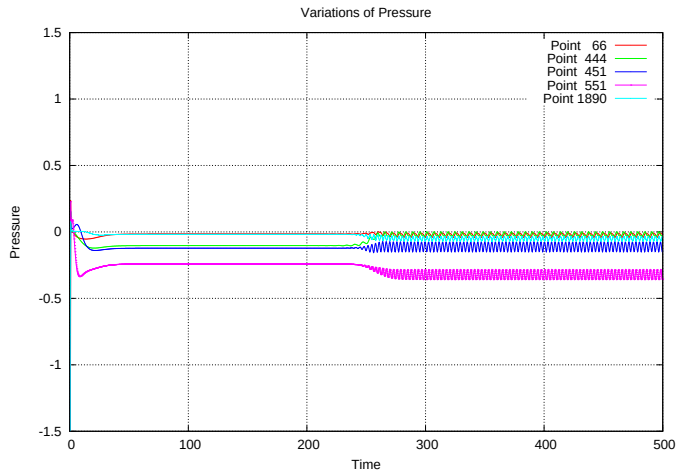

Figure 5.52 *Pressure Variations in the Von Kármán's Vortex Street for Ha=0.0*

Figures 5.52 to 5.54 show the time variation of pressure for the five points selected for $Ha = 0.0, 0.5, 1.0$. As can be seen in those figures the initial increasing of the magnetic field has very little effect over the variations in pressure.

Figures 5.55 to 5.57 show the time variation of pressure for the five points selected for $Ha = 2.5, 5.0, 10.0$. Contrary to $Ha = 0.0, 0.5, 1.0$ the effect over these pressures is significant, because the magnetic field completely suppresses the oscillations in pressure. The oscillations in the velocity for the different Hartmann numbers also present the same behavior as the oscillations in pressure. Figures

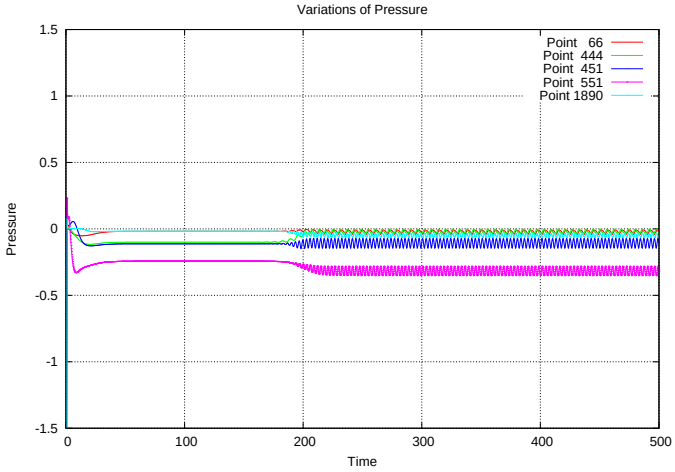

Figure 5.53 *Pressure Variations in the Von Kármán's Vortex Street for Ha=0.5*

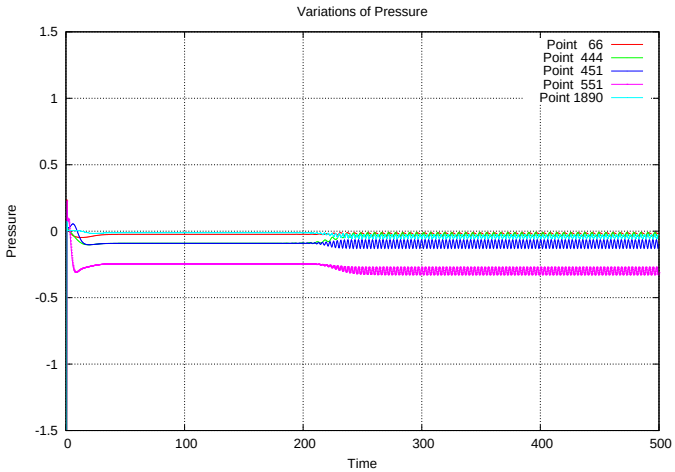

Figure 5.54 *Pressure Variations in the Von Kármán's Vortex Street for Ha=1.0*

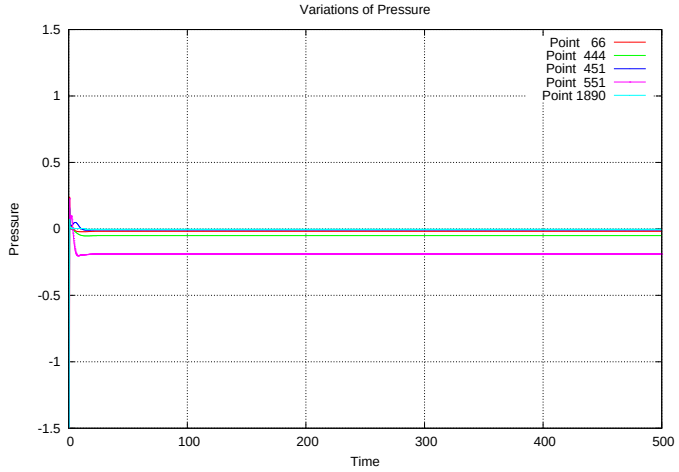

Figure 5.55 *Pressure Variations in the Von Kármán's Vortex Street for Ha=2.5*

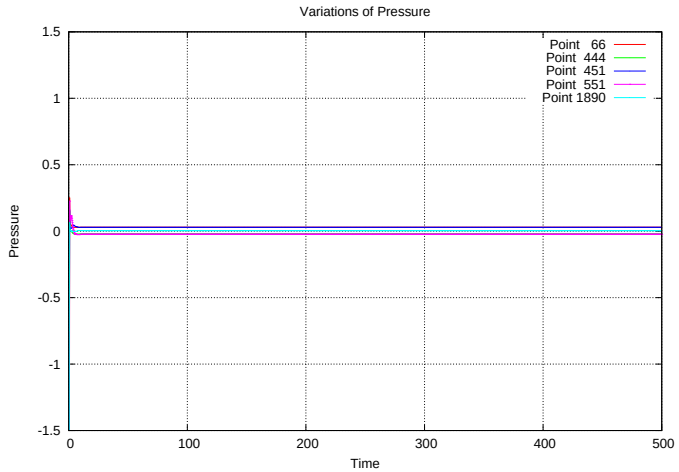

Figure 5.56 *Pressure Variations in the Von Kármán's Vortex Street for Ha=5.0*

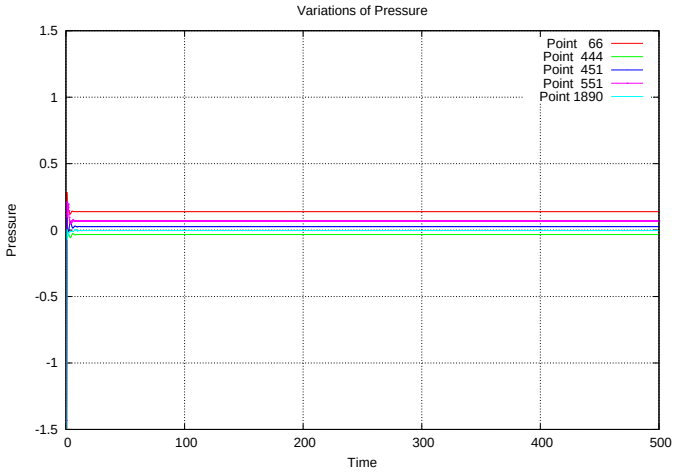

Figure 5.57 *Pressure Variations in the Von Kármán's Vortex Street for Ha=10.0*

5.58 to 5.63 show the variation in the x component of the velocity and figures 5.64 to 5.69 show the variation in the y component of the velocity.

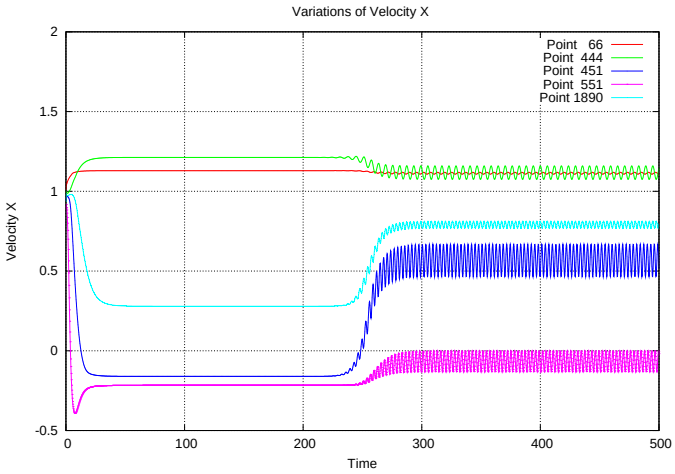

Figure 5.58 *Variations for Velocity x in the Von Kármán's Vortex Street for Ha=0.0*

As conclusion it can be said that the presence of magnetic fields in flows where oscillations can occur precludes their onset. This numerical benchmark shows clearly this behavior. This numerical benchmark also offers clues over the use of magnetic fields in the control of drag and lift forces. As can be seen in the drag and lift graphics the use of magnetic fields, reduce the value of the drag forces and also controls the de–attachment of boundary layers.

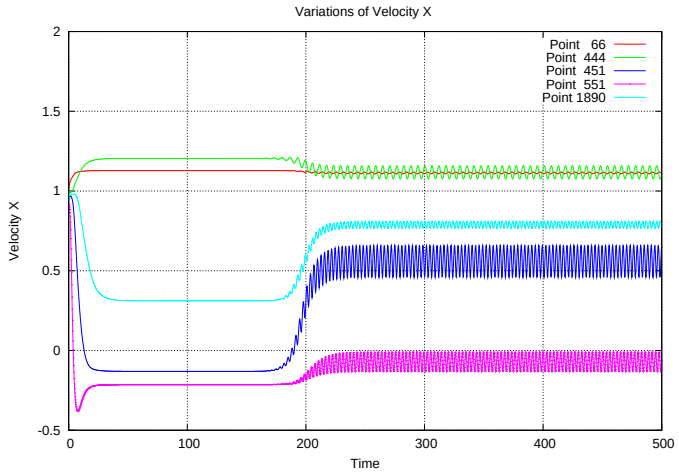

Figure 5.59 *Variations for Velocity x in the Von Kármán's Vortex Street for Ha=0.5*

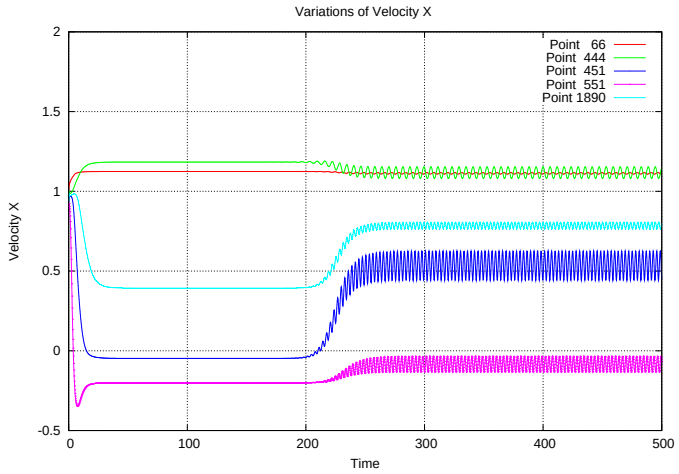

Figure 5.60 *Variations for Velocity x in the Von Kármán's Vortex Street for Ha=1.0*

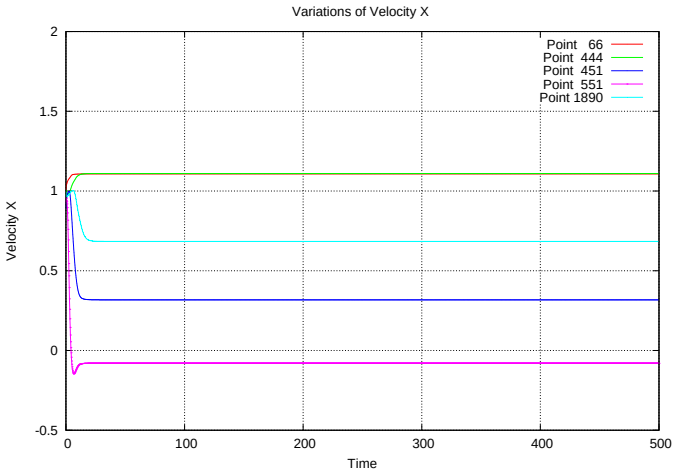

Figure 5.61 *Variations for Velocity x in the Von Kármán's Vortex Street for Ha=2.5*

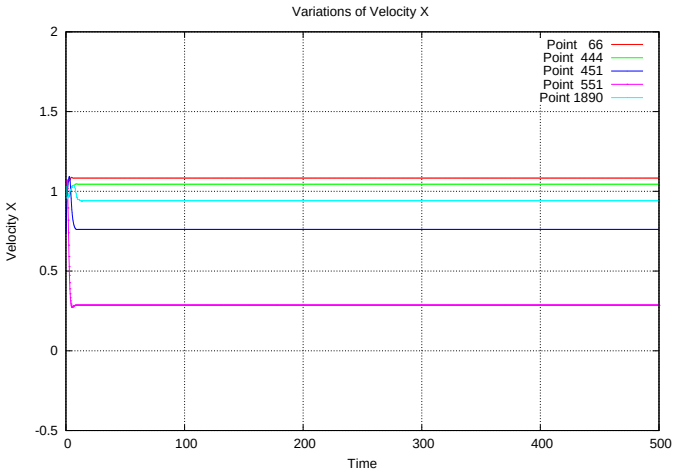

Figure 5.62 *Variations for Velocity x in the Von Kármán's Vortex Street for Ha=5.0*

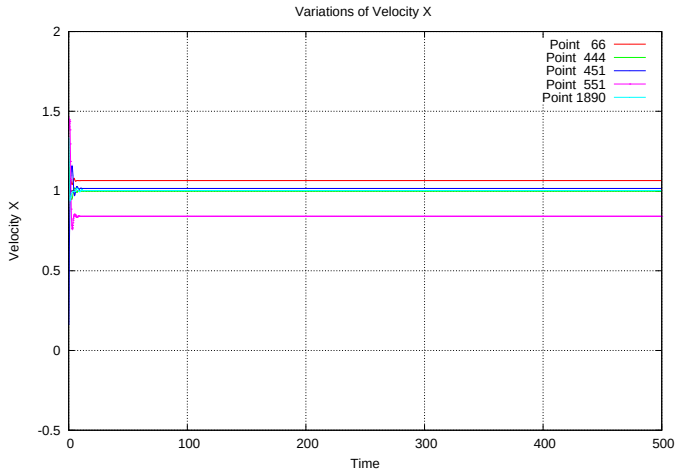

Figure 5.63 *Variations for Velocity x in the Von Kármán's Vortex Street for Ha=10.0*

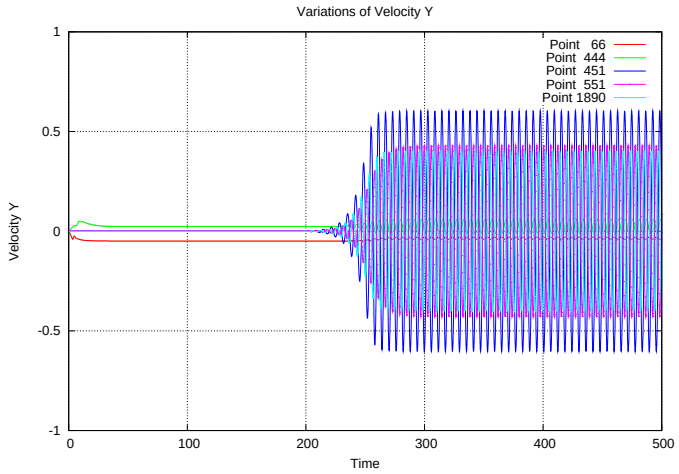

Figure 5.64 *Variations for Velocity y in the Von Kármán's Vortex Street for Ha=0.0*

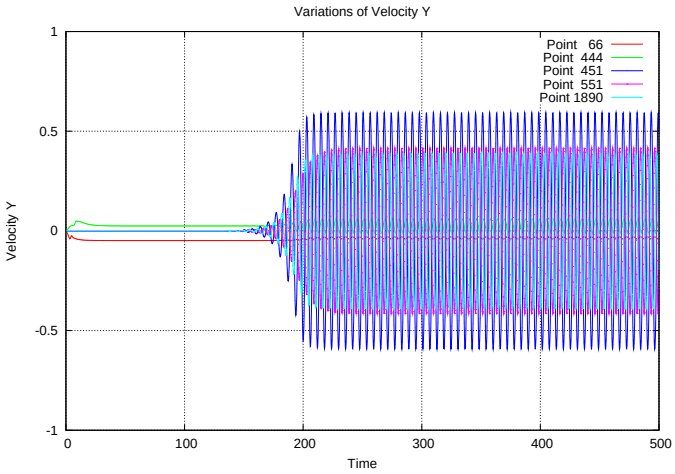

Figure 5.65 *Variations for Velocity y in the Von Kármán's Vortex Street for Ha=0.5*

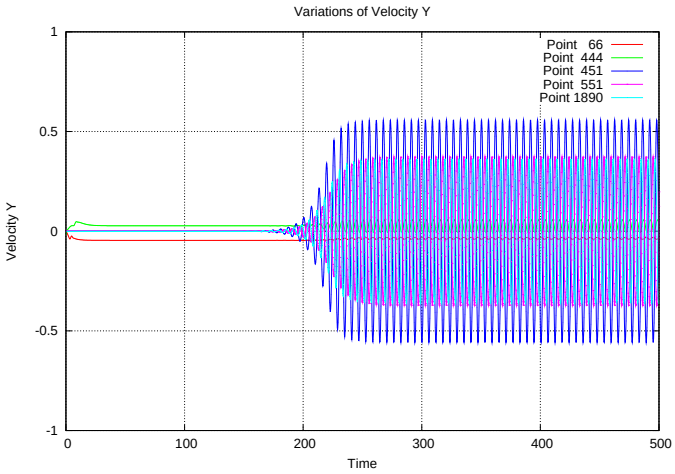

Figure 5.66 *Variations for Velocity y in the Von Kármán's Vortex Street for Ha=1.0*

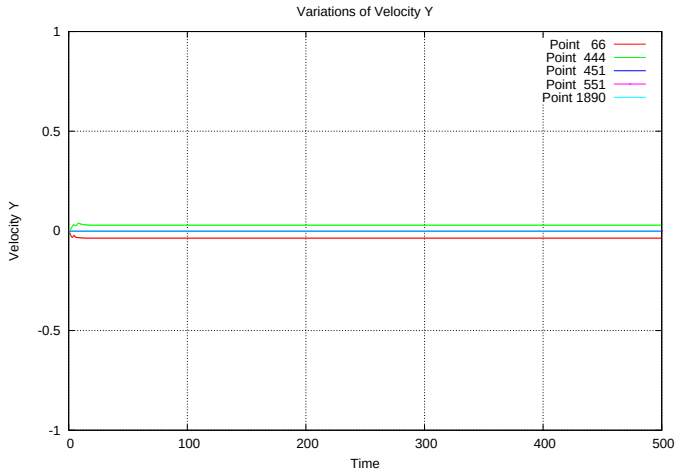

Figure 5.67 *Variations for Velocity y in the Von Kármán's Vortex Street for Ha=2.5*

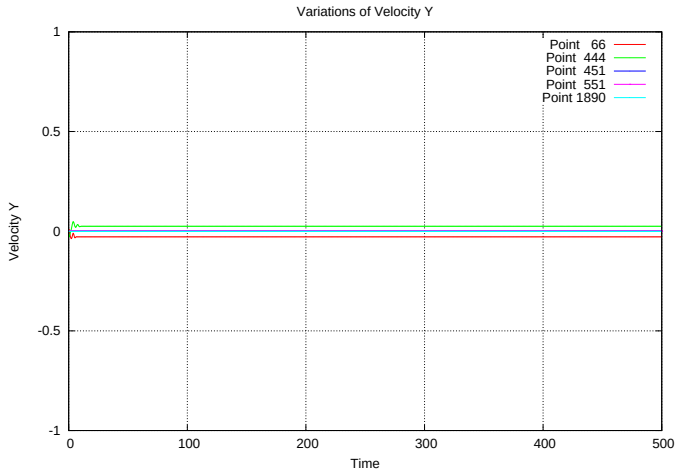

Figure 5.68 *Variations for Velocity y in the Von Kármán's Vortex Street for Ha=5.0*

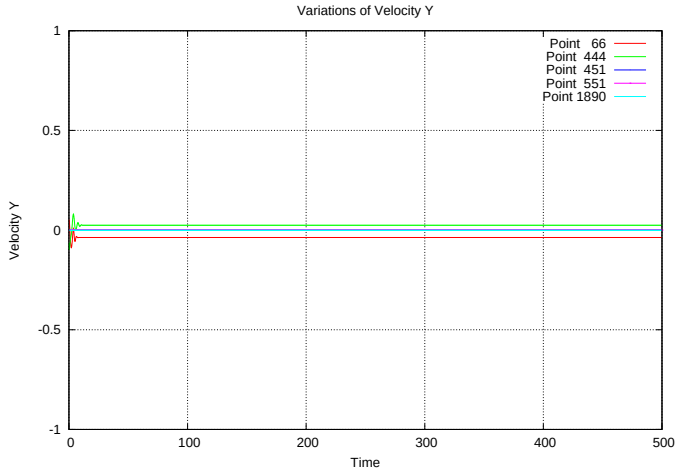

Figure 5.69 *Variations for Velocity y in the Von Kármán's Vortex Street for Ha=10.0*

5.4 Clogging in Continuous Casting of Steel

Steel is the most important metal alloy in the present. The majority of the steel is made using the Continuous Casting Process. This process is briefly described in section 2.3.1. Among the possible problems in the continuous casting process, the blocking of the nozzle employed is one of the most severe.

The main objective of this numerical simulation is to observe the behavior of the flow in a continuous casting nozzle while a magnetic field is applied. The blocking is particularly problematic when low carbon steels are casted because some deoxidation products e.g. alumina, get attached to the walls of the nozzle forming buildups. These buildups can eventually prevent the flow of steel through the nozzle. This can lead to a decrease in the quality of the steel or even to stop the continuous casting operation and diminish the productivity, [53].

The origin of the buildups in the nozzle is associated to the appearance of a recirculation zone in the entry of the nozzle. This recirculation zone is originated by a deattachment of the flow. Although the nozzle can be designed to prevent recirculation, even a small misalignment can originate a de–attachment. In order to prevent the recirculation of the flow, the use of a magnetic field has been proposed, [35] and [42]. The magnetic field used to suppress the recirculation is produced by a coil oriented coaxially with the flow. The general effect of the magnetic field is to produce a radial force over the fluid and therefore it tends to attach to the walls of the nozzle. The domain of the nozzle in a continuous casting process is presented in figure 5.70. This numerical simulation is bi–dimensional in its nature.

The boundary conditions used for this numerical simulation are presented in figure 5.70. Basically these boundary conditions consist of a fixed value for the radial component of the magnetic field for all the wall, the non-slip boundary condition for the velocity and finally an applied acceleration due to the gravity. These boundary conditions basically represent the conditions in the tundish and

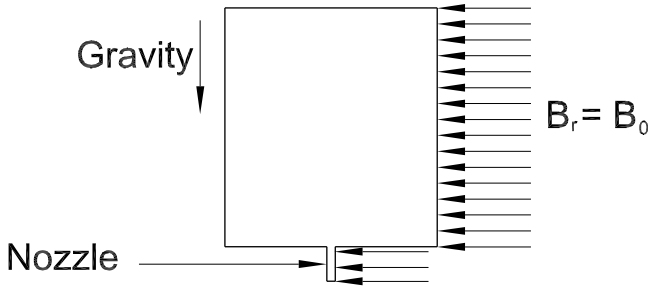

Figure 5.70 *Domain and Boundary Conditions for Nozzle Clogging*

the nozzle, as they are represented in figure 2.1. The following Hartmann numbers have been considered: $Ha = 1$, 10, 50 and 120. The Reynolds number that has been taken is $Re \approx 20000$ and the magnetic Reynolds number is $Rm = 0.03632$

The mesh used in this example is shown in figures 5.71 and 5.72. Basically, it is a symmetrical mesh of 18282 triangular elements with 9335 nodes. This degree of detail was needed in order to capture the behavior of the fluid in the nozzle, i.e. the recirculation.

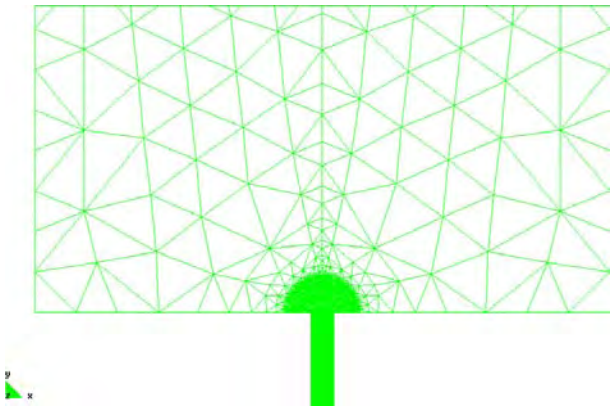

Figure 5.71 *Mesh used for Nozzle Clogging*

The nature of this example is purely qualitative because there is no numerical benchmark to compare. The dimensions and general setting of this example were taken from [42], where the approach to tackle this problem is purely analytical. Due to the dynamic nature of this example the Hartmann number used in order to get a uniform velocity field for the fluid is really high.

As can be seen in figures 5.73 to 5.77 the use of magnetic fields in the nozzle reduces the magnitude of the recirculation zone. The velocity of the fluid tends to

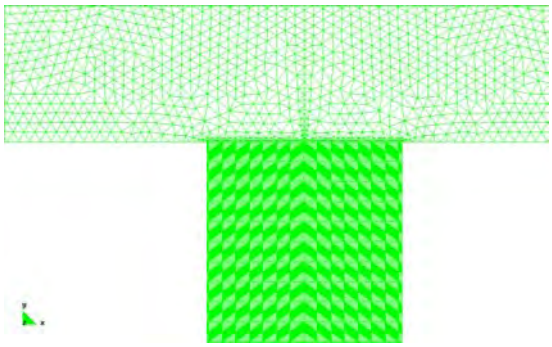

Figure 5.72 *Detail of the Mesh used for Nozzle Clogging*

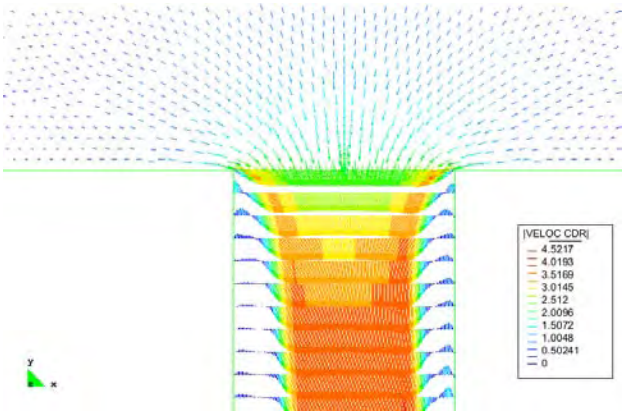

Figure 5.73 *Detail of Velocity for Ha=0*

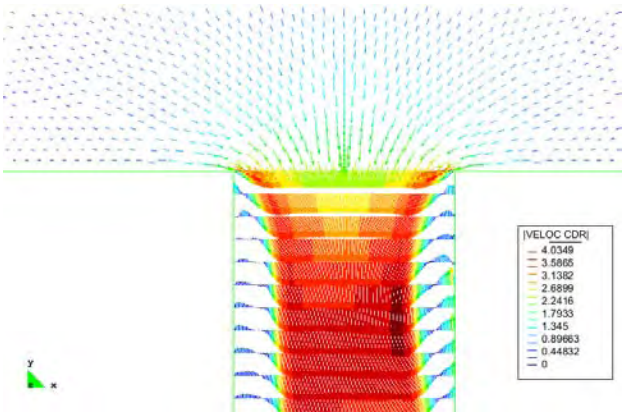

Figure 5.74 *Detail of Velocity for Ha=1*

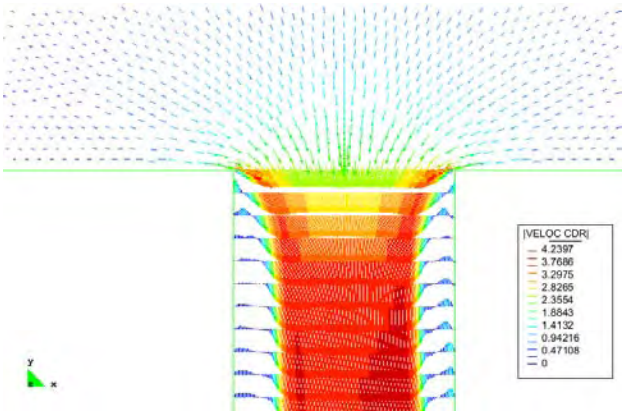

Figure 5.75 *Detail of Velocity for Ha=10*

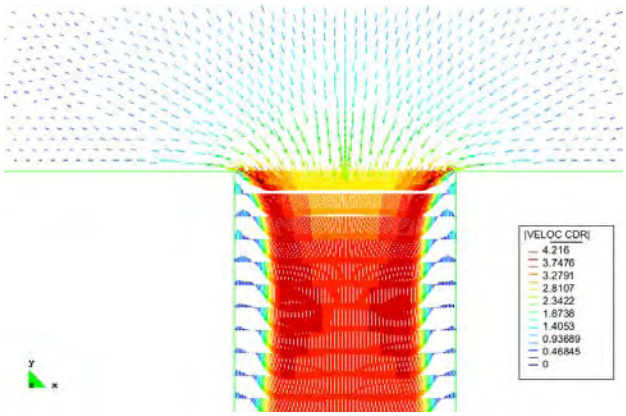

Figure 5.76 *Detail of Velocity for Ha=50*

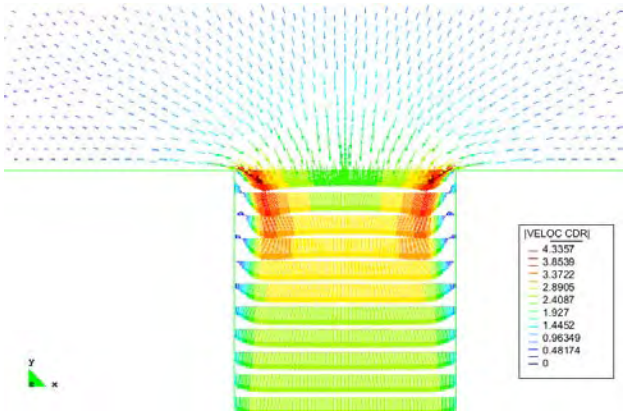

Figure 5.77 *Detail of Velocity for Ha=120*

get uniform and stabilizes the flow making less likely the occurrence of buildups. Eventually these effects of the magnetic fields applied to the nozzle provide an effective mean to improve the quality of the steel made by the continuous casting process.

5.5 Crystal Growth

The Czochralski process for the growth of semiconductor crystals is extensively used in the semiconductor industry today. It is named after Jan Czochralski, a polish scientist who discovered it in 1916. The main objective of this process is to get a mono–crystal. To perform this task a crystal seed is slowly pulled out of the crucible, where the semiconductor is melt. This action provides the melt with a unique direction for the solidification. In order to produce a cylindrical crystal, the seed is subject to a rotation while it is pulled out of the crucible. Czochralski process is mainly used to produce crystals of Si and Ge for the semiconductor industry, but it can also be used with metals and salts.

The technological importance of this process is justified, because it provides high purity semiconductor wafers. This wafers are used for the manufacture of semiconductor devices such as solar cells and integrated circuits. The degree of precision required by this kind of manufacture is made obvious given the fact that the wafers are cut with a thickness of 0.2 mm or even less. Therefore any impurity or imperfection in the crystal must be avoided.

The main objective of this numerical simulation is to observe the behavior of the molten semiconductor inside a crucible, in the Czochralski process. This numerical simulation was proposed by Bückle and Schäfer [7], in 1993. The numerical simulation of this crystal growth process is quite complex because it involves a heat transfer problem together with the MHD problem. In the Czochralski process, the convection gives rise to fluid movements which can be harmful for the crystalline structure of the silicon. Basically, the convection movements can introduce structural defects in the crystal. By applying an intense magnetic field, the convection movements are damped inside the crucible and the defects are diminished if not completely eliminated. For this numerical simulation cylindrical coordinates were used, and due to the symmetry conditions over the domain only half of a cross section of the domain was used. A simplified geometry for this problem is presented in figure 5.78. As can be seen in the previously mentioned figure, a crystal seed is been pulled out from a crucible and at the same time a rotational movement is being applied to the seed in order to obtain a cylindrical crystal.

The section under study presented at figure 5.78 is explained in detail in figure 5.79. Basically, figure 5.79 depicts the general situation of a Czochralski process presented for this numerical benchmark. As can be seen the problem consists in a vertical cylindrical crucible filled with a molted semiconductor to a height H, which is rotating with angular velocity Ω_C. The coaxial crystal on the top of the crucible is also rotating, but at the opposite direction of the crucible with angular velocity Ω_X. It is assumed that the crystal and the crucible are isothermal with temperature T_X and T_C respectively.

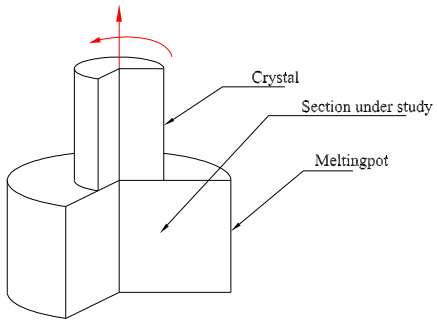

Figure 5.78 *Section Under Study for the Czochralski Process*

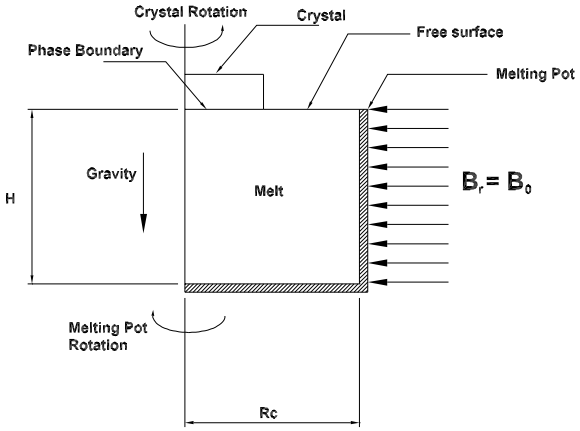

Figure 5.79 *General Depiction of Czochralski Process*

The boundary conditions for this numerical simulation are presented in figure 5.80. The nature of this numerical simulation makes necessary to introduce boundary conditions for velocity, temperature and magnetic field. The first kind of boundary conditions is imposed over the velocity. Non slip boundary conditions are imposed in the crucible walls, the bottom of the crucible and at the interface between the crystal and the molten semiconductor. Also, it must be considered that the crystal and the crucible are rotating in opposite directions, therefore the velocity for the liquid silicon at those interfaces is determinated by the rotational speed of the crystal and the crucible, respectively. The velocity of the fluid at the crucible walls is the same velocity of the walls, therefore this velocity is given by the product $\Omega_C R_C$, where R_C is the radius of the crucible. The velocity of the fluid at the crystal is given by $\Omega_X R_X$ where R_X is the radius of the crystal. In the case of the space between the crystal and the crucible walls, the velocity is not subject to any constrain but to remain as a free surface.

The second kind of boundary condition is imposed over the temperature,which is represented by letter T in this example. For the crucible walls, the temperature of the molten silicon is fixed to T_C and for the molten silicon in contact with the crystal, the temperature is fixed to T_X. For the molten silicon in contact with the bottom of the crucible a zero heat flux boundary condition is imposed, the same condition is applied to the symmetry line. The space between the crystal and the walls of the crucible is subject to a linear variation of temperature between the temperature of the crystal and the temperature of the crucible walls.

The third boundary conditions are for the magnetic field. For this numerical simulation all interfaces are assumed to be insulating walls. Finally, it is worthy of mention the fact that in figure 5.80, radial coordinate r is normalized by R_C, i.e. $r = 1$ in the right border of the domain.

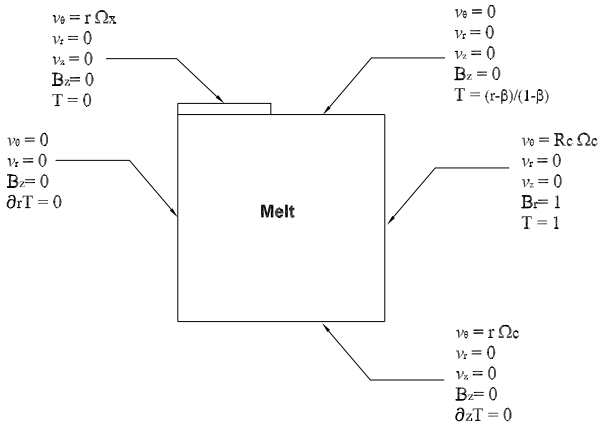

Figure 5.80 *Boundary Conditions Used for Czochralski Process*

In order to completely characterize this numerical simulation some non dimensional parameters must be defined. These parameters are the Reynolds number for the crucible and the crystal, the Prandtl and Grashof numbers and the aspect

Problem	Gr	Re_X	Re_C
A1	0	10^2	0
A2	0	10^3	0
B1	0	10^2	-2.5×10^1
B2	0	10^3	-2.5×10^2
C1	10^4	0	0
C2	10^5	0	0
D1	10^4	10^1	0
D2	10^5	10^1	0

Table 5.3 *Parameters and their values for the different cases in the Czochralski Process*

ratios of the crucible. These parameters are defined as:

$$Re_C = \frac{R_C^2 \left|\Omega_C\right|}{\nu} \tag{5.5.1}$$

$$Re_X = \frac{R_C^2 \left|\Omega_X\right|}{\nu} \tag{5.5.2}$$

$$Pr = \frac{\nu}{\kappa} \tag{5.5.3}$$

$$Gr = \frac{g\hat{\beta}\left(T_C - T_X\right) R_C^3}{\nu^2} \tag{5.5.4}$$

$$\alpha = \frac{H}{R_C} \tag{5.5.5}$$

$$\beta = \frac{R_X}{R_C} \tag{5.5.6}$$

To limit the number of possible combinations of these non–dimensional parameters eight combinations were analyzed during this research. These combinations are based on those proposed by Bückle and Schäfer in their original paper [7]. These cases are representative of the posible situations to be present in the actual Czochralski process. The values for Reynolds and Grashof numbers are presented in table 5.3 for all the cases. For all the cases proposed the aspect ratios and the Prandtl number are fixed at $\alpha = 1.0$, $\beta = 0.4$ and $Pr = 0.05$.

In this research, the cases presented in table 5.3, were performed increasing the Hartmann number. For each case listed, the Hartmann number used were $Ha = 0.0, 5.0$ and 10.0.

For the sake of clarity and brevity, in this document only the most important results of cases A2, B2, C2 and D2 cases are presented. This is done in order to not overwhelm the reader with several figures.

The domain for this simulation was meshed with *GiD* and the mesh is presented in figure 5.81. This mesh consists of 5408 linear triangular elements and 2809 nodes. As can be seen in the figure the mesh is coarse in the center of the domain and

more refined near the boundaries in order to capture any boundary layer present in the simulation.

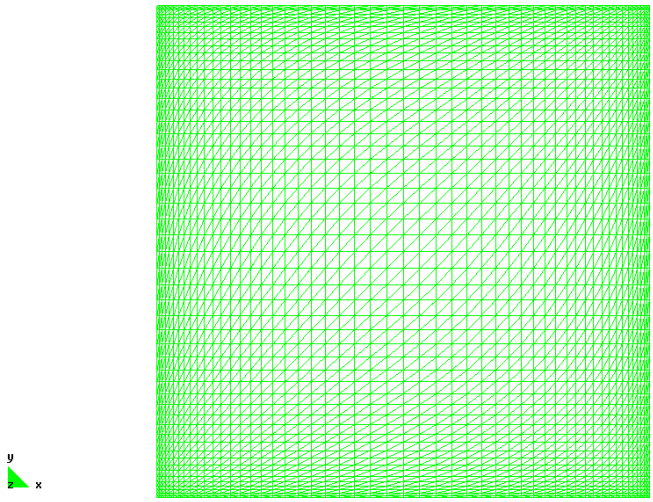

Figure 5.81 *Mesh Used for Czochralski Process*

5.5.1 Case A2

In this case, the crystal is provided with a constant rotational speed and the crucible is stationary, therefore the liquid semiconductor in contact with the crystal has a velocity proportional to the rotational speed of the crystal. In the other hand, the liquid semiconductor in contact with the crucible has zero velocity. This situation describes the basic setting that is possible to find in a real Czochralski process. There is no temperature imposed over the crucible and therefore there are not convection induced movements in the liquid semiconductor.

For Hartmann $Ha = 0.0$ the velocity norm is shown in figure 5.82. The vector field for the velocity is shown in figure 5.83, this figure is presented using an isometric perspective in order to visualize the velocity vectors. As can be seen in those figures, the highest velocities are found near the crystal. For this case there is no magnetic field.

For Hartmann $Ha = 5.0$, an homogenization of the flow field can be appreciated. This effect can be seen in figures 5.84. The radial component of the magnetic field is presented in figure 5.86

Finally for Hartmann $Ha = 10.0$, the homogenization of the flow field is quite evident as can be seen in figure 5.87. It can be said that the effect of the magnetic field is to get a more uniform flow field in the crucible. The radial component for the magnetic field is presented in figure 5.89.

One important aspect of any numerical simulation is its convergence properties. For case A2 and $Ha = 10.0$ figure 5.90 shows the convergence toward the steady

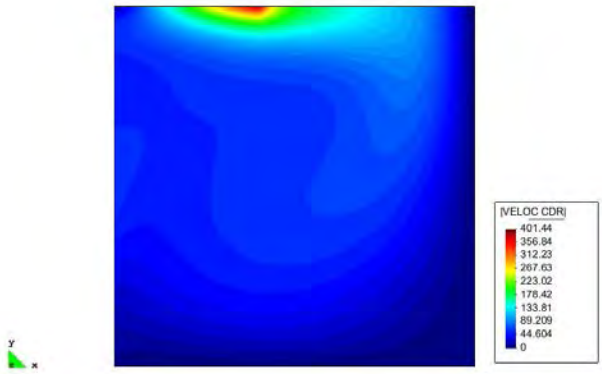

Figure 5.82 *Velocity norm for Ha=0.0 and case A2*

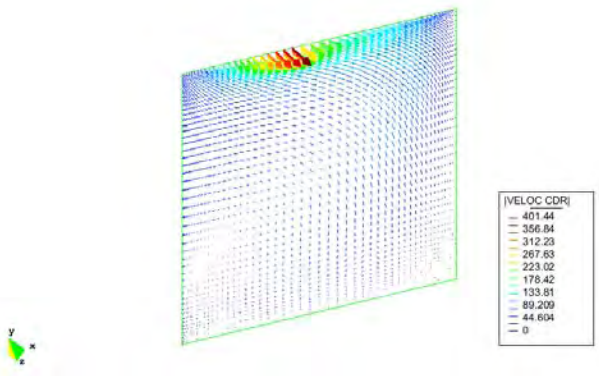

Figure 5.83 *Velocity vectors for Ha=0.0 and case A2*

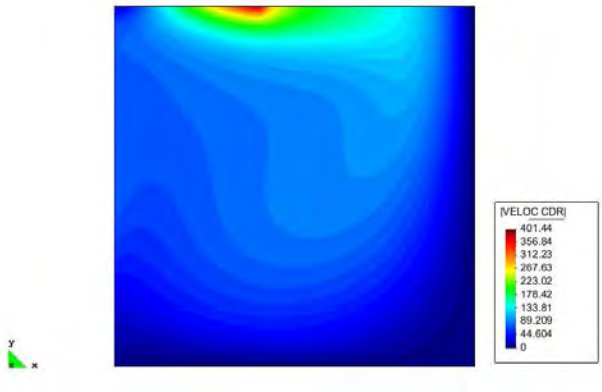

Figure 5.84 *Velocity norm for Ha=5.0 and case A2*

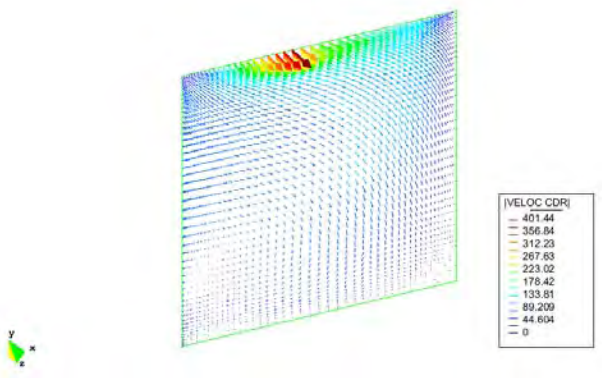

Figure 5.85 *Velocity vectors for Ha=5.0 and case A2*

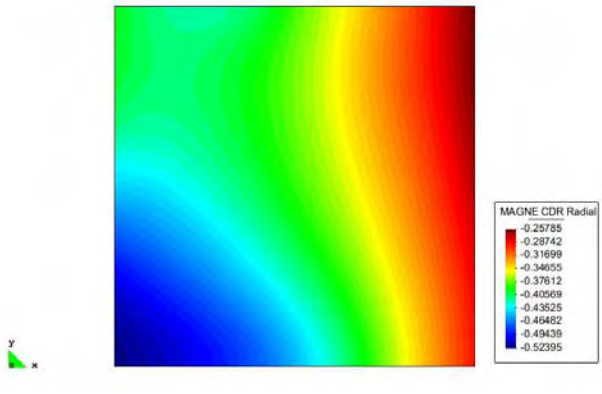

Figure 5.86 *Radial component of the magnetic field for Ha=5.0 and case A2*

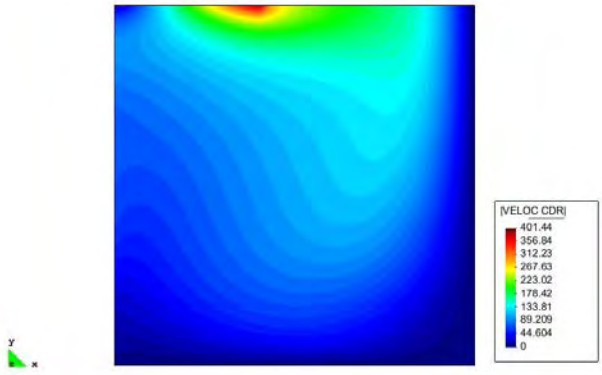

Figure 5.87 *Velocity norm for Ha=10.0 and case A2*

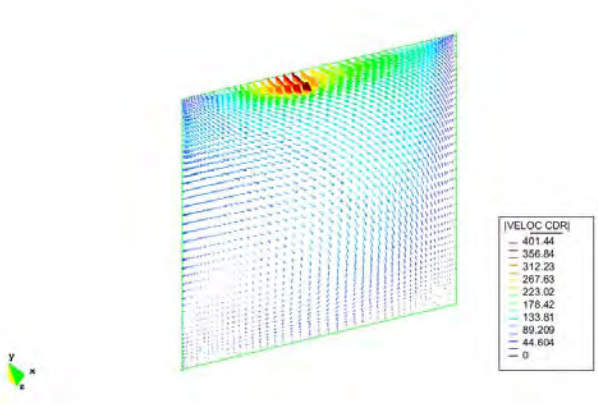

Figure 5.88 *Velocity vectors for Ha=10.0 and case A2*

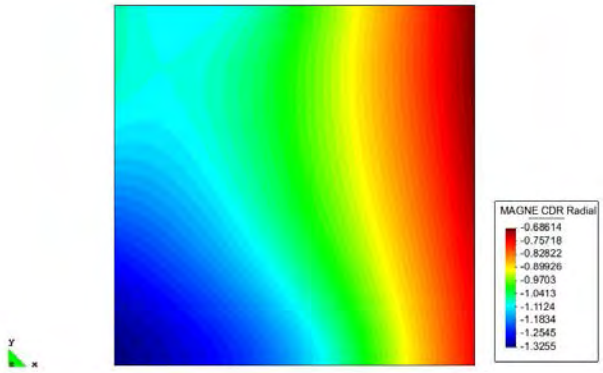

Figure 5.89 *Radial component of the magnetic field for Ha=10.0 and case A2*

state measured as the norm of $\delta_t \mathbf{U}$ in time normalized by $\delta_t \mathbf{U}$ in the first time step and in percentage.

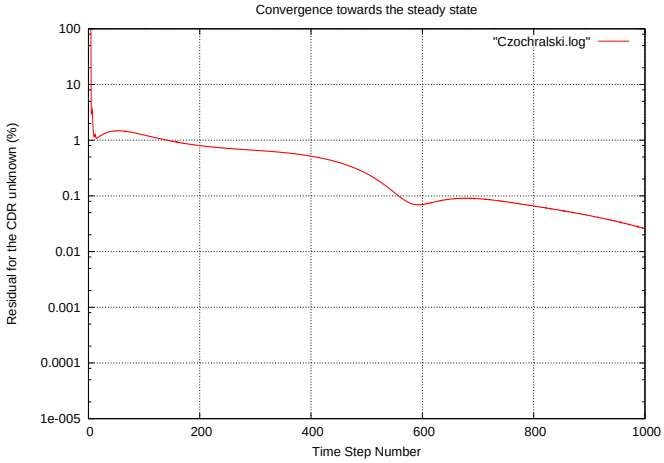

Figure 5.90 *Convergence toward the steady state for Ha=10.0 and case A2*

5.5.2 Case B2

In this case, in addition to the conditions described for case A2, the crucible is provided with constant rotational speed. This movement of the crucible makes the simulation closer to the real Czochralski process, but also makes the flow pattern more complex and difficult to understand and analyze. In this case the crucible is rotating counterclockwise, while the crystal is rotating clockwise.

For Hartmann $Ha = 0.0$, figure 5.91 shows the velocity norm, for case B2. There is no magnetic field imposed an therefore the flow field has no perturbation. Figure 5.92 presents the vector field for velocity for the same Hartmann number.

For Hartmann $Ha = 5.0$ there is a noticeable change in the flow field. As can be seen in figures 5.93 the velocity is again in a homogenization process. This is particularly important in the upper part of the domain, where the free surface of the liquid semiconductor is subject to a large change in velocities and therefore it is likely to be broken and allow the entrance of foreign bodies that can be harmful for the quality of the crystal. The radial component of the magnetic field is presented in figure 5.95

Finally, for Hartmann $Ha = 10.0$, the homogenization of the flow field is quite evident, as can be seen in figures 5.96. Again the upper boundary of the domain shows a large section where the velocity gradient in the neighborhood of the crystal is not as severe as for $Ha = 0.0$. This favors the quality of the crystal.

Figure 5.99 shows the convergence history toward steady state for case B2 and $Ha = 10.0$.

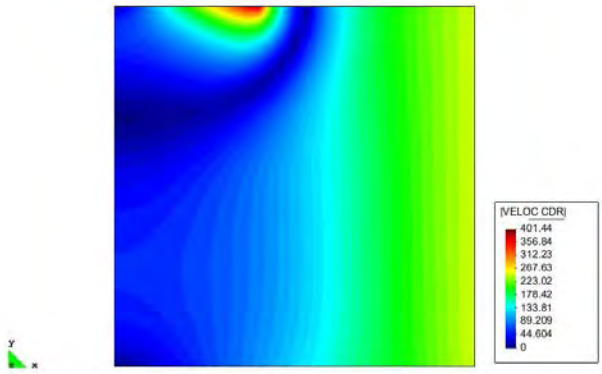

Figure 5.91 *Velocity norm for Ha=0.0 and case B2*

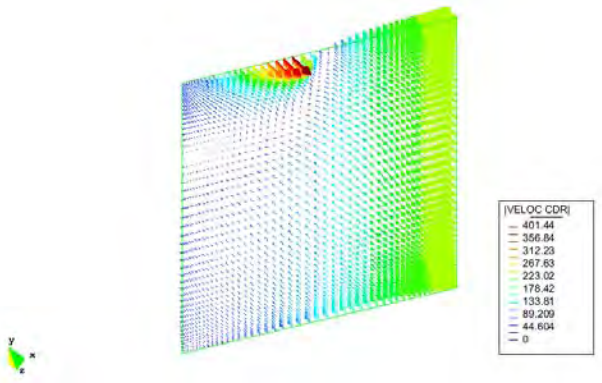

Figure 5.92 *Velocity vectors for Ha=0.0 and case B2*

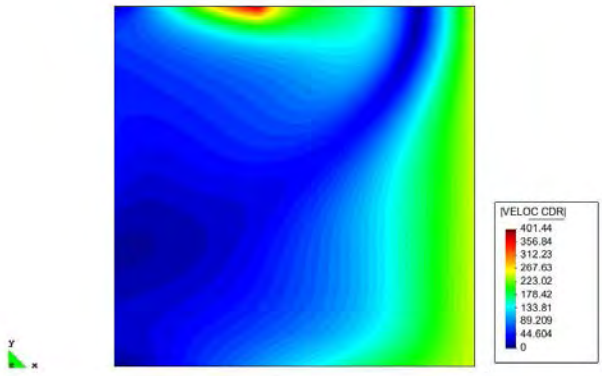

Figure 5.93 *Velocity norm for Ha=5.0 and case B2*

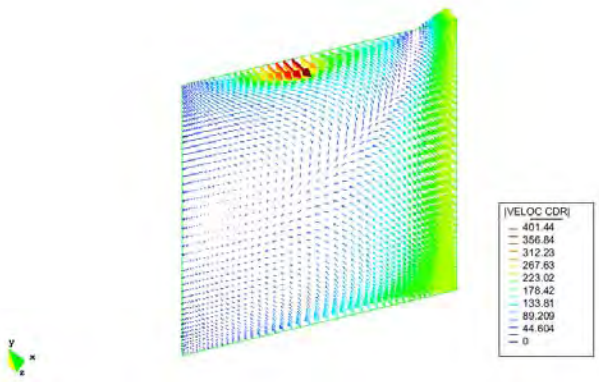

Figure 5.94 *Velocity vectors for Ha=5.0 and case B2*

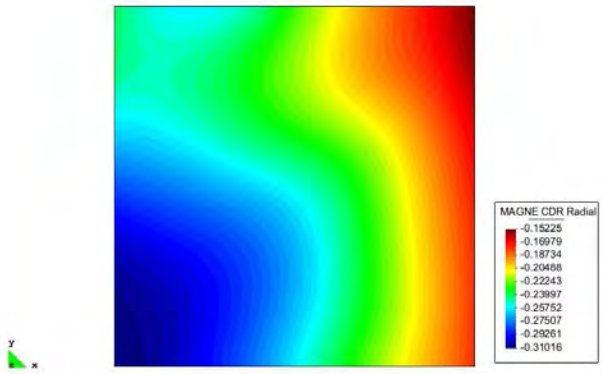

Figure 5.95 *Radial component of the magnetic field for Ha=5.0 and case B2*

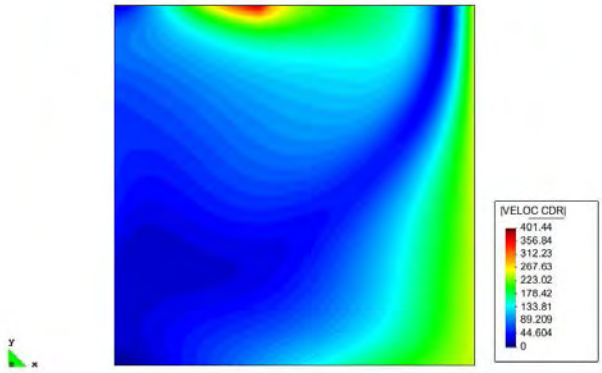

Figure 5.96 *Velocity norm for Ha=10.0 and case B2*

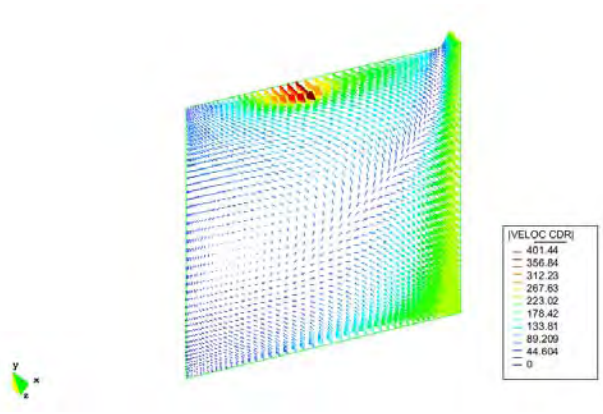

Figure 5.97 *Velocity vectors for Ha=10.0 and case B2*

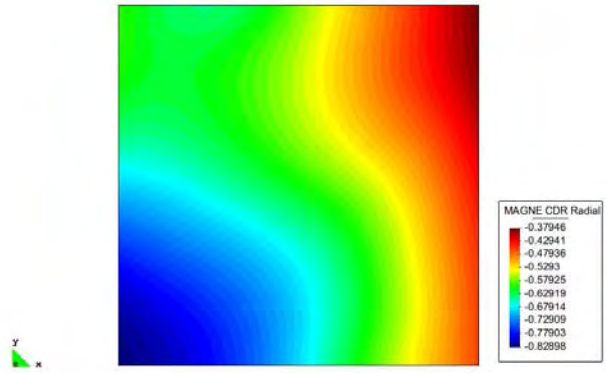

Figure 5.98 *Radial component of the magnetic field for Ha=10.0 and case B2*

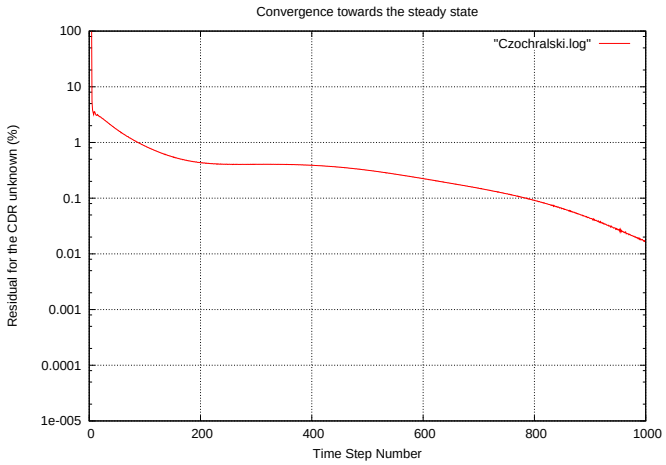

Figure 5.99 *Convergence toward the steady state for Ha=10.0 and case B2*

5.5.3 Case C2

This case is used to analyze the heat transfer phenomena involved in the Czochralski process. Temperature boundary conditions were imposed over the crucible and the crystal. In this case, both the crucible and the crystal will be stationary and therefore no movement in the liquid semiconductor is due to velocity in the crystal nor in the crucible.

The temperature boundary conditions will be the driving force behind the advection movements inside the liquid semiconductor. It has been said before that advection induced movements are harmful for the quality of the semiconductor crystal, therefore in this numerical simulation, while the Hartmann number is increased, the advection induced movements will be diminished.

For Hartmann $Ha = 0.0$, this case presents a new component in the simulation, i.e. advection due to the temperature. The temperature field is presented in figure 5.102. The velocity norm is presented in figure 5.100, it can be observed that the maximum velocity, for this Harmann number $Ha = 0.0$, is slightly above 200.0. For this case as was said before there is no movement induced neither by the crystal nor by the crucible, therefore there is no azimuthal component in the velocity field, this can be observed in figure 5.101. It can also be observed that there is now a temperature field for the simulation as is shown in figure 5.102

For a Harmann number of $Ha = 5.0$, figure 5.103 shows almost no change in the flow pattern, but there is a decrement in the maximum velocity, as can be observed at figure 5.103, where the velocity norm is around 175.0.

For Harmann number $Ha = 10.0$ there is a noticeable change in the flow patter and also in the maximum velocity as can be observed in figure 5.107, where the maximum velocity is around 120.0. This shows that the use of magnetic field in the presence of advection movements can greatly diminish the intensity of those movements.

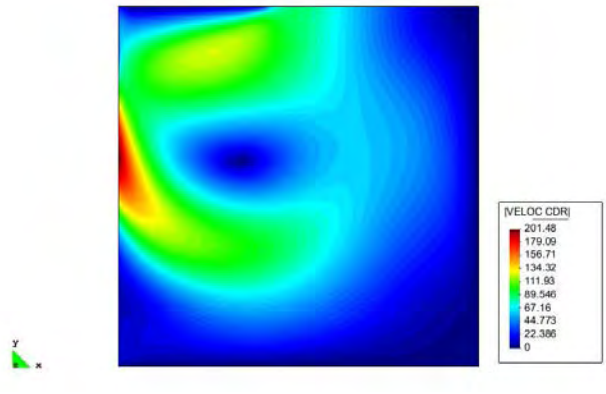

Figure 5.100 *Velocity norm for Ha=0.0 and case C2*

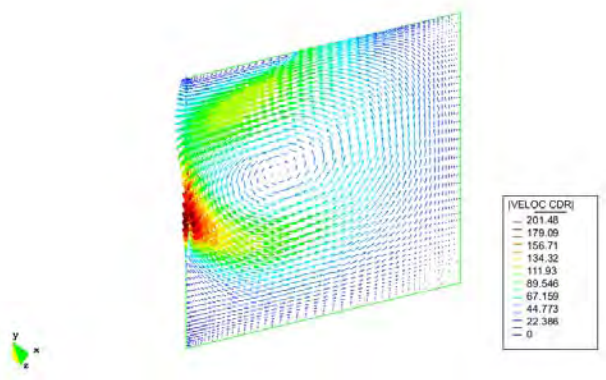

Figure 5.101 *Velocity vectors for Ha=0.0 and case C2*

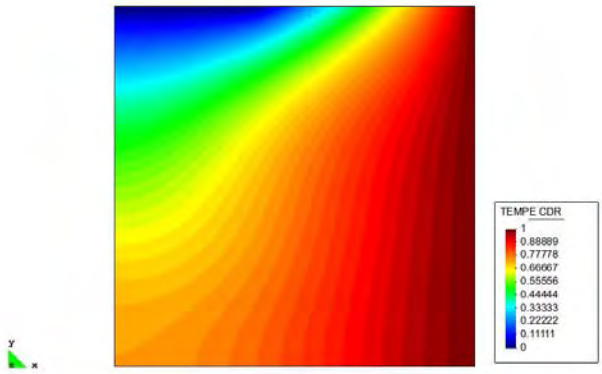

Figure 5.102 *Temperature for Ha=0.0 and case C2*

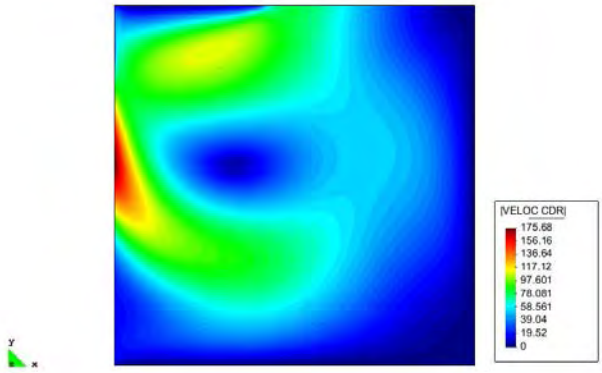

Figure 5.103 *Velocity norm for Ha=5.0 and case C2*

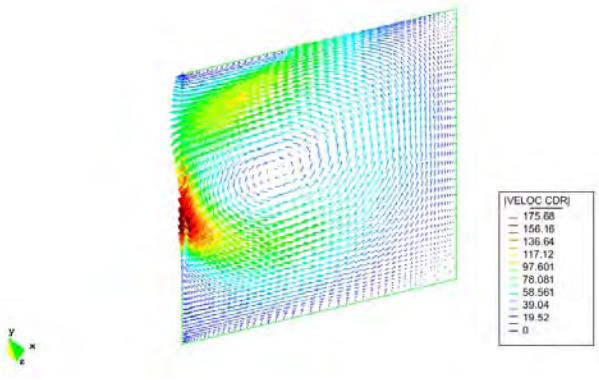

Figure 5.104 *Velocity vectors for Ha=5.0 and case C2*

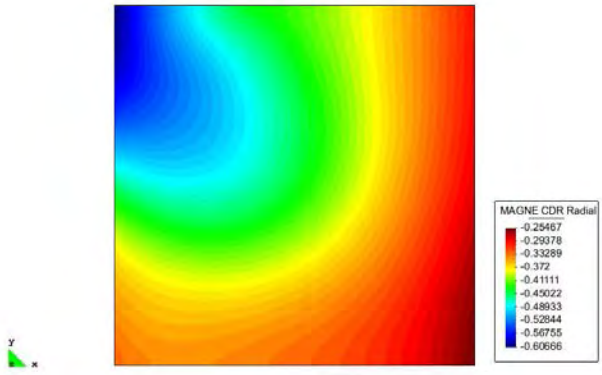

Figure 5.105 *Radial component of the magnetic field for Ha=5.0 and case C2*

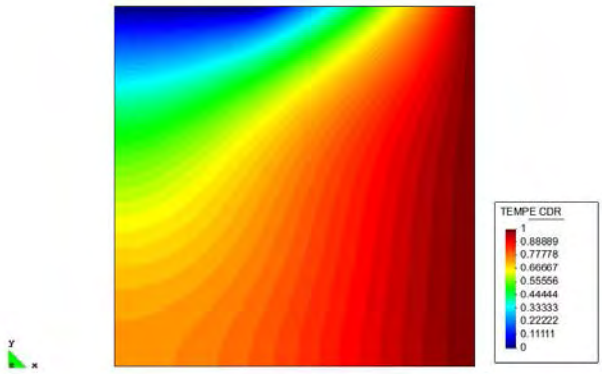

Figure 5.106 *Temperature for Ha=5.0 and case C2*

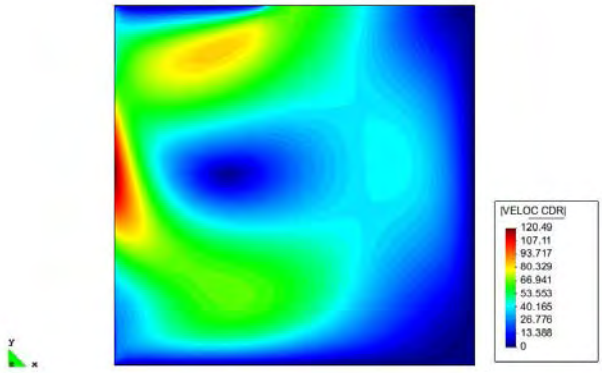

Figure 5.107 *Velocity norm for Ha=10.0 and case C2*

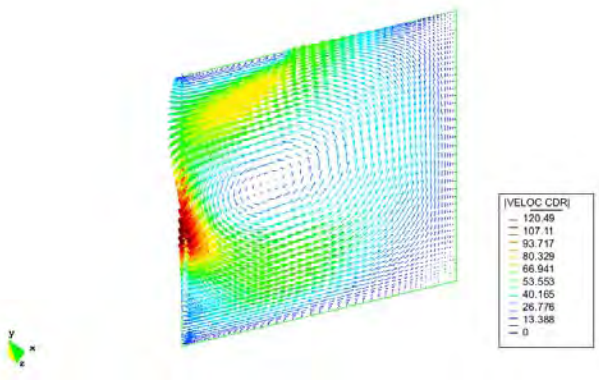

Figure 5.108 *Velocity vectors for Ha=10.0 and case C2*

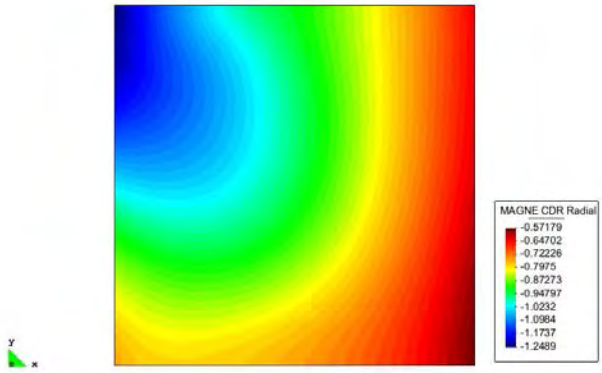

Figure 5.109 *Radial component of the magnetic field for Ha=10.0 and case C2*

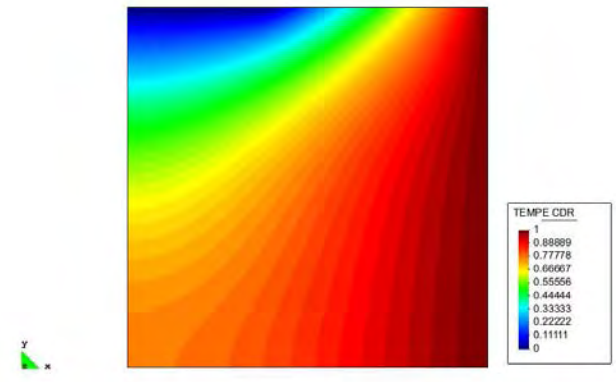

Figure 5.110 *Temperature for Ha=10.0 and case C2*

Finally figure 5.111 shows the convergence history toward steady state for case C2 and $Ha = 10.0$.

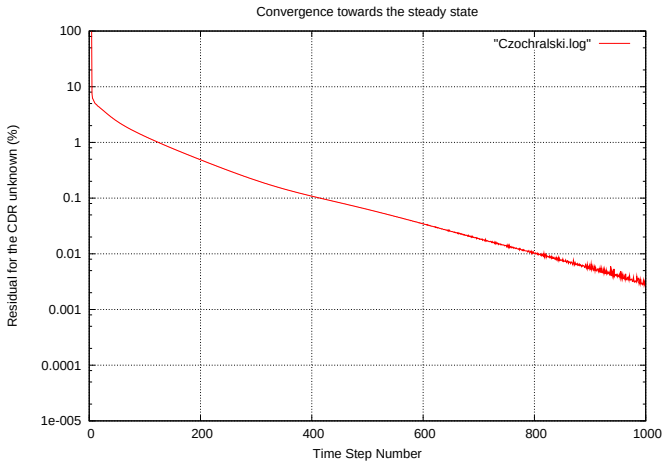

Figure 5.111 *Convergence toward the steady state for Ha=10.0 and case C2*

5.5.4 Case D2

This last case introduces a complete coupled Czochralski process, where the liquid in contact with the crystal has an imposed velocity and the crystal and the crucible have boundary conditions imposed over the temperature. Although the crucible is stationary, this case makes noticeable the quite complex flow patters that arise when advection movements are added to movements due to velocity in the crystal or in the crucible.

For Hartmann number $Ha = 0.0$ the flow pattern is quite similar to the pattern for case C2 at $Ha = 0.0$. This is due to the fact that the imposed velocity in the liquid by the crystal is overshadowed by the velocity induced by advection. In order to observe the velocity induced by the crystal movement only the azimuthal component of the velocity vector is shown in figure 5.114.

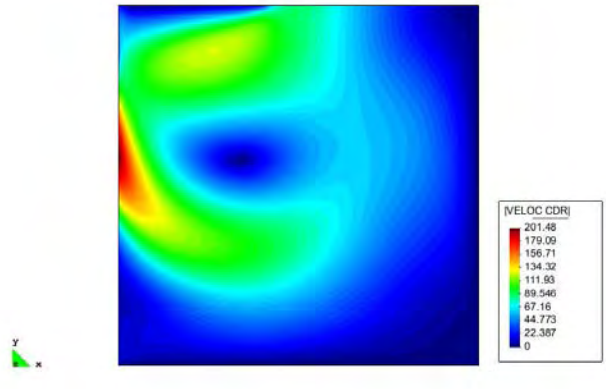

Figure 5.112 *Velocity norm for Ha=0.0 and case D2*

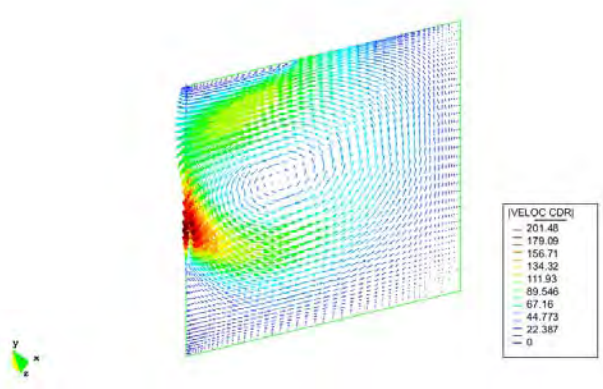

Figure 5.113 *Velocity vectors for Ha=0.0 and case D2*

For the next Hartmann number $Ha = 5.0$ the flow pattern shows similar behavior to the case C2 for the same Hartmann number. The flow patter is the same and the maximum velocity norm has the same value as in the case C2 for the same Hartmann number. But if the azimuthal component of the velocity is analyzed, a clear change in the flow pattern is observed, as is presented in figure 5.118.

For the last value of the Hartmann number $Ha = 10.0$, the overall flow patter

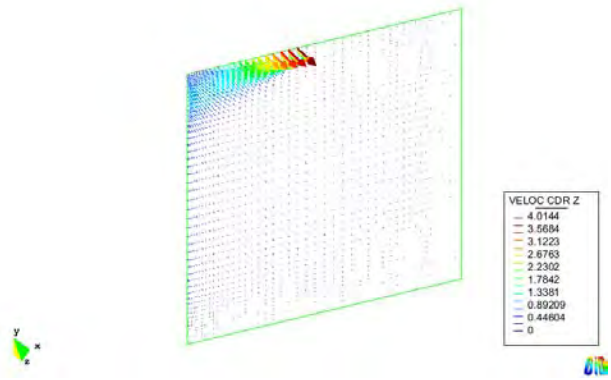

Figure 5.114 *Azimuthal velocity vectors for Ha=0.0 and case D2*

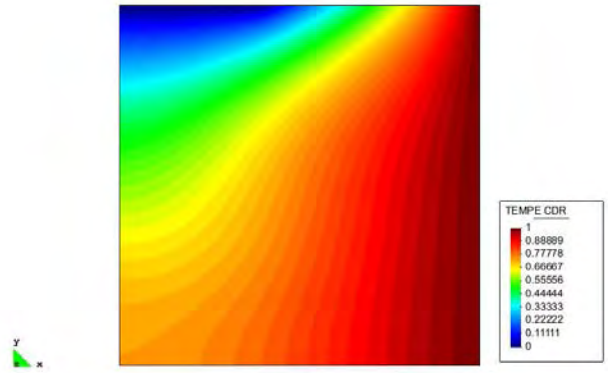

Figure 5.115 *Temperature for Ha=0.0 and case D2*

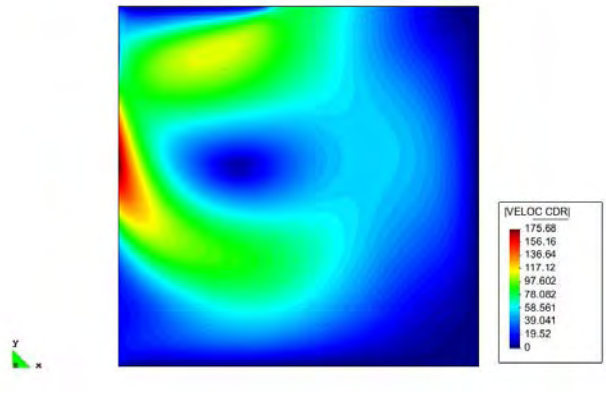

Figure 5.116 *Velocity norm for Ha=5.0 and case D2*

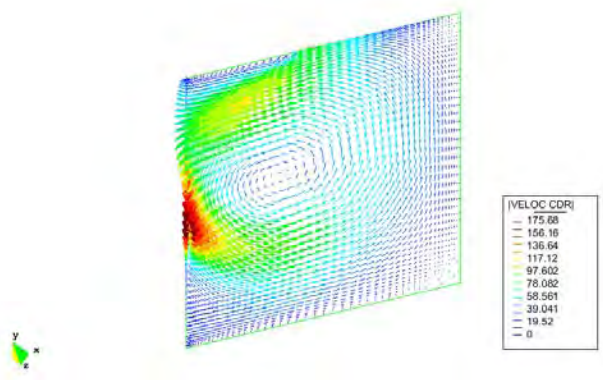

Figure 5.117 *Velocity vectors for Ha=5.0 and case D2*

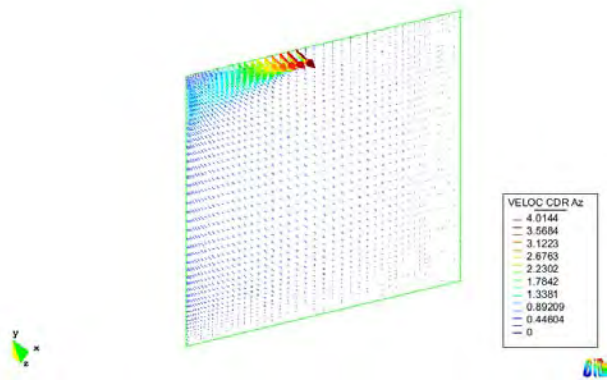

Figure 5.118 *Azimuthal velocity vectors for Ha=5.0 and case D2*

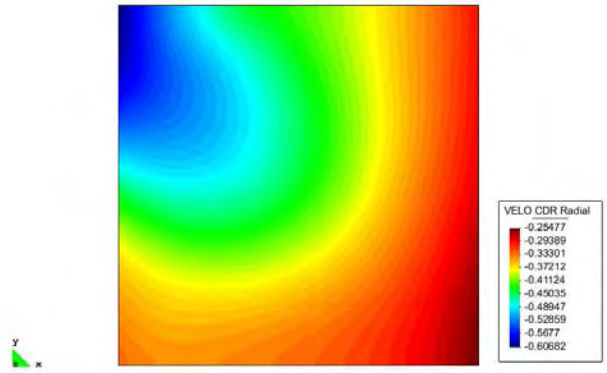

Figure 5.119 *Radial component of the magnetic field for Ha=5.0 and case D2*

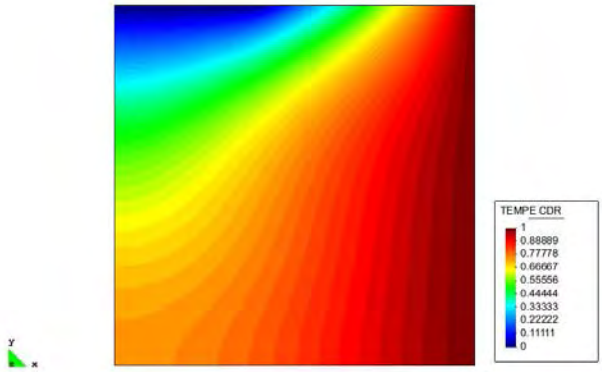

Figure 5.120 *Temperature for Ha=5.0 and case D2*

shows the same behavior as in case C2 for the same Hartmann number. The analysis of the azimuthal component of the velocity vector shows that for this Hartmann number the velocity field shows the characteristic homogenization of velocity, already observed in previous cases. The maximum value for the azimuthal component of velocity does not change but the flow patter is quite different from the pattern observed for $Ha = 0.0$ as can be seen in figure 5.123.

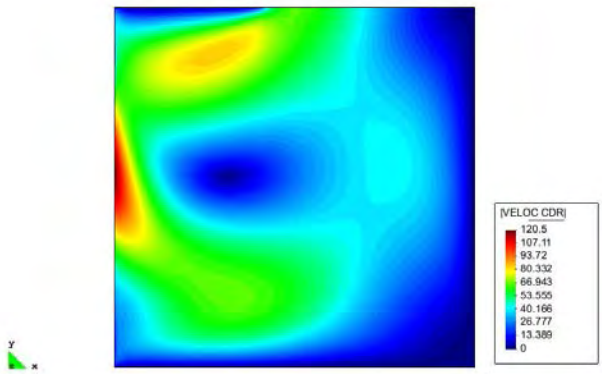

Figure 5.121 *Velocity norm for Ha=10.0 and case D2*

Finally figure 5.99 shows the convergence history toward steady state for case D2 and $Ha = 10.0$.

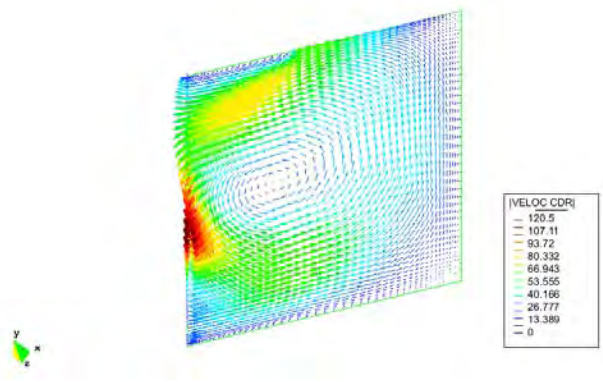

Figure 5.122 *Velocity vectors for Ha=10.0 and case D2*

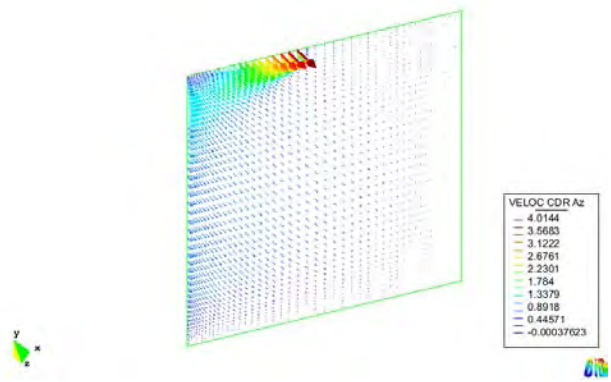

Figure 5.123 *Azimuthal velocity vectors for Ha=10.0 and case D2*

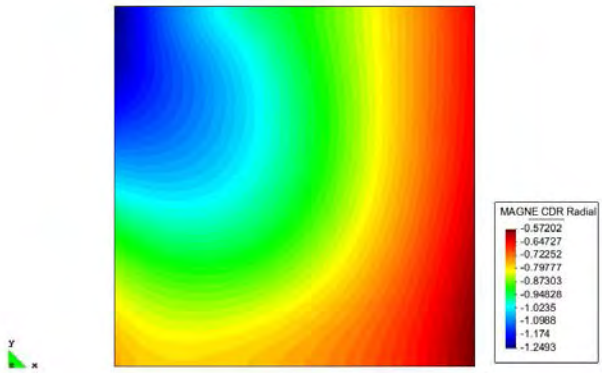

Figure 5.124 *Radial component of the magnetic field for Ha=10.0 and case D2*

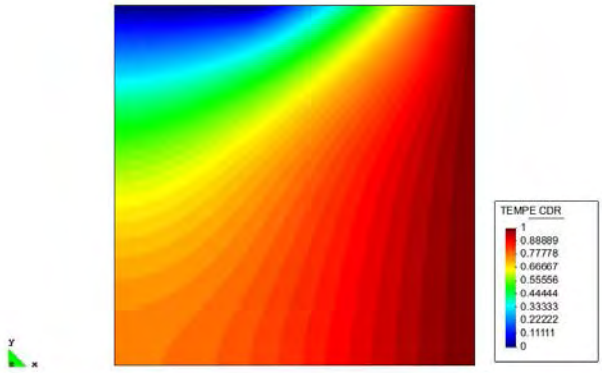

Figure 5.125 *Temperature for Ha=10.0 and case D2*

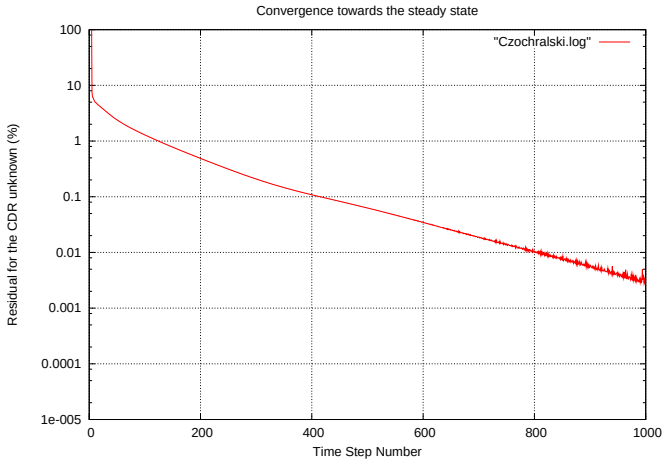

Figure 5.126 *Convergence toward the steady state for Ha=10.0 and case D2*

Chapter 6

Conclusions

The main objective of this thesis, namely the development of an efficient finite element algorithm for the incompressible Magnetohydrodynamics equations, has been accomplished. The development of such algorithm is an important addition to the tools available for the research of phenomena where liquid conductors under magnetic fields are present. Although this effort was limited to incompressible fluids, it can be used as the first step towards more complex phenomena where compressible fluids are involved.

The enforcement of the inf–sup condition and the suppression of the spurious oscillations in the magnetic field posed as the main problems to develop the algorithm. Such problems were tackled using strategies of proved effectiveness such as the Variational Multiscale approach and the use of a Lagrange multiplier.

An algorithm for the incompressible Magnetohydrodynamics equations is also an important tool for the study of some important technological applications. Most of those applications lie on the field of processing liquid semi–conductors like the silicon in order to build semiconductor crystals used in the electronic industry.

The second main application where the algorithm developed in this thesis is useful is the processing of liquid metals. In modern metallurgy, the handling of liquid metals with minimum or no contamination is one of the most important issues. MHD provides a way to do this effectively, but the precise mechanism under the magnetic forces that affects the behavior of the liquid metals must be studied before implementing any kind of solution. The algorithm developed at this work provides an efficient way to tackle this task.

6.1 Achievements

This thesis presents a stabilized finite element approximation for the incompressible Magnetohydrodynamics equations. This stabilized finite element approximation uses the algebraic version of the Variational Multiscale approach and a fictitious variable that plays the role of a Lagrangian multiplier. By using these two numerical resources, the main problems in finite element applied to MHD are addressed.

Namely:

1. Avoiding the need to satisfy the the inf–sup conditions.
2. The suppression of spurious solutions in the magnetic field due to equation (3.3.4) being neglected.
3. The suppression of spurious oscillations (in the magnetic field and the velocity) due to dominant first order terms.

First, the inf–sup conditions over the fluid velocity and the pressure in one hand and the magnetic field and the fictitious variable in the other hand are handled with the Variational Multiscale approach. This approach allows to overcome the compatibility problems between interpolating spaces.

Second, the spurious solutions in the magnetic field are handled with the fictitious variable r playing the role of a Lagrange multiplier. It was shown by Jiang et. al. [34] that those spurious solutions arise due to the zero divergence condition not being properly enforced. In order to address this enforcement the fictitious variable r is introduced and it plays the role of a Lagrange multiplier.

This is the first time these two numerical approaches are combined together to build a numerical scheme for MHD equations. It is also the first time a completely stabilized finite element scheme for MHD has been developed. Previous efforts were limited to stabilize only one variable and for this research all variables were stabilized.

The use of these two numerical resources within the frame of MHD equations opens the door to more complex simulations to gain insight in the particular nature of the phenomena involved and their possible applications to industrial processes.

In the field of industrial applications, the numerical scheme developed in this research has been applied to two industrial situations where MHD phenomena is present. First the clogging in continuous casting of steel and second the Czochralski process for the growth of semiconductor crystals. These industrial processes are quite relevant at industry today and justify, from a technological point of view, the development of numerical schemes for the MHD equations.

6.2 Possible Future Research Lines

There is a bright future for numerical simulations for MHD equations. The increase of possible applications in energy generation and semi–conductors process lights the path of the possible research lines to be followed:

1. Compressible flows interacting with Magnetic Fields.
2. Turbulence incorporated in MHD models.

The first research line arises from the future applications due to the plasma confinement required in order to develop a useful nuclear fusion reactor. The possible benefits from such a massive source of energy as nuclear fusion drives the efforts to develop more efficient numerical schemes in MHD for compressible flows.

This line of future research is not only important due to its technological applications but also because the behavior of compressible fluids in MHD poses a major numerical challenge that must be addressed. Also the strong non linearities that are present in the compressible case of MHD increase the difficulty involved in the numerical simulation of such phenomena.

The need to incorporate turbulence in MHD models arises from the processing of liquid metals and semiconductors and from liquid metal cooling of nuclear reactors. The current efforts in these technological areas provide the drive to keep developing better numerical schemes where turbulence is incorporated.

This line of research also involves major numerical challenges, such as the adequate modeling of the dynamo effect. This area involves a major component of fundamental research because the mechanism behind the dynamo effect is not fully understood and therefore its numerical modeling poses major difficulties.

References

[1] H. Alfvén. Existence of electromagnetic–hydrodynamic waves. *Nature*, 150:405–406, 1942.

[2] H. Alfvén. On the cosmogony of the solar system III. *Stockholms Observatoriums Annaler*, 14:1–29, 1942.

[3] F. Armero and J.C. Simo. Long–term dissipativity of time–stepping algorithms for an abstract evolution equation with applications to the incompressible MHD and Navier–Stokes equations. *Computer Methods in Applied Mechanics and Engineering*, 131:41–90, 1996.

[4] D. Arnold, F. Brezzi, and M. Fortin. A stable finite element for the Stokes equations. *Calcolo*, 21:337–344, 1984.

[5] C. Baiocchi, F. Brezzi, and L.P. Franca. Virtual bubbles and Galerkin–Least–Squares type methods(G.L.S.). *Computer Methods in Applied Mechanics and Engineering*, 105:125–141, 1993.

[6] G.K. Batchelor. *An Introduction to Fluid Dynamics*. Cambridge University Press, Cambridge, England, 1967.

[7] U. Bückle and M. Schäfer. Benchmark results for the numerical simulation of flow in czochralski crystal growth. *Journal of Crystal Growth*, 126:682–694, 1993.

[8] A.N. Brooks and T.J.R. Hughes. Streamline upwind/petrov–galerkin formulations for convection dominated flows with particular emphasis on the incompressible navier–stokes equations. *Computer Methods in Applied Mechanics and Engineering*, 32:199–259, 1982.

[9] M. Cervera, R. Codina, and M. Galindo. On the computational efficiency and implementation of block–iterative algorithms for nonlinear coupled problems. *Engineering Computations*, 13:4–30, 1996.

[10] M. Charina, A.J. Meir, and P.G. Schmidt. Mixed velocity, stress, current, and potential boundary conditions for stationary mhd flow. *Computers and Mathematics with Applications*, 48:1181–1190, 2004.

[11] R. Codina. Comparison of some finite element methods for solving the diffusion–convection–reaction equation. *Computer Methods in Applied Mechanics and Engineering*, 156:185–210, 1998.

[12] R. Codina. On stabilized finite element methods for linear systems of convection–diffusion–reaction equations. *Computer Methods in Applied Mechanics and Engineering*, 188:61–82, 2000.

[13] R. Codina. A stabilized finite element method for generalized stationary incompressible flows. *Computer Methods in Applied Mechanics and Engineering*, 190:2681–2706, 2001.

[14] R. Codina. Stabilized finite element approximation of transient incompressible flows using orthogonal subscales. *Computer Methods in Applied Mechanics and Engineering*, 191:4295–4321, 2002.

[15] R. Codina and J. Blasco. Analysis of a pressure stabilized finite element approximation of the stationary Navier–Stokes equations. *Numerische Matematik*, 87:59–81, 2000.

[16] T. G. Cowling. The magnetic field of sunspots. *Monthly Notices of the Royal Astronomical Society*, 94:39–48, 1933.

[17] P.A. Davidson. Magnetohydrodynamics in materials processing. *Annual Review of Fluid Mechanics*, 31:273–300, 1999.

[18] P. Dold and K.W. Benz. Rotating magnetic fields: Fluid flow and crystal growth applications. *Progress in Crystal Growth and Characterization of Materials*, pages 7–38, 1997.

[19] A. Einstein and L. Szilard. U.S. patent 1,781,541: Refrigeration. November 1930.

[20] M. Faraday. The Bakerian lecture: Experimental researches in electricity. *Philosophical Transactions of the Royal Society of London*, 122:163–194, 1832.

[21] J. F. Gerbeau. A stabilized finite element method for the incompressible magnetohydrodynamic equations. *Numerische Mathematik*, 87:83–111, 2000.

[22] J.L. Guermond and P.D. Minev. Mixed finite element approximation of an MHD problem involving conducting and insulating regions: The 2D case. *Mathematical Modeling and Numerical Analysis*, 36:517–536, 2002.

[23] J.L. Guermond and P.D. Minev. Mixed finite element approximation of an MHD problem involving conducting and insulating regions: The 3D case. *Numerical Methods for Partial Differential Equations*, 19:709–731, 2003.

[24] M. D. Gunzburger, A. J. Meir, and J. S. Peterson. On the existence, uniqueness and finite element approximation of solutions of the equations of stationary, incompressible magnetohydrodynamics. *Mathematics of Computation*, 56:523–563, 1991.

[25] M.D. Gunzburger. *Finite Element Method for Viscous Incompressible Flows.* Academic Press, 1989.

[26] J. Hartmann. Theory of the laminar flow of an electrically conductive liquid in a homogeneous magnetic field. *Matematisk-fysiske Meddelelser*, 15, 1937.

[27] J. Hartmann and F. Lazarus. Experimental investigations on the flow of mercury in a homogeneous magnetic field. *Matematisk-fysiske Meddelelser*, 15, 1937.

[28] O. Heaviside. On the forces, stresses and fluxes of energy in the electromagnetic field. *Philosophical Transactions of the Royal Society*, 183A:423, 1892.

[29] T.J.R. Hughes. Multiscale phenomena: Green's functions, the Dirichlet–to–Neumann formulation, subgrid scale models, bubbles and the origins of stabilized formulations. *Computer Methods in Applied Mechanics and Engineering*, 127:387–401, 1995.

[30] T.J.R. Hughes, G.R. Feijóo, L. Mazzei, and J.B. Quincy. The variational multiscale method–a paradigm for computational mechanics. *Computer Methods in Applied Mechanics and Engineering*, 166:3–24, 1998.

[31] T.J.R. Hughes, L.P. Franca, and M. Balestra. A new finite element formulation for computational fluid dynamics: V circumventing the Babuška–Brezzi condition: A stable Petrov–Galerkin formulation of the Stokes problem acommodating equal–order interpolations. *Computer Methods in Applied Mechanics and Engineering*, 59:85–99, 1986.

[32] T.J.R. Hughes, L.P. Franca, and G.M. Hulbert. A new finite element formulation for computational fluid dynamics: VIII the Galerkin/Least–Squares methods for advective diffusive equations. *Computer Methods in Applied Mechanics and Engineering*, 73:173–189, 1989.

[33] T.P. Hughes. Einstein: The inventor. *American Heritage Magazine*, 6, 1991.

[34] B. Jiang, J. Wu, and L.A. Povinelli. The origin of spurious solutions in computational electromagnetics. *Journal of Computational Physics*, 125:104–123, 1996.

[35] L.I. Kadar, P.P.Biringex, and J.D. Lavers. Modification of the nozzle flow using electromagnetic induction. *IEEE Transactions on Magnetics*, 30:4686–4688, 1994.

[36] B. Karlovitz and D. Halasz. U.S. patent 2,210,918: Process for the conversion of energy and apparatus for carrying out the process. August 1940.

[37] Th. Von Kármán. *Aerodynamics.* Cornell University Press, Ithaca, New York, 1954.

[38] H. Kürth. *Stahl und Eisen*, 39:512, 1917.

[39] L.D. Landau and E.M. Lifshitz. *Electrodynamics of Continuous Media*. Pergamon Press, Oxford England, 1987.

[40] L.D. Landau and E.M. Lifshitz. *Fluid Mechanics*. Pergamon Press, Oxford England, 1987.

[41] J. Larmor. How could a rotating body as the sun become a magnet? *Report of the British Association for the Advancement of Science*, pages 159–160, 1919.

[42] J.D. Lavers and L.I. Kadar. Application of electromagnetic forces to reduce tundish nozzle clogging. *Applied Mathematical Modelling*, 28:29–45, 2004.

[43] J.C. Maxwell. A dynamical theory of the electromagnetic field. *Royal Society Transactions*, 155:459–512, 1865.

[44] A. J. Meir. Thermally coupled magnetohydrodynamics flow. *Applied Mathematics and Computation*, 65:79–94, 1994.

[45] A. J. Meir and P. G. Schmidt. A velocity–current formulation for stationary MHD flow. *Applied Mathematics and Computation*, 65:95–109, 1994.

[46] A. J. Meir and P. G. Schmidt. Variational methods for stationary MHD flow under natural interface conditions. *Nonlinear Analysis, Theory, Methods and Applications*, 26:659–689, 1996.

[47] H.K. Moffatt and M.R.E. Proctor, editors. *Metallurgical Applications of Magnetohydrodynamics: Proceedings of a Symposium of the IUTAM held at Trinity College, Cambridge, UK*. The Metals Society, London, 1984.

[48] J.B. Mullin and K.F. Hulme. The use of electromagnetic stirring in zone refining. *Journal of Electronics and Control*, 4:170–174, 1958.

[49] G. Mutschke, G. Gerbeth, T. Albrecht, and R. Grundmann. Separation control at hydrofoils using Lorentz forces. *European Journal of Mechanics B/Fluids*, 25:137–152, 2006.

[50] E.J. Peralta. U.S. patent 7,303,581: Artificial heart using magnetohydrodynamic propulsion. December 2007.

[51] J. S. Peterson. On the finite element approximation of incompressible flows of an electrically conducting fluid. *Numerical Methods for Partial Differential Equations*, 4:57–68, 1988.

[52] O.M. Phillips. The prospects for magnetohydrdynamic ship propulsion. *Journal of Ship Research*, pages 43–51, 1962.

[53] K. G. Rackers and B. G. Thomas. Clogging in continuous casting nozzles. In *78th Steelmaking Conference Proceedings*, pages 723–734, Nashville TN., 1995. Iron and Steel Society.

[54] W. Ritchie. Experimental researches in voltaic electricity and electro–magnetism. *Philosophical Transactions of the Royal Society of London*, 122:279–298, 1832.

[55] N. B. Salah, A. Soulaimani, and W. G. Habashi. A finite element method for the magnetohydrodynamics equations. *Computer Methods in Applied Mechanics and Engineering*, 190:5867–5892, 2001.

[56] N. B. Salah, A. Soulaimani, W. G. Habashi, and M. Fortin. A conservative stabilized finite element method for the magneto–hydrodynamic equations. *International Journal for Numerical Methods in Fluids*, 29:535–554, 1999.

[57] Y. Sasakawa, S. Takezawa, Y. Sugawara, and Y. Kyotani. The superconducting MHD-propelled ship YAMATO-1. In *Proceedings of the 4th International Conference and Exhibition: World Congress on Superconductivity (SEE N96-10230 01-76)*, volume 1, pages 167–176. NASA. Johnson Space Center, 1995.

[58] D. Schötzau. Mixed finite element methods for stationary incompressible magneto–hydrodynamics. *Numerische Matematik*, 96:771–800, 2004.

[59] D.A. Shtanko. Solidification of steel in a magnetic field. *Zh. Tekh. Fiz*, 3:1085, 1933.

[60] B. Singh and J. Lal. Finite element method in magnetohydrodynamic channel flow problems. *International Journal for Numerical Methods in Engineering*, 18:1104–1111, 1982.

[61] M. Tezer-Sezgin and S. Köksal. Finite element method for solving MHD flow in a rectangular duct. *International Journal for Numerical Methods in Engineering*, 28:445–459, 1989.

[62] S.T. Wu. Unsteady MHD duct flow by the finite element method. *International Journal for Numerical Methods in Engineering*, 6:3–10, 1973.

[63] N. Zou and A. Nehorai. Detection of ship wakes using an airborne magnetic transducer. *IEEE Transactions on Geoscience and Remote Sensing*, 38:532–539, 2000.